Stony Brook University

MECHANISMS AND SPATIOTEMPORAL EVOLUTION OF INTRACELLULAR Ca^{2+} ALTERNANS IN CARDIAC TISSUE

A Dissertation Presented

By

Zhiheng Jia

to

The Graduate School

in Partial Fulfillment of the

Requirements

for the Degree of

Doctorate of Philosophy

in

Biomedical Engineering

Stony Brook University

May 2012

Stony Brook University

The Graduate School

Zhiheng Jia

We, the dissertation committee for the above candidate for the

Doctorate of Philosophy degree, hereby recommend

acceptance of this dissertation.

Dr. Emilia Entcheva, Advisor
Associate Professor, Biomedical Engineering

Dr. Ira S. Cohen, Member
Professor, Physiology & Biophysics

Dr. Yingtian Pan, Member
Professor, Biomedical Engineering

Dr. David J. Christini, Member
Professor, Weill Cornell Medical College

This dissertation is accepted by the Graduate School

Charles Taber
Interim Dean of the Graduate School

Abstract of the Dissertation

Mechanisms and spatiotemporal evolution of intracellular Ca^{2+} alternans in cardiac tissue

By

Zhiheng Jia

Doctorate of Philosophy

in

Biomedical Engineering

Stony Brook University

2012

Instabilities in cardiac repolarization, presented as T-wave alternans (TWA) in the ECG, are a known precursor of re-entrant cardiac arrhythmias, e.g. ventricular tachycardia (VT) and ventricular fibrillation (VF). Alternations in intracellular Ca^{2+} cycling have been suggested recently as direct contributors to instabilities in action potential duration (APD) and TWA. Furthermore, both computer simulations and experiments have shown that subtle fine-scale intracellular Ca^{2+} alternans emerge much earlier than detectable VT and VF episodes, and can promote the initiation of VT/VF. Recent experimental results from our lab and others revealed that the alternans regions may be persistent during VT. Overall, these findings corroborate the notion that the genesis and evolution of Ca^{2+} alternans are tightly linked to VT/VF development.

We hypothesize that alternans in intracellular Ca^{2+} are not all-or-nothing response, but evolve gradually over time and space, and are influenced by several important factors, e.g.

cellular coupling and Ca^{2+}-Vm kinetics. The goal of this research is to quantify the influences of these factors with the long-term objective to predict arrhythmia development based on spatiotemporal profiles of early-stage alternans.

Experimental testing of this hypothesis, particularly the capture and characterization of the early-stage fine-scale alternans, which are dynamically changing, requires specialized technical tools that were specifically developed for this project – e.g. automated computer detection/characterization algorithms for fine alternans in conjunction with ultra-high spatiotemporal resolution macroscopic imaging system. Furthermore, mathematical models were employed as complementary tools to validate and expand the experimental findings. Finally, a new technological development by our lab – an optogenetic approach (use of exogenous light-sensitive ion channels) was used to provide optical instead of electrical stimulation of cardiac tissue and to probe for the role of virtual electrodes in the emergence of fine-scale alternans.

This research is the first to tackle the challenge of automatically identifying and tracking the spatiotemporal characteristics of cell-level calcium alternans over a large field of view, at the early stage of onset. By developing a theoretical and experimental framework for the effects of cellular coupling and Ca^{2+}-V_m coupling on the spatiotemporal evolution of alternans, this work aims to provide new predictive tools to systematically correlate early stage alternans to later arrhythmia development.

I dedicate this dissertation to my family:
My wife, ling li, who has been with me for 11 years as an amazing partner.
My mother and father, whose support, encouragement, and constant love have sustained me throughout my life.

Table of Contents

List of Tables and Figures

Chapter 1: Introduction and specific Aims

Chapter 2: Detecting space-time alternating biological signals close to the bifurcation point

Chapter 3: The effects of cellular coupling on the spatiotemporal evolution of intracellular Ca^{2+} alternans

Chapter 4: Computer simulations of Ca^{2+} alternans and variable diffusion in a cardiac model

Chapter 5: The development of cardiac optogenetics by cell delivery and its application to fine alternans verification

Chapter 6: Future work

List of Abbreviations

4PB	4-phenylbutyrate
$[Ca]_i$	Intracellular calcium
$[dF/dt]_{max}$	Maximum upstroke rate
$[dV/dt]_{max}$	Maximum depolarization rate
$\frac{\partial^2 v}{\partial x^2}$	Spatial gradient of membrane potential
$\frac{\partial v}{\partial t}$	Temporal gradient of membrane potential
λ	Space constant
τ	Time constant
APD	Action potential duration
BDM	Butanedione monoxime
BNP	Brain natriuretic peptide
Cav1.2	Voltage-gated calcium channel 1.2
CF	Carboxyfluorescein
CICR	Calcium-induced calcium release
CPVT	Catecholaminergic polymorphic ventricular tachycardia
CTD	Calcium transient duration
CV	Conduction velocity
Cx43	Connexin 43

DAD	Delayed afterdepolarization
DI	Diastolic interval
ECG	Electrocardiogram
FRAP	Fluorescence recovery after photobleaching
FOV	Field of view
g_j	Gap junction conductance
I_{CaL}	L-type calcium current
I_{TO}	Transient outward potassium current
Kir2.1	Inward rectifying potassium channel 2.1
Kv4.3	Voltage-gated potassium channel 4.3
L	Longitudinal/parallel to the direction of tissue alignment
MTWA	microvolt T-wave alternans
Myh6	α-myosin heavy chain gene
Myh7	β-myosin heavy chain gene
Nif	Nifedipine
PDMS	Polydimethylsiloxane
PMT	Photomultiplier tube
r_e	Extracellular resistance
r_i	Intracellular resistance
r_m	Membrane resistance

RT-PCR	Real time-polymerase chain reaction
SCA	Spatially concordant alternans
SDA	Spatially discordant alternans
SR	Sarcoplasmic reticulum
t	Time
TCU	Tandem cell unit
TP	Temporal persistence
TWA	T wave alternans
V_m	Transmembrane voltage
VF	Ventricular fibrillation
VT	Ventricular tachycardia

Acknowledgments

Firstly, I would like to sincerely and gratefully thank Dr. Emilia Entcheva for her patience, support, guidance, and most importantly, her friendship during my graduate studies at Stony Brook. I still remember six years ago when I just joined the Dr. Entcheva's lab, as a student with mechanical engineering background, I had no idea about Biology and Biophysics, and Dr. Entcheva started patiently to explain to me the process of Calcium-induced calcium release in cardiac cells, which opens the door of cardiac alternans research for me. Moreover, she encouraged me to not only grow as an engineer but also as a scientist with independent thinking.

I would also like to thank all of the members of cardiac cell engineering lab, especially Harold Bien, who taught me all kinds of knowledge: from molecular biology to image processing, from critical thinking to micro-processor programming. Chiung-yin Chung showed me how to do primary cell culture. Harold and CY, these two friends and co-workers, also provided some much needed humor and entertainment in what could have otherwise been a somewhat stressful laboratory environment. I would also like to thank Jianjin Xu for helping me with experiment preparation, Cookie Yu for cell culture, and Steven Leigh for spiral experiment. Thanks to all other lab members past or present during these six years in CCEL: John Williams, Jaslin Kalra, Marek Lhotak, Jacqueline Gunther, Aashay Tattu, Ujas Shah, Christina Ambrosi, Nan Shen, Aleks Klimas, Marcel Hörning, Puja Parikh, Wei Wang, Jia Lu, Mohit, Rohit, Hala, Syed, Budassi, Sandy, etc.

I would like to thank my committee members: Dr. Ira S. Cohen, Dr. David J. Christini and Dr. Yingtian Pan, who supported me through this exciting and challenging journey. Appreciate the time, support and guidance from the dissertation committee throughout my thesis proposal to defense!

More specifically, I would like to thank Zhongju Lu, Huilin Liu and Joan Zuckerman in Dr. Ira Cohen's lab for developing and characterizing HEK-ChR2 cell line, Dr. Yohannes Shiferaw for providing Shif-fox model, Chris Gordon in Dr. Peter Brink's lab for western blot, Virginijus Valiunas and Hong-Zhang Wang for dual patch clamp, Barbara Rosati and Qinghong Yan in David McKinnon's lab for preparing ChR2 plasmid, Urszula Golebiewska and Yuanjian Guo in Dr. Susan Scarlata's lab for FRAP experiment.

I would like to thank the Department of Biomedical Engineering at Stony Brook University, especially Ms. Anne-Marie Dusatko, who guided my through all the paperworks through these six years.

Finally, and most importantly, I would like to thank my wife Ling Li. Her support, encouragement, quiet patience and unwavering love were undeniably the bedrock upon which the past ten years of my life have been built. Her tolerance of my occasional vulgar moods is a testament in itself of her unyielding devotion and love. I thank my parents, for their faith in me and allowing me to be as ambitious as I wanted. It was under their watchful eye that I gained so much drive and an ability to tackle challenges head on.

Chapter 1

INTRODUCTION
AND SPECIFIC AIMS

1.1 Background and Significance

1.1.1 T wave alternans (TWA) and intracellular Ca^{2+} alternans

As reported by American Heart Association in 2009, the overwhelming majority of sudden cardiac deaths (estimated at about 325 000 per year in US) are still caused by arrhythmias like VT/VF [1], which remain highly unpredictable. TWA, the beat-to-beat changes in the morphology or amplitude of the T wave of in an electrocardiogram (ECG), was firstly described in 1908. But only large variations ("macroscopic" TWA) could be detected at that time and the large TWAs were associated with lethal ventricular tachyarrhythmias. With the recent development of detecting technology, microvolt T-wave alternans (MTWA) was discovered and became one of the most promising non-invasive indexes for predicting vulnerability to ventricular arrhythmias in various experimental and clinical conditions. Multiple algorithms, especially spectrum methods, have been developed for detecting MTWA, but its mechanistic underpinnings are not fully understood.

At the tissue level, as Fig.1 shows, computer simulations[2, 3] have demonstrated that T-wave alternans could be caused by spatially concordant alternans (SCA) and spatially discordant alternans (SDA), which can be caused or exaggerated by inherent complex tissue heterogeneities or occurring in fibrosis, infarction [4, 5].

At the cellular lever, the mechanism of cardiac alternans was firstly postulated by Nolasco and Dahlen[6] in 1968. They proposed that the slope of the action potential duration (APD) restitution curve can explain the alternation phenomenon as a generic instability. APD restitution is the relationship between APD and the previous diastolic interval (DI) and can be measured experimentally by plotting APD versus DI when pacing frequency changes. However, recent experiments [7-9] demonstrated that Ca^{2+} instabilities may act as independent pro-arrhythmic factors, as isolated myocytes can exhibit Ca^{2+} alternans without voltage alternants. Without any structural heterogeneity, cellular alternans could be induced by bidirectional coupling between trans-membrane potential and intracellular Ca^{2+}. Also the diffusion properties of intracellular calcium (compared to transmembrane voltage) make it possible to have extremely small scale of occurrence of these instabilities. Both computer simulations [10, 11] and recent experiments [12] have shown that SDAs in intracellular Ca^{2+} can emerge from a single cell, much earlier than detectable macroscopic disturbances in propagation and initiation of VT.

Furthermore, such alternans regions may persist in VT and affect its progression [13, 14]. Therefore, to better understand the initiation and development of VT/VF, it will be imperative to capture and characterize the early onset of intracellular Ca^{2+} alternans and to investigate the mechanisms of their spatiotemporal evolution.

1.1.2 Catecholaminergic polymorphic ventricular tachycardia (CPVT) and intracellular Ca^{2+} alternans

CPVT is an arrhythmia, in which calcium alternans may play essential role, as intracellular Ca^{2+} concentration will be leaking from sarcoplasmic reticulum (SR). CPVT is characterized by episodic syncope occurring during exercise or acute emotion in individuals without structural cardiac abnormalities, which affects about one in ten thousand people, and cause 15% of all unexplained sudden cardiac deaths in young people[15]. Two genes are currently known to be associated with CPVT: RYR2 (autosomal dominant) encodes the cardiac ryanodine receptor channel [16], which is responsible for 50%-55% of cases of CPVT [17] and its mutations are shown in Panel A of Fig.2; CASQ2 (autosomal recessive) encodes calsequestrin, a calcium buffering protein of the sarcoplasmic reticulum (SR) [16], which is responsible for 1%-2% of cases of CPVT [18].

RyR2 plays a key role in cardiac myocyte excitation–contraction coupling, as shown in Panel B of Fig. 2. Upon opening of the cell membrane L-type calcium channels by the depolarizing action potential, small amounts of calcium ions permeate the cardiomyocyte and trigger a ten-fold larger release of calcium ions through the RyR2 channels situated at the SR; this sequence of events is called as calcium-induced calcium release (CICR). The precise mechanisms by which RyR2 mutations cause arrhythmias are as of yet unclear, but it is believed that mutations could induce hyperactive “leaky” release, and in turn promote the spontaneous Ca^{2+} release events that lead to arrhythmogenic delayed afterdepolarizations (DADs). CASQ2 mutations could impaire luminal Ca^{2+} sensing and promote the spontaneous SR release events and DADs underlying the ventricular tachyarrhythmias characteristic of the disease [15].

As a genetically heterogeneous disease, CPVT is heritable and very difficult to prevent. And both of its mutations could lead to spontaneous Ca^{2+} release, serving as origin of cardiac alternans. The proposed research is focusing on the alternas evolution from the early stages at fine scales, even a single cell, to later tissue level arrhythmias, like VT and VF, which may assist

in the development of targeted therapies to prevent early stage cellular alternans to VT or VF, and thus be relevant to therapies for pathologies like CPVT.

1.1.3 Intracellular Ca^{2+} alternans detection and characterization

A variety of techniques, usually based on 1D temporal or spectral analysis, have been proposed in the past three decades for automatic detection of alternans in the ECG, and have facilitated the capture of otherwise invisible TWAs in many clinical and experimental conditions [19-24]. While the detection of microvolt alternans has been a major accomplishment and cannot be undermined, there are several facilitating factors, including typically long records and no need for preservation of spatial/phase information, as often the analyzed data are single-point (not spatial) records. There are parallels in the challenges of detecting microvolt TWAs and subtle intracellular Ca^{2+} alternans. However additional difficulties arise in the latter associated with the use of ultra-high spatiotemporal resolution mapping technology and inherently noisy optical mapping data; data acquired with optical mapping techniques can be of extremely large size (up to a Gigabyte per second of recording) [25]. Automatic detection of intracellular Ca^{2+} alternans over time and space has to not only efficiently process such large data sets but also resolve phase of alternation needed for spatial analysis (distinct from existing TWA detection algorithms).

In spatially-resolved measurements, the detection of alternans has to meet additional challenges: it is informative to track not only their existence (as in T-wave analysis), but also their magnitude and phase for each beat at each spatial location. Preserving phase information is necessary for identification of spatially discordant alternans (SDA), Figure 1B. SDAs can precipitate or coexist with reentrant waves [26] and are more closely associated with the development of reentrant ventricular arrhythmias, irregularities in the ECG and sudden cardiac death [27-29].

More generally, there are many uncertainties in the spatiotemporal alternans detection as Fig.3 shows. (A) Uncertainty in the bifurcation point: As a bifurcation parameter increases, a critical transition takes place, e.g. transition from a 1:1 response to 2:2 response to external perturbation. For a given system's dynamics and in the presence of noise (including natural variability), there exists an uncertainty zone, for which is challenging to determine the exact state of the system. (B) Uncertainty in transition zones between opposite phases of oscillation: Over space, it is possible for neighbouring regions to exhibit opposite phase of alternation. Between them a

"nodal line" or no-alternation zone must exist. In real experiments, the width of this zone will depend on the system's dynamics and the noise in the system. (C) Temporal persistence (TP) of alternation in white noise: left – maximum-length alternating sequence, m, in a random binary signal of length n; right – TP of alternation in a random binary signal of length n. Presented empirical data (10,000 trials per point) show 95% confidence interval for m and TP. Based on these data, a threshold TP for alternans detection can safely be chosen above the curve (right).

1.1.4 Factors that could affect intracellular Ca2+ alternans cellular coupling

Gap junctions provide low-resistance pathways between cardiac myocytes and allow the flow of mostly small intracellular signaling molecules (including Ca^{2+}). Gap junctions are particularly important for the synchronized excitation and contraction in cardiac muscle, which may be disturbed by pathological cell uncoupling.

We hypothesize that cellular coupling can alter the spatiotemporal evolution profiles of intercellular Ca2+ and can be quantitatively linked to later development of arrhythmias. To test this hypothesis, we will design experiments to perturb coupling as follows:

(1) Use a clinically approved anti-cancer agent, 4PB, to increase cellular coupling by promoting the expression of connexin 43 (Cx43) and without other visible changes in function [30].

(2) Decrease cellular connectivity by low doses of a gap junction uncoupler - heptanol [31]. Coupling under these conditions will be quantified by fluorescence recovery after photobleaching (FRAP).

We will employ ultra-high spatiotemporal macroscopic mapping in conjunction with the alternans detection/characterization algorithm in Aim1 to examine the evolution profiles of intracellular Ca2+ and to correlate with the FRAP coupling data.

Ca^{2+}-V_m Dynamics

Cardiac tissue is inherently heterogeneous [29], and conventionally this heterogeneity was considered as the main source of alternans, especially for SDAs [4]. However, computer simulations [3, 32] indicate that SDAs can also be induced in homogeneous tissue by dynamic factors. Furthermore, VT induced by rapid pacing can spontaneously break up into VF in homogeneous initial conditions [33-35]. All these indicate that the evolution of cardiac alternans

could be affected by dynamic factors like local Ca^{2+}-V_m relationship, which can be bidirectional, i.e. voltage or intracellular Ca^{2+} can act as a driving force. When the system is voltage-driven, Ca^{2+} alternans occur as a secondary phenomenon since the transmembrane potential (V_m) can easily affect the voltage-dependent L-type Ca^{2+} channels to induce further Ca^{2+} induced Ca^{2+} release and the electrical signal propagates much faster than the chemical signals (Ca^{2+}). V_m-driven alternans usually occur in positive V_m-Ca^{2+} coupling, while Ca^{2+}-driven alternans can be the result of either positive or negative Ca^{2+}-V_m coupling. We hypothesize that the local V_m-Ca^{2+} kinetics can change the spatiotemporal evolution profile of intracellular Ca^{2+} alternans in a quantifiable way. With the help of computer simulations, we will attempt to reveal the nature of the V_m-Ca^{2+} coupling [10, 36] and how it relates to the spatiotemporal evolution of intracellular Ca^{2+} alternans.

Virtual electrode effects

A potential confounding factor to the fine-scale instabilities studied here can be the so called "virtual electrode effects", where the externally applied electrical field produces areas of positive and negative polarization of various amplitudes next to each other[37, 38]. A point or line source electrode (used for pacing or cardioversion) will inevitably produce spatially non-uniform electrical field. Furthermore, due to the intrinsic heterogeneity of cardiac tissue, there will be small "islands" with various degrees of membrane refractoriness superimposed with large-scale changes in transmembrane potential in cardiac tissue. As a result, the emerging fine-scale instabilities can be influenced by such superimposed polarization effects.

1.1.5 Significance of proposed research

The successful completion of the proposed research will make an important contribution towards the ultimate goal of understanding the mechanisms of initiation of reentrant arrhythmias, including VT/VF, and particularly the role of intracellular Ca^{2+} alternans in the early stages of such instabilities, where prevention may be an option.

The proposed project will also provide new research tools for imaging and automatic detection of the early onset of calcium alternans over space and time; as well as systematic correlation of the spatiotemporal alternans evolution with the underlying cellular coupling and local voltage-

calcium coupling. Such results can help understand and link the sequence of events leading to dangerous reentrant arrhythmias and possibly help design suitable preventive measures.

1.2 Specific Aims

Aim1: Develop tools for identification and characterization of spatiotemporal cardiac alternans with ultrahigh resolution in conditions of noise.

To understand the formation and evolution of alternating regions, especially at the early stage, it is critical to be able to identify and characterize alternans under macroscopic mapping with ultra-high spatiotemporal resolution over large field of view (FOV). We define the following two sub aims:

Aim 1.1: Develop tools for alternans detection over space and time with preservation of phase information in temporal signals contaminated with noise.

We have recently developed a novel algorithm, which in conjunction with ultra-high resolution optical imaging, can detect subtle alternans overcoming noise and preserving phase [39]. Using this algorithm, we are able to track over extended periods of time the spatiotemporal profiles of early stage alternans with quantifiable specificity and sensitivity.

Aim 1.2: Examine essential evolution characteristics of early "fine" alternans for arrhythmia predictions

With the alternans detection algorithm, our goal is to identify the essential characteristics of alternans evolution that could be closely linked to the later progression of VT/VF. No such imaging or software tools meeting our needs have been published previously.

Aim2: **Examine the effects of cellular coupling on the spatiotemporal evolution of intracellular Ca^{2+} alternans in cardiac tissue.**

Cellular coupling is critical for maintaining synchronization of exciation and repolarization between cells and could affect the spatiotemporal evolution of intracellular Ca^{2+} alternans. We propose to experimentally perturb coupling in either direction by subjecting homogeneous myocyte monolayers to 4-phenylbutyrate (4PB) for increasing coupling [30] and to heptanol for decreasing coupling [31]. The resultant coupling will be quantified using mathematical interpretation of results from a macroscopic version of fluorescence recovery after

photobleaching (FRAP) applied to a network of cells rather than a single cell. Functionally, the spatiotemporal profiles of calcium alternans as function of cell-to-cell coupling will be assessed by optical mapping. A mathematical model will be employed to validate and expand the experimental results. This will be the first investigation of spatiotemporal evolution of intracellular Ca^{2+} alternans under a range of coupling conditions, including augmented coupling.

Aim3: Formulate a theoretical framework for the mechanisms of evolution of Ca^{2+} alternans in cardiac tissue under various cell-cell coupling conditions and different voltage-calcium dynamics

Computer simulations [3, 32] have revealed that SDAs can be induced in homogeneous tissue purely by dynamic factors, e.g. local intracellular Ca^{2+}-V_m kinetics [40]. Our experimental results indicate that cellular coupling plays a vital role in the spread of instabilities in Ca^{2+}/V_m. Therefore, we use computer models to verify and interpret the experimental alternans evolution patterns under different coupling conditions and variable Vm – Ca^{2+} dynamics.

Additional factor that can add heterogeneity over space-time is the emergence of “virtual electrodes” – common in electrical pacing and cardioversion as a side-effect of the induced electric fields. To address the question whether such field perturbation influence in a substantial manner the evolution of Ca^{2+} instabilities in cardiac tissue, we have developed a new optical pacing method – extending optogenetics (the use of light-sensitive ion channels) to the heart. We studied fine-scale Ca2+ instabilities under traditional electrical and new optical stimulation to reveal the robustness of our findings.

Fig.1 Origins of T-wave alternans[2]. The figure describes how alternans is reflected from cellular level to tissue level and body level. The MTWA in ECG signal origins from SCA or SDA in tissue level, in which APD alternans are spatially in the same phase or out of phase.

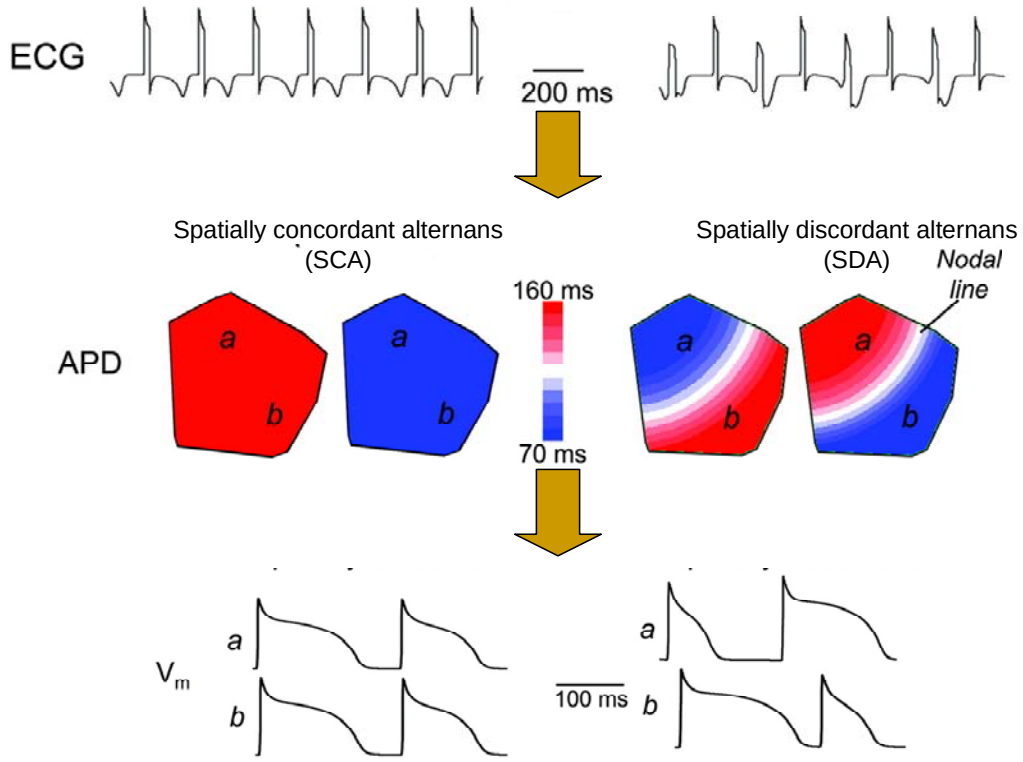

Fig.2 mutations of the RyR2 gene in CPVT (closed symbols) and its function [41]. Panel A shows the mutation form of cardiac ryanodine receptor channel, which is responsible for 50%-55% of cases of CPVT. Panel B, shows how RyR2 works in cardiac myocyte excitation–contraction coupling.

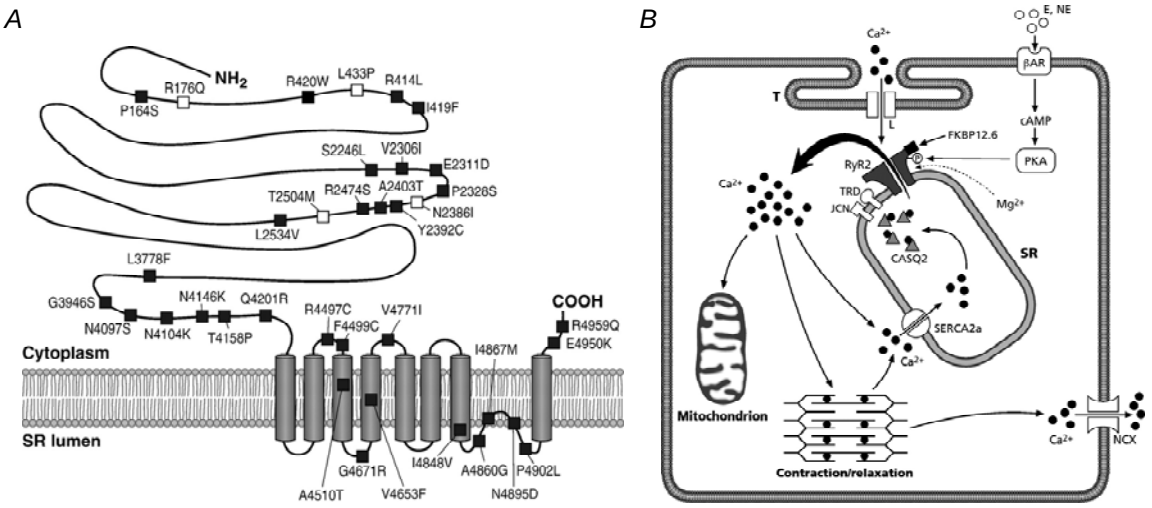

Fig.3 Uncertainty in detection of alternating signals. Panel a: Uncertainty in the bifurcation point: as a bifurcation parameter increases, a critical transition takes place, e.g., transition from a 1:1 response to 2:2 response to external perturbation. For a given system's dynamics and in the presence of noise (including natural variability), there exists an uncertainty zone, for which it is challenging to determine the exact state of the system. Panel b: Uncertainty in transition zones between opposite phases of oscillation: over space, it is possible for neighboring regions to exhibit opposite phase of alternation. Between them a "nodal line" or no-alternation zone must exist. In real experiments, the width of this zone will depend on the system's dynamics and the noise in the system. Panel c: TP of alternation in white noise: maximum-length alternating sequence, *m*, in a random binary signal of length *n* (left); TP of alternation in a random binary signal of length *n* (right). Presented empirical data (10 000 trials per point) show 95% confidence interval for *m* and TP. Based on these data, a threshold TP for alternans detection can safely be chosen above the curve (right).

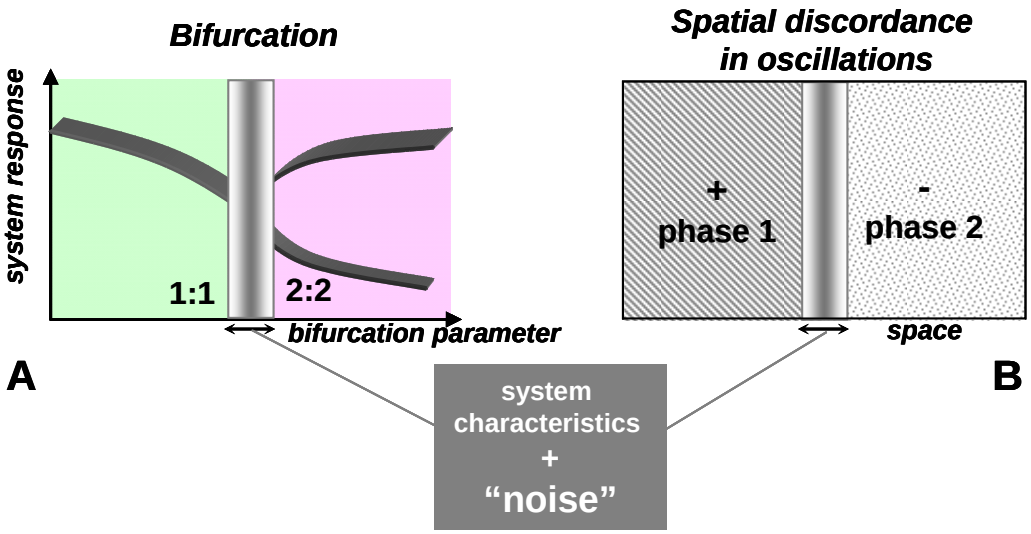
Bifurcation
system response
1:1
2:2
bifurcation parameter
A
Spatial discordance
in oscillations
+
phase 1
-
phase 2
space
B
system
characteristics
+
“noise”

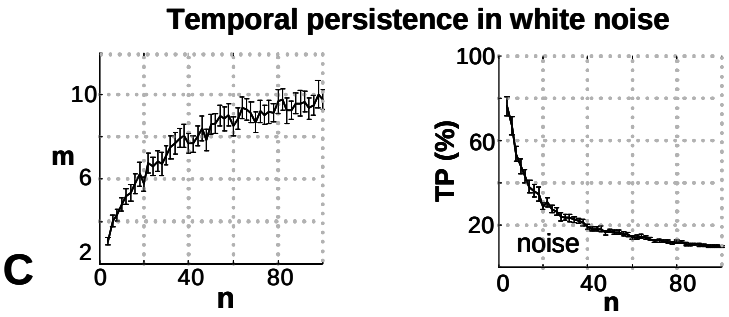
Temporal persistence in white noise
C
m
10
6
2
0
40
80
n
TP (%)
100
60
20
noise
0
40
80
n

Chapter 2

DETECTING SPACE-TIME ALTERNATING BIOLOGICAL SIGNALS CLOSE TO THE BIFURCATION POINT

2.1 Abstract

Time-alternating biological signals, i.e., alternans, arise in variety of physiological states marked by dynamic instabilities, e.g., period doubling. Normally, a sequence of large-small-large transients, they can exhibit variable patterns over time and space, including spatial discordance. Capture of the early formation of such alternating regions is challenging because of the spatiotemporal similarities between noise and the small-amplitude alternating signals close to the bifurcation point. We present a new approach for automatic detection of alternating signals in large noisy spatiotemporal datasets by exploiting quantitative measures of alternans evolution, e.g., temporal persistence, and by preserving phase information. The technique specifically targets low amplitude, relatively short alternating sequences and is validated by combinatorics-derived probabilities and empirical datasets with white noise. Using high-resolution optical mapping in live cardiomyocyte networks, exhibiting calcium alternans, we reveal for the first time early fine-scale alternans, close to the noise level, which are linked to the later formation of larger regions and evolution of spatially discordant alternans. This robust method aims at quantification and better understanding of the onset of cardiac arrhythmias and can be applied to general analysis of space-time alternating signals, including the vicinity of the bifurcation point.

This chapter is based on published work [42]. Thanks to Emilia Entcheva and Harold Bien for giving valuable advice and support during the algorithm development.

2.2 Introduction

Feedback-regulated systems often exhibit damped oscillations in response to perturbations until the limit of control is reached at which critical juncture the amplitudes can rapidly progress to wildly fluctuating values. At the brink of departure from stable conditions, (subtle) oscillations may persist, serving as a potential predictor of dynamic instability. Many

biological processes feature negative feedback control and behave similarly. In spatially extended systems, persistent time-alternating signals, i.e. alternans, can appear as a sequence of large-small-large transients, and can display variable amplitude and variable patterns over time and space, including spatial discordance (alternation with opposite phase). Upon entry in period doubling regime, i.e. in the immediate vicinity of the bifurcation point, the alternans amplitude is typically very small [43] and thus alternans detection is extremely challenging due to spatiotemporal similarities with white noise. Fig.3 illustrates such uncertainty zones expected at the bifurcation point and/or at the border of phase reversal over space. In both cases, very small amplitude alternation (comparable to noise) would be expected. No previously published detection methods have tackled these uncertainty regions in space-time, particularly for limited-duration signals.

For example, excitable tissues (heart, brain, muscle) are biological systems susceptible to dynamic instabilities, e.g. period doubling. In the heart, capturing early bifurcation events (frequency being the control parameter) may translate in early diagnosis of life-threatening events. The onset of some arrhythmias, such as VT and the more malignant VF, has been linked to the development of alternans at the cellular level [44-46] and alternans in the clinical records (ECG). Computerized algorithms based on spectral and nonlinear methods made possible the detection of microvolt-level T-wave alternans, barely discernible in ECG records [47, 48]. These subtle T-wave alternans were found to correlate with future arrhythmia occurrence in some disease conditions, e.g. post-myocardial infarction [49]. While the detection of microvolt alternans has been a major accomplishment and cannot be undermined, there are several facilitating factors, including typically long records and no need for preservation of spatial/phase information. At the cellular level, such instabilities of small amplitude may develop even earlier

and may be buried in noise and have easily dismissible speckled spatial appearance due to inherent biological variability and lack of spatial synchronization close to the bifurcation point.

In spatially-resolved measurements, the detection of alternans has to meet additional challenges: it is informative to track not only their existence (as in T-wave analysis), but also their magnitude and phase for each beat at each spatial location. Preserving phase information is necessary for identification of SDA, Fig.3B. SDAs can precipitate or coexist with reentrant waves [50] and are more closely associated with the development of reentrant ventricular arrhythmias, irregularities in the ECG and sudden cardiac death [44, 51, 52].

In this report, we tackle the general question of uncovering subtly alternating signals over time and space in conditions of noise and/or low amplitude alternation (as illustrated in Fig.3). We present a new approach for automatic detection of alternating signals in large spatiotemporal data sets by quantifying temporal persistence and preserving phase information. The technique is validated by combinatorics-derived probabilities and empirical tests with white noise. This robust new method can be useful in quantification and better understanding of the onset of cardiac arrhythmias and in general analysis of space-time alternating signals, including response to perturbations in the vicinity of bifurcation points or high noise conditions.

2.3 Materials and Methods

2.3.1 Primary Cardiac Myocyte Isolation and Culture

Neonatal rat ventricular myocytes were used because of their high plasticity and ability to reconnect into a tissue-like syncytium after dissociation from tissue. The cells were isolated and plated as previously described (44). Briefly, cardiac tissue from the ventricles of three-days-old neonatal Sprague-Dawley rats was excised after surgery to open the chest cavity. The tissue was

washed of any blood and minced into small pieces for enzymatic digestion over night with trypsin (1mg/mL, 4°C, USB, Cleveland, OH), then collagenase 1mg/mL, 37°C, Worthington, Lakewood, NJ) the following morning. After ninety minutes preplating to remove the cardiac fibroblasts, myocytes were plated at high density (4×10^5 cells/cm^2) onto fibronectin-coated PDMS (Sylgard 184, Dow Corning, Midland, MI) scaffolds. Cells were maintained with 5% CO_2 at 37°C with 10% fetal bovine serum (GIBCO Invitrogen, Carlsbad, CA) supplemented medium M199 (GIBCO) for days one and two after plating, then switched to 2% serum supplemented medium changed every other day.

2.3.2 Macroscopic Optical Mapping and Analysis

Optical mapping of intracellular calcium (using fluorescent dye Fluo-4) will be performed on day 6 after culture using an intensified CMOS camera (1280*1024 pixels at 200 fps, FOV of about 2*2 cm) at room temperature in standard Tyrode's solution. Spatial imaging resolution after 2*2 binning will be (44*44 μm in x-y). Pacing will be applied via a platinum line electrode, and shows an actual optical signal from a pixel after pre-processing.

A series of advanced methods will be applied for data pre-processing using custom-designed software in Matlab (MathWorks, Natick, MA). Signal filtering will include temporal Savitzky-Golay filter (2nd order, 7 frames window) and spatial Bartlett filter (3 pix kernel). In preliminary tests, these have been found to introduce minimal distortion in our data. After baseline subtraction and enhancement of contrast, each beat will be automatically detected by time of activation. Further automated detection of peak height of calcium transients will be done for all spatial locations (pixels) over all beats to form 3D data sets.

2.4 Theoretical basis of the algorithm

Automatic detection of alternating sequences in noise-containing non-stationary signals has to address the possibility for false identification due to random noise-related and/or short-lived alternations. For simplicity, we examine the case of binary alternating signals, since the peak calcium transient sequences can be binarized.

From combinatorics, one can derive the probability of a given binary data set with length n to exhibit uninterrupted alternating pattern with length m. Intuitively, there are a total of 2^n possible binary strings of length n. Further, we consider all possible positions and bit assignments of the m-bit alternating sequence within a binary string of length n, if m can fully fit into the n-sequence only once. A given alternating sequence of length m can be positioned (n-m+1) different ways within a binary string n, depending on where it begins.

As Panel B in Fig.5 shows, if we first consider only central positioning of m, excluding the two border locations, the number of possible positions becomes (n-m+1-2), i.e. (n-m-1). In order to ensure that the alternating sequence does not extend beyond the specified length m, the two flanking bits must duplicate the first and last value of the alternating sequence in order to break the pattern, hence instead of (n-m) bits, we have (n-m-2) unassigned bits, resulting in 2(n-m-2) possible bit assignments. Also there are two alternative forms for the m bits, i.e. phases, of the alternating sequence: (‘1, 0, 1, 0…’ or ‘0, 1, 0, 1…’). Thus the possibilities for centrally positioned m-sequence within n are:

$$p_c = 2*(n-m-1)*2^{(n-m-2)} \qquad (1)$$

If we consider now any of the two border locations of the m alternating sequence within the n bits, because of the one reserved flanking bit, there are (n-m-1) bits left to assign values to,

i.e. 2(n-m-1) possible bit assignments. Considering the two border position and the two phases of the m-sequence, we get the possibilities for the border positions of m:

$$p_b = 2 * 2 * 2^{(n-m-1)} \tag{2}$$

Adding Eqns. (1 and 2), gives all possible cases of m-bit sequence positioned within an n-bit sequence:

$$\begin{aligned} p &= p_c + p_b = \\ &= 2 * (n-m-1) * 2^{(n-m-2)} + 2 * 2 * 2^{(n-m-1)} \\ &= (n-m-1+2^2) * 2^{(n-m-1)} = \\ &= (n-m+3) * 2^{(n-m-1)} \end{aligned} \tag{3}$$

Finally, we obtain a closed-form expression for the probability of having an uninterrupted alternating set of strictly m bits in a random n-bit sequence:

$$P(m,n) = \frac{(n-m+3) * 2^{(n-m-1)}}{2^n} \qquad (n > m > \frac{n}{2} > 2) \tag{4}$$

As Fig.5 shows, (A) Time-alternating signals are identified based on their temporal persistence (TP). From the original traces (synthetic signal is shown for simplicity) a representative signal parameter is extracted, e.g. peak height of calcium concentration. Then derivative and sign are taken along the time dimension to accentuate the alternating patterns and the signal is binarized. Interruptions in alternating patterns are found by locating the zeros after another derivative. (B) Derivation of Equation 4: The denominator is 2^n - all possible combinations of a binary string of length n. For the numerator: a given alternating sequence of length m can be positioned in (n-m-1) positions with (n-m-2) unassigned bits (central case), or positioned in 2 positions with (n-m-1) unassigned bits (border case).The sum of both cases gives the total number of possibilities.

Eq. 4 is valid under some assumptions, e.g. if m has a minimum length exceeding the half-length of n. For short strings of m with respect to n, i.e. for m<n/2, Eq. 4 has to be modified to avoid miscounting of multiple occurrences of m within n.

In this study, we illustrate the detection strategy using spatiotemporal records of intracellular calcium transients in cardiomyocytes. The original records can be binarized and Panel A in Fig.5 illustrates the typical steps in calculating TP; the theoretical curve (Eq. 4) is plotted in Fig 6A. The prototype of this algorithm has been introduced in a conference proceedings form [53].

2.5 Specificity and sensitivity

Spatially-resolved measurements of alternans prompt considerations of relative phase over space, i.e. spatial concordance/discordance needs to be identified. SDAs can be recognized as neighboring regions alternating with opposite phase. The determination of phase is not trivial since the alternating sequence can be easily corrupted by noise. It becomes critical to determine a phase which can be representative and consistent between different spatial locations. Based on the TP concept, we introduce representative phase (RP) derived in time-overlapping segments for different spatial locations to help identify SDAs (Panel B in Fig.6); RP assumes values of -1 or +1.

Temporal persistence criterion is used as means of improving specificity and sensitivity in detection of subtle alternans. Previous studies of cardiac alternans in space-time have exclusively dealt with amplitude of alternans well above the noise level. Typically ad hoc signal duration is chosen and 100% compliance within that signal is required for positive detection of alternans [44, 52, 54]. In contrast, the focus of this research is on formalizing the criteria for

alternans detection and on uncovering subtle alternating signals, close to the noise level, as in Fig 3. These are of special interest as potential early indicators of destabilization.

Empirical testing of the algorithm was performed using uniformly distributed pseudo-random numbers, generated in Matlab. To be comparable to the experiments (considering total number of observed pixels), 40 000 random data sets were created as noise samples, having 4 to 40 beats. After processing the noise data with our alternans identification algorithm, we obtained results perfectly matching the theoretical predictions. We plot in Fig 6A the percent of false positive detections versus signals' total length n for TP≥60%, 75% and TP≥90% as thresholds. Theoretical (Eq. 4) and empirical results (random data sets with white noise) are shown to match perfectly. For example, if a line is drawn parallel to the x-axis at p=0.05, one can determine that there is only 5% chance for random noise to be falsely identified as alternans for signal length n=13 beats, of which m≥8 beats (TP≥60%) form an uninterrupted alternating sequence. Conversely, such temporal sequence would be classified as alternans at TP=60% with 95% confidence. Overall, theoretical and empirical data from Figure 6A can be used for rationally deriving a TP threshold in alternans identification.

If a total signal length of at least n=25~30 beats can be guaranteed, then identification of alternans can be done at TP≥60% with >99% confidence (Figure 6A). In fact, for such long records even TP≥40% would suffice for >95% confidence of detection. Thus lowering the TP threshold (from the conservative 100%) can be done without compromising the specificity of detection.

Even if the calculated signal TP is below some pre-set threshold for confirming alternans, the TP value itself is still a powerful measure of the level of organization and probability of consistent alternation compared to that seen in a random signal. Table 1 shows side-by-side TP

calculated for white noise traces and TP from actual calcium records of the same length. At low pacing frequencies, where no alternation is expected, the TP for the calcium records is undistinguishable from noise. Signal length predictably lowers the TP in noise traces (as per Figure 3C). Increasing pacing frequency gradually increases the TP index in the calcium traces and makes it statistically higher than that seen in noise records with comparable length. Thus even TP levels below threshold are informative for the physiological response of the system and the gradual recruitment of alternating spatial sites.

For analysis of alternans at multiple spatial locations, we apply the concept of representative phase (RP), illustrated in Figure 6B using TP=60% for simplicity. Pixels A and B are selected to belong to different spatial regions. Pixel A exhibits uninterrupted alternation in the (t1 – T2) time interval, while pixel B alternates continuously in the (T1-t2) interval. For TP≥60%, there will be at least 20% temporal overlap for different spatial locations, allowing the determination of a representative phase (RP) in the [t1 t2] interval; RP is used for identification of SDAs.

An important question is how different signal-to-noise ratio (SNR) conditions affect the performance of the proposed strategy, especially when the alternans are very subtle (low alternans ratio, AR, see Methods). We address this question in Fig.7, where variable SNR was created by adding white noise to 4 perfect alternans sequences (TP=100%, n=30) having AR=6%, 10%, 20% and 50%. As noise level increases, SNR decreases (right-to-left on the x-axis), detected TP drops following a sigmoid curve. If the alternans detection threshold is set at TP≥60%, all signals with SNR below the crossing point with the dark horizontal line will be misclassified (false negative); as expected, signals with very subtle alternans (low AR) are more sensitive to noise resulting in more false negatives. While Figure 6A illustrates the specificity of

the algorithm as function of TP and signal length, Figure 7 helps assess its sensitivity as function of AR and SNR. Setting TP threshold lower than 100% increases sensitivity, i.e. allows detection of alternans at lower SNR; for example at SNR=30 is possible to detect alternans with AR=6%, while requiring TP=100% would not allow that.

As Fig. 7 shows, (A) Variable SNR was generated by adding white noise to 4 perfect alternans sequences (TP=100%) of length n=30, having different AR=6%, 10%, 20% and 50%. Curves show 95% probability of detecting alternans of different AR at the corresponding SNRs and TP values. For TP≥60%, all signals with SNR below the cross point with the dark horizontal line will be misclassified (false negative). Setting TP<100% increases sensitivity, i.e. allows detection of alternans at lower SNR. (B) For low (left) and high (right) SNR, the 95% sensitivity limit of detection is shown at three different TP thresholds. Y-axis scale (ARs) is different for low and high SNR. Alternans in the area above the curves will be obscured by noise, while detecting alternans is safe with 95% sensitivity under the curves.

2.6 Experimental validations

Strong cell-to-cell coupling in cardiac tissue does not guarantee spatial synchronization at the bifurcation point. Due to inherent cellular variations in electrophysiological properties, different spatial locations may enter a period-doubling regime at different values of the bifurcation parameter (frequency, in this case), thus creating intricate spatiotemporal patterns, which can be revealed only at very high resolution mapping. To test this, we applied our algorithm to high-resolution optical mapping of intracellular calcium in thin long strips of cultured cardiomyocytes, subjected to electrical pacing at progressively increasing frequency starting from 1Hz. For consistent results, in the alternans analysis, 30 beats were used for each

pacing frequency, so that at TP≥60%, the confidence level in alternans detection (specificity) was >99% (Figure 6A).

With increasing pacing frequency, the number of locations (pixels) exhibiting alternans gradually increases, Fig. 8 A, B. The gray scale in Panel A represents the degree of alternation, AR; white areas are without alternans. The images in the left column show the spatial localization of alternans identified by the current algorithm over 30 beats using TP≥60%. For comparison, the middle and the right column present maps of alternans if only the first 8 or the last 8 beats are considered and 100% compliance (8 out of 8) is imposed, as done in a recent study [54]. Despite similarities in structure, the alternans regions uncovered by the different approaches are not identical. The spatial alternans map for the final 8/8 beats (right column) bears more similarity to the results from our approach compared to the first 8/8 beats (middle column). This is most likely due to the more transient response during the first 8 beats after change in pacing frequency and achievement of steady-state towards the end. The different spatial maps for the first and the last 8 beats highlight the dynamic nature of alternans and their dependence on the particular pacing protocol (in [54] only 8 (transient) beats were analyzed). Interestingly, by Eq. 5, the longer examined sequence by our approach (30 beats) yields higher specificity of detection than the 8/8 method despite the lower chosen TP threshold and regardless whether the signal is at steady-state or not.

Frequency-dependent increase in alternans is further illustrated in the time domain for two selected spatial locations – A and B, Fig. 8 B. For these two locations, the algorithm reports no alternans (TP<60%) for pacing frequencies up to 2.78Hz. Then, at 2.78Hz, only point B shows persistent alternans, while at 3.12Hz, the two neighboring locations start alternating out-

of-phase, i.e. they form a small-scale (microscopic) SDA region. In the original traces (bottom row) these small-magnitude SDAs for points A and B are discernable.

Displaying alternans regions by their respective phase (RP*AR, %) reveals the nature of local organization as different spatial locations start alternating, Fig.9 A. Left column displays all confirmed locations of alternans in peak calcium (TP≥60%) as frequency increases, while the right column shows only SDA regions identified based on proximity criterion. Upon increasing pacing frequency, both peak calcium concentration and the duration of calcium transient change in the same direction, hence the product of the two can be used to improve SNR and the detection of alternans; Figure 9B shows this enhanced version of the data from Fig.8A. It is apparent, that higher frequency not only recruits more alternating regions, but also increases the yield of SDA regions. At 2.78Hz, the tissue is largely alternating in-phase as a contiguous region, but the presence of a small number of pixels mildly alternating out-of-phase (blue) leads to the identification of SDAs. At even higher pacing frequency - 3.12Hz – the tissue clearly breaks in local SDA regions with complex shape.

Alternans targeted specifically by our algorithm fall in the uncertainty zones depicted in Fig.3, and are shown in Figure 9A & B; they are subtle (AR<20%), and can easily be missed if insufficient imaging resolution is used. Speckled spatial maps of alternans as shown here have not been reported even for similar experimental systems. For comparison, in Fig.9 B we show a different sample where more familiar contiguous regions of large amplitude alternans (AR>50%) with sharp nodal lines of no alternans between them exist. Spatial maps like the one in Figure 9C are more typical of previous reports [52, 54] – such large AR alternans can be easily detected by a variety of methods. In contrast, subtle alternans with low-amplitude and high spatial frequency

normally are dismissed by conventional imaging and analysis tools due to spatial averaging (insufficient spatial resolution) and/or insufficient sensitivity of the analysis algorithms.

2.7 Discussion

An important transition in the system's dynamics to a qualitatively different state occurs at the bifurcation point. Capturing this transition is highly desirable, as illustrated, for example, by recent interest in defining the type of bifurcation in cardiac tissue [55]. Knowing if a border collision vs. pitchfork period doubling bifurcation takes place may yield a better understanding of the inherent structure of the system – continuous vs. piece-wise continuous (hybrid).

Quantification of properties in the immediate vicinity of the bifurcation point, however, is extremely challenging due to noise-like behavior over time (small amplitude alternations may be buried in noise) and space (bifurcation threshold may vary between cells and yield a speckled spatial appearance), Fig.3. Previous studies have dealt with more prominent high AR alternans – away from the bifurcation point, and have employed mostly ad hoc selection of the temporal sequence length needed to confirm alternans by imposing 100% compliance within that length. The limits of detection form statistics point of view (confidence in detection) have not been determined before. This requirement may be too conservative and lead to inferior sensitivity in the presence of noise compared to the method proposed here, Figure 7. This deficiency in sensing subtle alternans does not necessarily come with superior specificity (depending on signal length). For example, specificity for the (8/8) method of identifying alternans [54] is 99.41%, while a TP-based strategy, requiring 18 out of 30 beats yields 99.997% specificity. Furthermore, if sufficient knowledge exists about the acquisition system (SNR and expected AR), TP index (even <60%) can be selected to obtain optimal specificity and sensitivity, guided by Figures 6

and 7. The detection limit (lowest possible AR) of the algorithm will depend on the SNR, which may be also affected by the bifurcation parameter, like SNR, shown in Tables 1 and 2.

Table.1 Frequency affects the SNR for alternans detection

Frequency (Hz)	1.66	2.21	2.45	2.78	3.12
SNR	46.6	42.5	35.1	28.1	25.0

Table.1 shows the SNR decrease with increasing pacing frequencies. This is due to the general decrease in calcium transient magnitude and duration with higher frequency - less time for the sarcoplasmic reticulum (SR) to refill with Ca^{2+} and less subsequent Ca^{2+} release.

Table.2 Limits of sensitivity (%) in alternans detection under various SNR and AR combinations

AR \ SNR	25	30	35	40	45
3%	14.21	24.28	38.36	53.51	68.30
4%	33.73	55.23	73.99	89.33	**97.96**
5%	60.05	82.96	**96.73**	**100**	**100**
6%	84.07	**98.67**	**100**	**100**	**100**
7%	**97.12**	**100**	**100**	**100**	**100**

Table.2 shows the adaptive sensitivity of the proposed alternans detection approach under SNR typically encountered in our system. At lower pacing frequencies, alternans are not present or exhibit low magnitude (low AR), yet SNR is high and allows for good detection down to AR

of 4%. Higher pacing frequencies are more likely to push the system away from the bifurcation point and to produce larger AR alternans; SNR decreases, yet the detection limit still remains quite good – AR=7% for SNR of 25. In general, this method allows exploration of rather subtle alternans (AR<10%).

The approximate limit of our system in detecting calcium alternans in large cell monolayers (2.5cmx2.5cm) with spatial resolution of 44um is AR=4-7% depending on frequency. In comparison, for T-wave alternans detection in 12-lead ECG, the equivalent AR varies between 1-65% [56-58]. However, in such analysis much longer event sequences are employed – typically >100 to 2000 or more beats [56, 58, 59]. Such long sequences combined with advanced spectral analysis make possible the detection of alternans for lower AR. Our algorithm targets cases, where relatively short signals (<30 beats) can be used and phase information is of interest.

Preservation of phase information (RP) at different spatial locations, offers automated identification of spatially-discordant alternans. Large-scale SDAs have been more directly linked to complex local dynamics [50, 60], pronounced alternations in the ECG signal, e.g. alternating QRS complex [51], and identified as a possible path to induction of spiral waves in VT and VF [52, 61]. Calcium alternans and especially SDAs occurring over a small (subcellular) spatial scale have been only recently suggested by computational studies [62] and experimentally confirmed in a tissue setting [63]. The imaging and analysis strategy presented here allow tracking of the early evolution of such subtle alternans over a large field of view (Figures 5 and 6) - essential in the study of reentrant arrhythmias occurring over centimeter scale. We found that initially sporadic small-AR spatially concordant alternans become more pronounced with pacing frequency and consolidate in larger regions, followed by complex-shape SDAs at even higher

pacing rates. A deterministic continuous model for alternans generation in a reaction-diffusion system [61, 64] would have predicted large well defined regions of SDAs (as in Figure 6C). Instead, at this early stage we observe more speckled SDA patterns, which could be linked to inherent heterogeneities, revealed only when imaging at sufficient spatial resolution and using high-sensitivity analysis. Ability to identify alternating signals and their phase permits exploration of spatiotemporal patterns at the bifurcation point. Because of the general nature of the algorithm, it can be applied to identification of any potentially alternating dynamic signals (cardiac or not).

Fig.4 Experimental setup and pacing protocol. Panel A: Experimental setup: cardiomyocytes are cultured on rectangular strips and paced during experiments with a line electrode on one side. A pre-processed Ca2+ fluorescence intensity signal from a single pixel is shown. Panel B: Cells were paced at several frequencies following a dynamic restitution protocol - frequency was varied from 1Hz to 2Hz in 0.5Hz steps and thereafter in 0.2Hz increments. At each pacing frequency, steady state is achieved by pacing for 60 beats, and then record 30 transients.

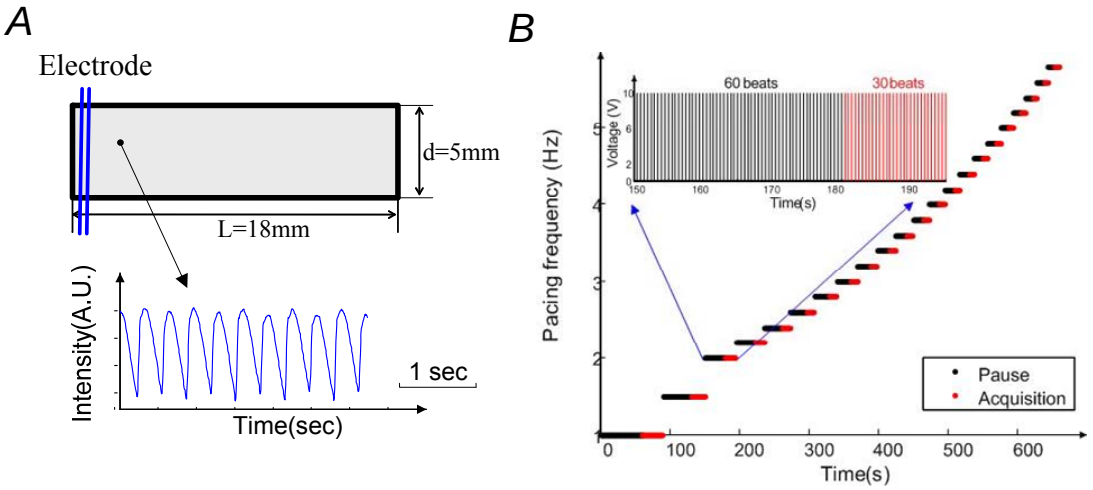

Figure 5. Identification of time-alternating signals and derivation of Equation 4. Panel A: (b) Time-alternating signals are identified based on their TP. From the original traces (synthetic signal is shown for simplicity), a representative signal parameter is extracted, e.g., peak height of calcium concentration. Then derivative and sign are taken along the time dimension to accentuate the alternating patterns and the signal is binarized. Interruptions in alternating patterns are found by locating the zeros after another derivative. Panel B: Derivation of 4: the denominator is 2^n all possible combinations of a binary string of length n. For the numerator: a given alternating sequence of length m can be positioned in $(n-m-1)$ positions with $(n-m-2)$ unassigned bits (central case), or positioned in two positions with $(n-m-1)$ unassigned bits (border case). The sum of both cases gives the total number of possibilities.

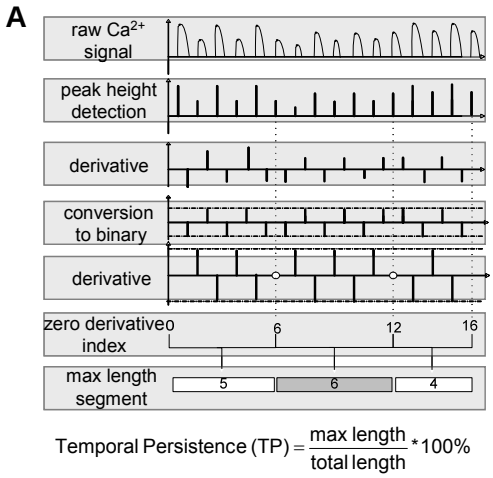

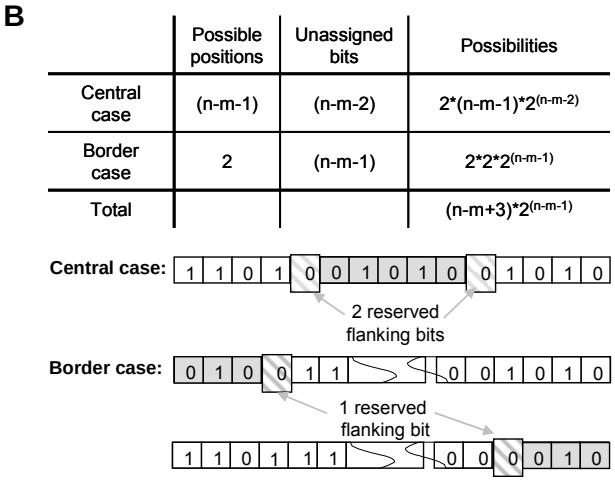

Figure 6. Specificity of alternans detection based on temporal persistence (TP). Panel A: Specificity of alternans detection: the stars are the theoretical probabilities (5), while the solid lines represent empirical results, computed from white noise datasets. The theoretical and empirical data match perfectly for TP of 60%, 75%, and 90%. Signal length $n \geq 13$ is needed for $p < 0.05$ (≥95% specificity of detection) at TP ≥ 60%, while shorter signals will suffice when enforcing stricter TP thresholds. Panel B: Spatial locations are said to exhibit alternans, if their TP exceeds some critical value, e.g., TP ≥ 60%. Two neighboring pixels A and B satisfying this criterion in the interval from T_1 to T_2, have their uninterrupted alternating sequences in the [t_1, T_2] and [T_1, t_2] intervals, respectively. There will be at least 20% temporal overlap for the different spatial locations, allowing the determination of RP, used for characterization of SDAs.

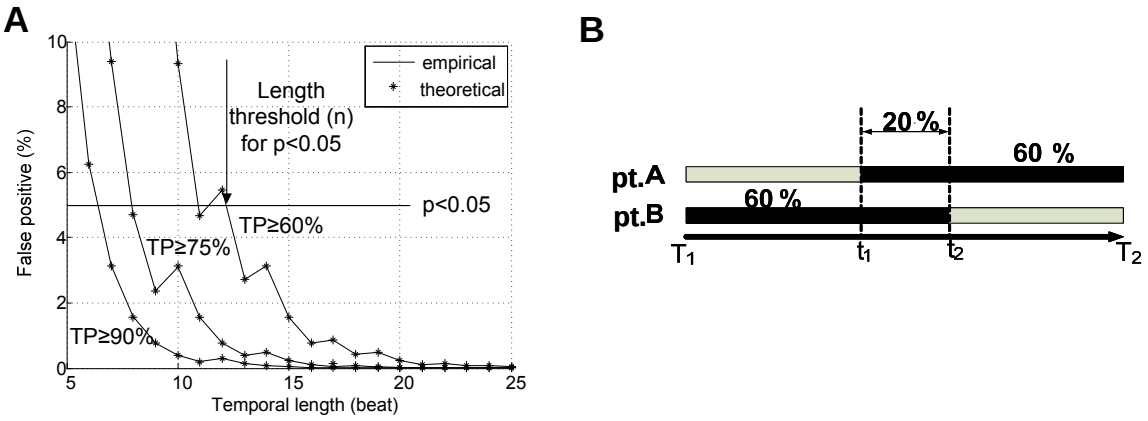

Figure 7. Sensitivity of alternans detection as a function of SNR and AR Panel A: Variable SNR was generated by adding white noise to four perfect alternans sequences (TP = 100%) of length n = 30, having different AR = 6%, 10%, 20%, and 50%. Curves show 95% probability of detecting alternans of different AR at the corresponding SNRs and TP values. For TP ≥ 60%, all signals with SNR below the cross point with the dark horizontal line will be misclassified (false negative). Setting TP < 100% increases sensitivity, i.e., allows detection of alternans at lower SNR. Panel B: For low (left) and high (right) SNR, the 95% sensitivity limit of detection is shown at three different TP thresholds. *Y*-axis scale (ARs) is different for low and high SNR. Alternans in the area above the curves will be obscured by noise, while detecting alternans is safe with 95% sensitivity under the curves.

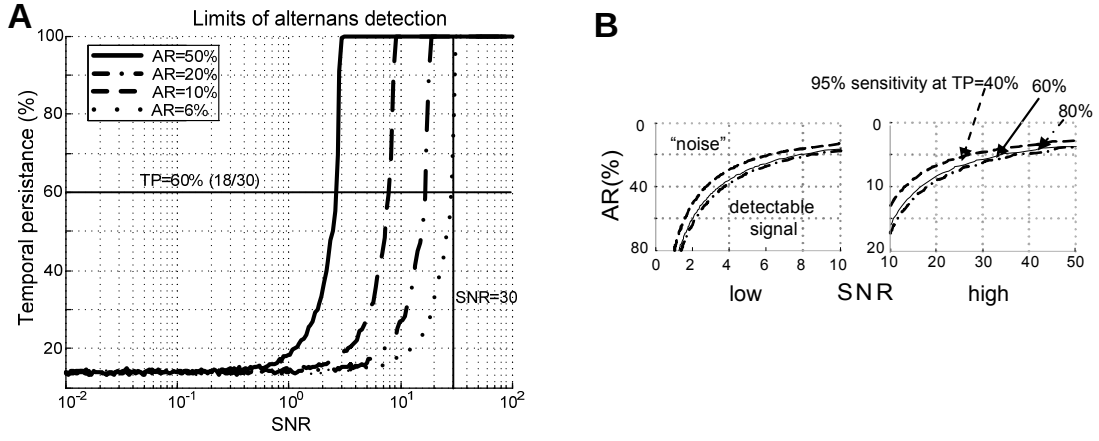

Figure 8. Frequency as control parameter for alternans development in space-time. Panel A: Spatial alternans patterns over different pacing frequencies. Gray scale represents AR with white areas not satisfying the TP criterion. Images on the left are for TP ≥ 60% (18/30 beats); images in the middle and to the right are the result of imposing TP = 100% (8/8 beats), with the eight beats selected at the beginning or the end of the 30 beat record. Panel B: Time series—the original intensity traces and derivatives of peak height in calcium are shown for two selected points A and B over different pacing frequencies. Blue and red in the left column represent the original data for points A and B, respectively. Blue and red in the middle and right column refer to derivative values during odd and even beats, respectively. For a perfectly alternating segment, all odd and even beats should be evenly distributed above and under the zero line, e.g., derivatives for A and B at 3.12 Hz (TP = 100% for both locations).

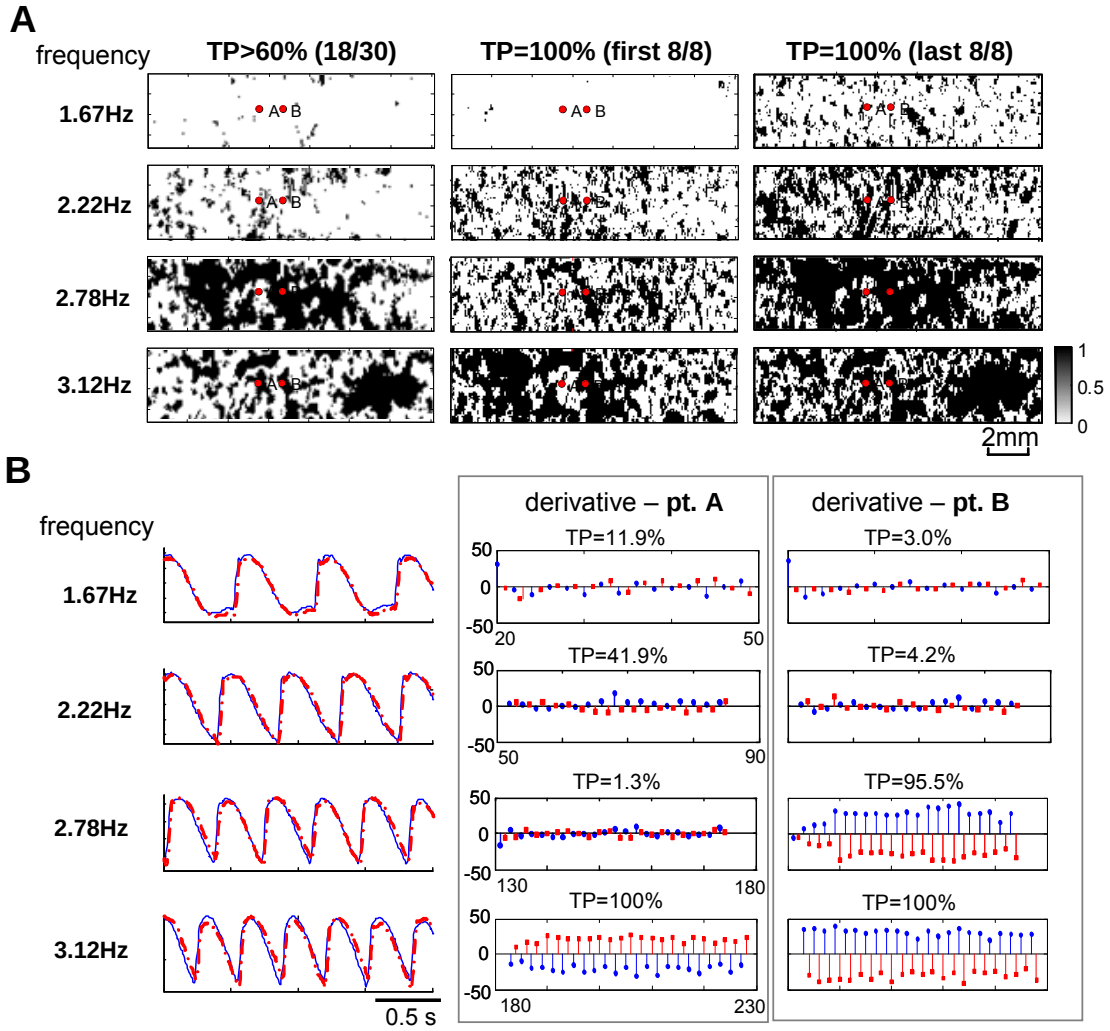
A
frequency
TP>60% (18/30)
TP=100% (first 8/8)
TP=100% (last 8/8)
1.67Hz
2.22Hz
2.78Hz
3.12Hz
A
B
1
0.5
0
2mm
B
frequency
1.67Hz
2.22Hz
2.78Hz
3.12Hz
0.5 s
derivative – pt. A
derivative – pt. B
TP=11.9%
TP=3.0%
TP=41.9%
TP=4.2%
TP=1.3%
TP=95.5%
TP=100%
TP=100%
50
0
-50
20
50
90
130
180
230

Figure 9. Identification of spatially discordant alternans. Panel A: Phase-based identification of SDA patterns over different pacing frequencies. Color shows the magnitude of alternans at different spatial locations, quantified by RP × AR%. Red and blue identify opposite RP; green areas are regions with no detected alternans. Images on the left display all points with confirmed alternans; images in the middle show confirmed SDAs based on proximity criterion. Panel B: Enhancements of alternans by using the product of peak height (PH) and calcium transient duration (CTD) are due to changes in the same direction for both in response to frequency, and lead to improved noise resistance. Panel C: Large-scale alternans (AR ≥ 50) in solid contiguous in-phase regions are shown in contrast to previous examples with low AR and speckled spatial distribution. Two traces extracted from sites A and B illustrate spatial discordance.

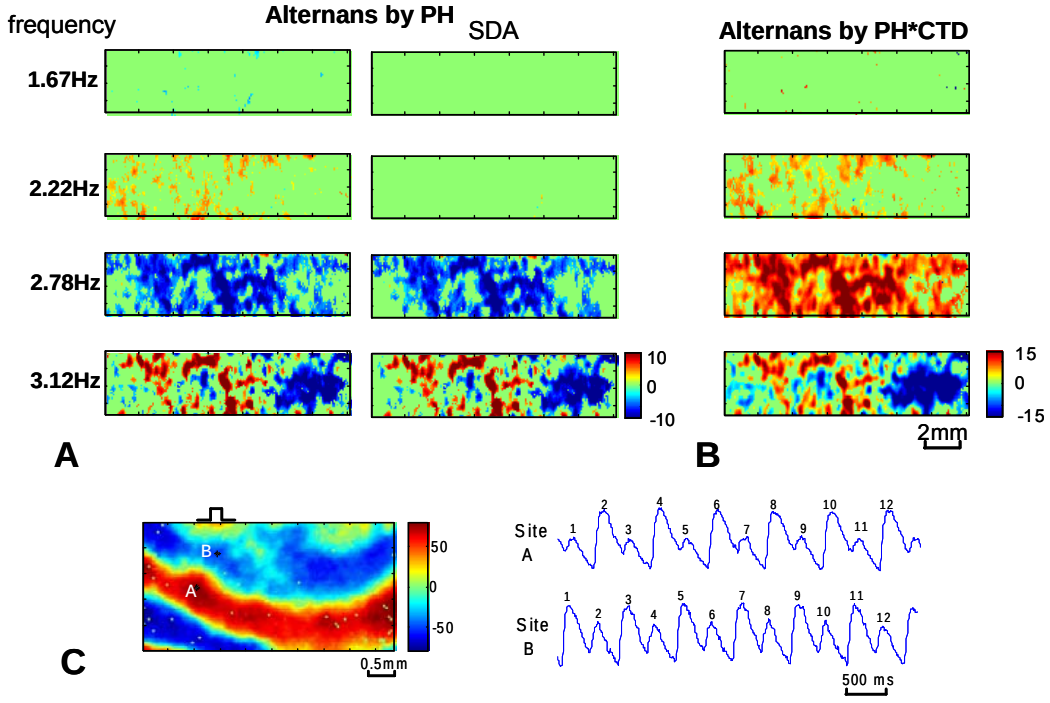

Chapter 3

THE EFFECTS OF CELLULAR COUPLING ON THE SPATIOTEMPORAL EVOLUTION OF INTRACELLULAR Ca^{2+} ALTERNANS

3.1 Abstract

Gap junctions are particularly important for cardiac tissues, as electrical signals need to be conducted efficiently to allow heart myocytes to contract in tandem. The objective of the Aim2 is to explore the effects of cellular connectivity on Ca^{2+} alternans evolution. 4PB and heptanol will be used as suitable perturbations to efficiently change cellular coupling, importantly, in a bi-directional manner (increasing and decreasing). We will investigate how the varied level of cellular coupling, quantified in FRAP experiments, affects the spatiotemporal evolution of intracellular Ca^{2+} alternans (mapped with ultra-high spatiotemporal resolution in response to different pacing frequencies).

This chapter is based on published work [65]. Thanks to Chris Gordon in Dr. Peter Brink for helping with Western Blot.

3.2 Introduction

Recent experimental evidence is increasingly supportive of the important role that intracellular Ca^{2+} dynamics plays as an independent factor[66] in the development of diverse types of arrhythmias in inherited or acquired cardiac pathologies. Early intracellular Ca^{2+} instabilities, e.g. alternans, are now viewed as a prelude to the progression of life-threatening arrhythmias in heart failure[67], long QT syndrome type 2[68], and in catecholaminergic polymorphic ventricular tachycardia (CPVT) [69, 70].

Beat-to-beat alternans is a local (cell-level) phenomenon, revealed when a cell is stressed/driven at above certain pacing rate. The origin of this rate-dependent dynamic instability has been traced to the steepness of the action potential duration (APD) restitution, if voltage (V_m) alternans are concerned[71], or to dynamic Ca^{2+} handling parameters, e.g. the steepness of Ca^{2+} release as a function of Ca^{2+} load[72] or a more elaborate set of conditions[73], if the source of

instability lies with Ca^{2+}. Inherent variability in cellular properties across the tissue is expected to result in different threshold for alternans for each cell. Thus, "seeds" of early alternation can, in theory, form at relatively low rates, and "graded" alternans amplitude can be seen across different cells. Because of the syncytial properties of healthy cardiac myocardium, by virtue of cell-cell electrical coupling via gap junctions and its homogenizing effects, such isolated instabilities are likely to be suppressed for purely voltage-driven alternans, and the tissue is likely to become engaged in alternation only after critical mass of cells reach threshold. The effective wavelength for alternation [74] in such cases is large (on the cm-scale), determined by the high effective diffusion for voltage, D_v.

Instabilities (alternans) driven by intracellular Ca2+ cycling, on the other hand, can form spatially distinct patterns [75-77], due to the much slower effective diffusion for calcium, D_{ca}. Considering the complexity brought about by the electromechanical coupling/feedback (i.e. V_m-Ca^{2+} coupling) in the heart through the Na/Ca exchanger and the L-type Ca^{2+} channels, it is unclear a priori to what degree can "electrical diffusion" (D_v, not D_{ca}) act as a "smoothing" factor in the spatiotemporal evolution of local Ca^{2+} alternans, i.e. if and how does gap junction coupling influence the spread of early cell-level Ca^{2+} alternans?

Cellular coupling is not a parameter that factors in directly into current general theories about alternans origin and evolution. Empirically, thus far it has been shown that:

1) Ca^{2+} alternans can indeed form fine-scale spatial patterns even in intact hearts[75, 77] - a finding that has been corroborated by computer simulations[78, 79].

2) Improved coupling may be alternans-suppressing and anti-arrhythmic [80, 81]. Karma and colleagues used a simplified amplitude equation for excitable tissue to analytically assess the effects of coupling – relating wavelength for alternans pattern formation to electrical diffusion

(D_v) and APD[74]. Yet, previously no clear relationship has been revealed (experimentally or theoretically) between intracellular Ca^{2+} instabilities and cell-cell (electrical) coupling.

In this work, we set out to dissect experimentally the role of electrical coupling in the spatiotemporal evolution of Ca^{2+} alternans at the multicellular level. We systematically varied and quantified coupling in a simplified *in vitro* model of a cardiac syncytium (neonatal rat cardiomyocyte culture) and used ultra-high resolution optical mapping (capable of subcellular resolution over a centimeter-scale) and an alternans detection algorithm to trace experimentally the evolution of Ca^{2+} alternans.

3.3 Materials and Methods

3.3.1 Optical mapping experimental protocol

On days 5-7 after cell plating, myocytes or mixture of myocytes and fibroblasts will be washed, equilibrated at room temperature in Tyrode's solution (1.33 mM Ca^{2+}, 5 mM glucose, 5 mM HEPES, 1 mM $MgCl_2$, 5.4 mM KCl, 135 mM NaCl, 0.33 mM NaH_2PO_4, pH 7.4) and stained for intracellular Ca^{2+} with Fluo-4 AM (Molecular Probes, Eugene, OR, USA). Labeled samples will be transferred to a temperature controlled (30^oC) experimental 35mm chamber perfused with fresh Tyrode's solution. During experiments, cells are stimulated with a Pt line electrode at one end of the scaffold, initiating planar waves. Cells are paced at several frequencies following a dynamic restitution protocol, as shown in panel B of Fig.4. For each frequency, the first 60 beats are paced to achieve steady-state, and then 30 transients are collected for data analysis. Cells in each coupling condition will be paced until 2:1 complete block. Fluorescence calcium signals will be recorded with an intensified camera system (pco CMOS 1280×1024), which is capable of macroscopic imaging in a single layer of cells at 200 fps and at 20 μm/pix within a FOV>2×2 cm.

Because of the relatively long records needed for capturing alternans evolution and the fluorescence type of measurements used here, we have adopted tangential illumination and automated shuttering to avoid photobleaching:

(1) Tangential illumination

The illumination strategy we proposed is able to significantly reduce the intensity of light exposure: excitation light is delivered at 90±15deg with respect to the imaging axis, from tangentially positioned light sources. In contrast to traditional vertical/direct illumination, the fluorophore life-span under tangential distributed illumination is much longer.

(2) Automated shuttering

As an additional step to avoid photobleaching we reduce the time-span of light exposure by custom-developed shutter control software, which automatically synchronizes the illumination light with data acquisition. The illumination light is only turned on during the data acquisition periods.

In order to prove these two methods work, we have conducted a dedicated experiment for examining photo bleaching. As shown in Fig.11, the sample was paced at 1.5Hz for 60 beats without illumination or data acquisition, then illumination light was turned on and 15 beats were recorded. This process was repeated 17 times. The SNR decreased only slightly (11.5%), from 26.45 to 23.40 within the 15 minutes of the experiment. Since we will be using comparable overall durations, these results give us confidence that photobleaching effects will not interfere significantly with our measurements.

3.3.2 Perturbation of cell-cell coupling and Na^+ ion channels

Reduction in cellular coupling was done by acute treatment with very low doses of heptanol (Sigma-Aldrich, St. Louis, MO). Heptanol was diluted in Tyrode's solution to 0.25mM and 0.50mM, and at each concentration samples were perfused for 10min before measurements.

Increase in cellular coupling was done by a small molecule, 4-phenylbutyrate (4PB), which we recently found to act as gap junction agonist[81]. 4PB (Calbiochem, La Jolla, CA) was applied in culture medium at 1mM for 48h at 37^{o}C. We have found that these treatment conditions result in upregulation of Connexin 43.

In a subset of samples (n=4), we tested the effect of sodium channel blocker TTX on wave propagation by applying TTX at concentrations: 0, 0.93, 2.8 and 8.33 M, and measuring changes in conduction velocity during pacing at 1Hz.

3.3.3 Quantification of cell-cell coupling using fluorescence recovery after photobleaching (FRAP)

Cardiomyocyte monolayers were stained with a low molecular weight dye - calcein-AM (Invitrogen, Carlsbad, CA) at 0.5 M for 20 min. Quantification of diffusion properties at the multicellular level was done by a macroscale version of FRAP[82], using Olympus confocal system with its FluoView FV1000 software package. A single cell within the field of view was was bleached out at 100% laser power for 1s, followed by measurements of recovery at 1% laser power (488nm), acquiring data every 1s for at least 120s. An empirical approach was employed, where normalized fluorescence recovery curves were fit with a perturbation-relaxation equation[82, 83] to extract quantitative measures of diffusion. Theoretical analysis[83] reveals than is inversely proportional to the effective diffusion constant and thus to cell-cell coupling.

3.3.4 Experimental measurements of V_m-Ca^{2+} coupling

In a subset of samples (n=16), cells were co-stained for transmembrane voltage and intracellular calcium with di-8-ANEPPS(Invitrogen) and Fura-2-AM (Invitrogen), respectively. Cells were stimulated with a Pt line electrode at one end of the scaffold, initiating a planar wave. Pacing frequency was varied from 1Hz to 2Hz in 0.5Hz steps and thereafter in 0.2Hz increments. Measurements of steady-state response in V_m and Ca^{2+} at the same location were done

sequentially and pacing signal was used to align beats, as previously reported[84]. Fluorescence signals were recorded with a photomultiplier tube at a fixed distance (1.2-1.6cm) from the electrode at a sampling rate of 1kHz. Using an automatic pacing protocol and filter switching, cells were paced up through failure to follow 1:1 (occurrence of alternans or conduction block), and then down, decreasing pacing frequency. Hysteresis was measured as the difference between the frequency of appearance of alternans upon increase in frequency minus the frequency of disappearance of alternans while decreasing frequency (Fig. 12).

3.4 Results

3.4.1 Cellular coupling perturbations by 4PB and heptanol

As an anti-cancer agent, 4-phenylbutyrate (4PB) has recently been reported to be able to promote the expression of connexin 43 (Cx43) [85], which is critical for maintaining synchronization of repolarization between cells. In my dissertation research, we proposed to test the effects of 4PB in a multicellular cardiac preparation and its ability to enhance cellular coupling, focusing on arrhythmia-relevant measures, including alternans.

The detailed protocol for 4PB treatment is: 4PB was diluted in distilled water at 500mM and stored in -20^{o}C freezer. Two days prior to experiments, 4PB was further diluted 1:500 in culture medium (dose determined based on preliminary Western blots) and cells were incubated at 37^{o}C until experiments.

Our immunofluorescence results have confirmed that 4PB was able to promote Cx43 expression. Panel A in Fig.13: Representative confocal immunofluorescence images of both control and 4PB treated samples. Blue indicates nuclei stained by DAPI. And green is the Cx43 marked by immunofluorescence. Panel B: Granulometry-quantified region numbers of Cx43. Panel C: Western blot results of 4 typical control and 4PB treated samples.

No obvious side effects have been found about 4PB, and Fig.14 shows the apoptosis results. Panel A: representative images stained by Calcein (green, live cells), and Ethidium (red, dead cells). Panel B: Viability results of control, 1mM and 10mM 4PB treated samples.

According to published cumulative dose response curve for heptanol [86], significant effects on propagation (conduction velocity, CV) are seen when the heptanol concentration is in the range: from 0.1 mM to 17.8 mM. As heptanol can slow down conduction velocity by blocking cellular gap junctions, the patterns of propagation waves over space for extremely high concentrations may be too complicated for analysis. Therefore, more concentration test points will be intentionally selected from the lower range, as follows: 0.25mM and 0.5mM. From preliminary tests in our lab, we have decided to vary heptanol concentration in a sequence, waiting for 10 minutes for a dose to take effect. Each sample will undergo a full pacing protocol (described later) at each dose. Since the effects of heptanol are reversible, after all recordings are done, we will wash out heptanol, wait for 10 minutes and do another record, just to check for potential remodeling and hysteretic effects.

To conduct FRAP experiment, cardiomyocyte monolayers were stained with 0.5 mM calceine AM for 20 minutes. Data was acquired using the Olympus confocal system with its FluoView 1000 software package. Cells for bleaching were selected with clearly defined borders using a free polygonal drawing tool. Bleaching was carried out at 100% laser power for 1 second while measurements were obtained at 1%. At last, FRAP data was analyzed according to [87], with a subsequent mathematical analysis linking the data to electrical coupling. More specifically, myocytes with good connections to neighboring cells are firstly selected, then bleached with full laser power for 1 sec at t=0s. The recovery fluorescence intensity was recorded for the next 200 sec, but the difference of recovery fluorescence intensity is already

$$F(t) = F_0 + (F_\infty - F_0)(1 - e^{-t/\tau})$$

visible at t=20s between 4PB treated and control myocytes. In order to acquire quantitative results, the normalized fluorescence curves were fitted by perturbation-relaxation equation:

(5)

$F(t)$ is the fluorescence intensity at time t. Correspondingly, F_0 and F_∞ are the fluorescence intensity at t=0 and t=∞. τ is the time constant which indicates the recovery speed.

FRAP experiments (Fig. 15) were conducted to verify and quantify the effects of 4PB and heptanol on cellular coupling. Panel A shows the representative fluorescence images of cardiac myocytes before photo bleaching, just after bleaching and 20s after bleaching. Panel B is average of fitted curves by equations (4). Obviously, at the same time point after photo bleaching, 4PB samples have the highest recovery rate, heptanol samples were slowest. Panel C shows the statistical result of recovery time constant from all 4 groups: 4PB, control, 0.25mM heptanol, and 0.50mM heptanol.

Besides validating the cellular coupling using FRAP, we also checked the condition velocity (CV) under 4PB or heptanol treatment, which is the speed of Ca^{2+} transients transmitted through cardiac monolayer and has been closely linked to cellular coupling. The methodology to measure CV is: as the length of scaffold is much longer than its width (18mm to 2mm), it can roughly be treated as 1D. Then the CV is calculated through least square linear fit over the spatiotemporal plot of the spatial locations along all pixels versus their corresponding activation time for individual beats.

As Fig.16 shows, (*A*) CV measured at 30°C, 1 Hz pacing for each group in the rectangular samples; last bar shows recovery (*wash out*) after heptanol treatment. Error bars indicate standard deviation; (*) significance at $p < 0.05$; the 95% CI for the slope of a regression line was (23.7, 46.9). (*B*) Example activation maps for the four groups; color indicates time of

activation (0 to 0.1 s), isochrones (in *black*) are 0.02 s apart. Ca^{2+} transients are shown from each sample at the * location. (*C*) Estimated relative effects of heptanol on CV via suppression of gNa and via gap junction block. The two diamonds indicate actual measured CV values (as % of control, from panel *A*) for the two heptanol concentrations used here; the three curves show expected reduction in CV via gNa block alone: analytical estimate (*black*), numerical solution (*red*), and our experimental data with TTX block (*blue*). (*D* and *E*) No significant effects of 4PB and low doses of heptanol on Ca^{2+} transients: CTD80 and rise time (mean ± SE) are not significantly different between the groups ($p = 0.34$ for 4PB effects and $p = 0.16$ for heptanol effects on CTD80); power analysis with bootstrapping would have uncovered significant changes if CTD80 were altered by >18.7%.

3.4.2 Alternans evolution under different cellular coupling conditions

With the help of developed algorithm for alternans quantification [88], the evolution profiles in different cellular coupling conditions could be unveiled as Fig.17 shows. **A.** Resolving fine-scale alternans while imaging a large field of view (FOV): (top) space-time plot of persistent (over 55 beats) fine-scale alternation at the cellular and sub-cellular level at 4Hz pacing, detected while imaging FOV = 2.2x2.2 cm^2; color indicates Ca^{2+} alternans ratio (%), multiplied by phase (-1, +1); (bottom) plot of fine-scale SDAs along a line from the same sample. B-D. Representative spatial maps of fine-scale Ca^{2+} alternans at steady-state under different pacing frequencies and cellular coupling conditions: 0.5 mM heptanol (B), control (C) and 4PB samples (D). Pacing electrode is on the right side. Color indicates the amplitude of the alternans ratios (in %) at different spatial locations. Red and blue identify opposite phase; dark green areas are regions with no detected alternans; white areas identify conduction blocks. Traces on the right are from the location identified by a (*) at pacing frequencies 2.8 Hz, 3.4 Hz and 4.0 Hz.

To further investigate the intracellular Ca^{2+} alternans evolution profiles in various coupling conditions, we examined a few more parameters: CV, block frequency, fine pre-threshold alternans area and alternans event frequency. The CV results in Panel A of Fig.18 is merely for verifying the effects of 4PB and heptanol, which should increase and decrease CV respectively. **B:** Break-point frequency (frequency of failure to follow 1:1) as function of the diffusion factor (1/ , s). C**:** Evolution of the areas exhibiting local Ca^{2+} alternans as function of pacing frequency: green for low coupling (0.5 mM heptanol), black for intermediate coupling (control) and blue for high coupling (4PB); arrows indicate the average break-point frequency; error bars indicate standard error. D**:** Space-averaged alternans ratio for early fine Ca^{2+} alternans (< 2Hz) as function of coupling/diffusion. E**:** Area of fine Ca2+ alternation at low frequencies (<2Hz) as function of coupling**.** F: Proportion of samples (%) that exhibited large-scale 2:2 alternans upon break-point frequency (the remaining samples went directly into 2:1 block). Sample numbers for A~F are $n_{0.5\ mM}$=17, $n_{0.25\ mM}$=14, $n_{control}$=28, n_{4PB}=18.

3.5 Discussion

3.5.1 Perturbation and quantification of cell-cell coupling

We employed an *in vitro* model of cardiac syncytium, neonatal rat cardiomyocyte culture, that has been successfully used in addressing a wide range of mechanistic questions related to multicellular cardiac function[89-95]. Currently, there is no completely selective way of systematically perturbing gap junction coupling without affecting other cell/tissue properties. To create a range of coupling conditions, in this study, we chose two perturbations known for relatively high selectivity in their action on cardiac cellular coupling: a classic gap junction uncoupler[96], heptanol, which when used at low doses, as here: 0.25mM and 0.5mM, has negligible effects on excitability, and a gap junction enhancer, 4PB, which we have shown recently to augment cellular coupling in cardiac tissue by upregulating Cx43 [81], similar to reports in other tissues[97, 98]. Coupling under these perturbations was quantified by a

macroscopic version of fluorescence recovery after photobleaching (FRAP) [82, 87, 95], Fig 15A. FRAP measures the diffusion of a low-molecular weight dye (in our case, calcein-AM) to infer coupling via gap junctions. FRAP results are best presented in terms of the time constant of recovery, obtained after nonlinear curve fit to a perturbation-relaxation curve[83], Fig 15B. As intended, we found that perturbation of coupling resulted in a range of values from low (1mM 4PB) to high (0.5mM heptanol), both of which were significantly different from control, Fig 15C. While the exact derivation of diffusion coefficients (D) from such FRAP measurements will depend on model assumptions[83], in general, D is inversely proportional to τ, thus throughout this study we use ($1/\tau$ as a surrogate measure of coupling and indirectly of electrical diffusion, D_v.

3.5.2 Rate-dependent evolution of fine-scale Ca^{2+} alternans as a function of coupling

Another work we did was to quantify the spatiotemporal behavior of intracellular Ca^{2+} alternans in our experimental system under the established coupling conditions. Experimental tracking of early (cellular) "seeds" of Ca^{2+} alternation, that we call "fine-scale" alternans, is difficult at the macroscopic/tissue level because of their small amplitude and fine spatial scale, i.e. because of their apparent similarities with random noise[99]. To achieve this by non-confocal imaging over a centimeter scale FOV, we combined ultra-high resolution optical mapping[100] and a newly validated algorithm for detection of spatiotemporal alternans, which uses temporal persistence (TP) as a measure to ensure high fidelity in distinguishing low-level alternation from noise[99]. Fig 17A shows the first to our knowledge example of a non-confocal detection of cellular-level Ca^{2+} alternans while mapping a cm-FOV. Five fine-scale spatially-discordant alternans regions are shown, which persisted for at least 50 beats when this sample was paced at 4Hz.

For the chosen algorithm parameters (TP≥60%)[99], each spot of alternation in Fig 18B-D is confirmed with specificity >99.99% and sensitivity >96.75% for alternans ratios ≥5%, even if the patterns visually may resemble noise. Such fine alternating signals are lost in classic macroscopic maps of Ca^{2+} alternans due to spatial averaging by insufficient resolution. Here, we reveal that "seeds" of alternation exist at relatively low pacing frequencies regardless of coupling, and that increasing pacing rates gradually recruit larger areas of Ca^{2+} alternation until development of large-scale alternans and/or direct development of conduction blocks. These results are in agreement with confocal data from intact hearts [77].

Fig 18A-B links measured coupling values (1/ τ to quantified macroscopic tissue function, to reveal theoretically expected monotonic increase of CV and break-point frequency (the maximum frequency of 1:1 capture) with coupling. Figs 18C-F illustrate the behavior of intracellular Ca^{2+} alternans as function of coupling. The progressive recruitment of larger areas of fine alternans is shown across pacing frequencies for three levels of coupling, Fig 18C. Increase of coupling resulted in monotonic decrease in the average amplitude of early alternation (alternans ratio) at low frequencies (< 2Hz), Fig 18D. Surprisingly, the area of early Ca^{2+} alternation was found to be a non-monotonic function of coupling, Fig 18B and Fig 18E, where intermediate (not low) coupling resulted in the largest area of early alternation. Furthermore, this trend was reproduced when we examined the percent of samples in each of the four experimental groups that underwent large-scale Ca^{2+} alternation prior to block (large-scale alternans were defined as alternans in contiguous areas ≥ 0.3mmx0.3mm), Fig 18F. Thus, the spatial extent of early Ca^{2+} alternans (ignoring amplitude) was predictive of alternans development at higher rates for different coupling.

3.5.3 Antiarrhythmic effects of 4PB

Fig. 17 shows examples of alternans development in linear strips of cardiomyocytes (4PB-treated, heptanol and control) with progressively increasing pacing frequencies, in which control and heptanol samples exhibited more alternans, at earlier time points (lower frequencies) and developed conduction blocks (white) much earlier than 4PB-treated samples.

We further examined the common characteristics of evolution of spatiotemporal alternans or direct transition to conduction blocks when control and 4PB samples were subjected to progressively faster pacing rates. As shown in Fig. 18B, the block frequencies for 4PB treated sample are higher than those in control samples. And usually there are two pathways for alternans evolution: direct transition to conduction blocks or occurrence of alternans. The data shows that most of 4PB-treated samples would directly go to block without exhibiting any alternans, while half of the control samples developed certain alternans before blocking.

In addition to well-known larger scale alternans, using our newly developed algorithm we are able to capture and quantify fine spatial alternans over a large area. These are defined as having small magnitude (<20% of calcium transient height, measured as difference in peak height between consecutive beats) and small cellular/subcellular level spatial scale (typically around 200μm). Figure 18C indicates that 4PB can effectively suppress the emergence of fine alternans, most likely via coupling promoted synchronization.

3.5.4 Predicting arrhythmia development depends on profiles of early stage alternans

In order to investigate the evolution pathways, different aspects of detected spatiotemporal profiles of alternans must be characterized, e.g. spatial percentage (the area of alternans/SDA regions compared to the whole sample area), number of regions (the amount of alternans/SDA regions), and their corresponding ratios between two phases. The variation of

these parameters over different pacing frequencies will capture the temporal Ca^{2+} alternans evolution.

Cardiac monolayers will be stimulated according to the pacing protocol in Fig.4 panel B. In all our experimental data (25/25 samples) we have observed fine-scale alternans at early stages (pacing frequency≤2Hz). Although these fine-scale alternans only occupy 1% or even less of the total area, as shown in Fig.17 panel B, they would grow with increasing pacing frequency. Panel C shows two aspects of evolution: parameters class I (number and size): with higher pacing frequency, alternans regions will consolidate to larger areas, or more regions will emerge but with similar size. parameters class II (location): after pacing frequency is increased, alternans regions will drift to other locations, but in some samples, they may be anchored to the same locations. Intuitively, spatial percentage and number of regions are two parameters to quantify the spatiotemporal evolution profiles of alternans, which could be used for class I parameters. But the tools for quantifying class II are still missing. And the problem becomes even more complicated when we consider phase information provided by our detection algorithm.

The main purpose of the proposed research is not only to characterize the spatiotemporal profiles of alternans, but also to deliver predictive tools for later arrhythmia development based on the characteristics of early stage alternans. Clinically, the onset of VT/VF occurs when alternans occupy sufficiently large area. Based on the spatiotemporal profiles of early stage alternans, we are trying to answer the questions: what's the size of alternans areas, what's the spatial morphology of these alternans regions, and when it will happen?

Panel A in Fig.19 shows that the average area of pre-threshold (early stage, pacing frequency≤2Hz) alterans is proportional to the average maximum area of alternans, i.e. the area of pre-threshold alternans regions is predictive of the alternans areas later on. Using K-means

clustering analysis [101] in the example in Fig.19, we show successful prediction of the nodal line location of later (full-blown) SDA regions. This approach will be employed and validated as a predictive tool. How to predict when (at what rates) the largest alternans area will occur is still unclear. Intuitively it will be related to the block frequency, as shown in panel B of Fig.4, but we will need further quantification.

3.6 Conclusions

Recent evidence from modeling and experiments casts intracellular Ca^{2+} dynamics as independent pro-arrhythmic factor. However, the detailed mechanism of instabilities progression to arrhythmias at the tissue level is not well understood. Cellular coupling through gap junctions provides low-resistance pathways between cardiac myocytes and hence helps synchrony. We hypothesize that cellular coupling alters the early spatiotemporal evolution of Ca^{2+} instabilities and can be quantitatively linked to arrhythmic events. We experimentally perturbed cellular coupling bi-directionally (increasing and decreasing) by use of a small molecule, 4-phenylbutyrate (4PB), which we have shown to serve as gap junction agonist, increasing diffusion and conduction velocity (CV) without major side effects, and the use of a gap junction uncoupler – heptanol. Coupling under these conditions was quantified by macroscopic fluorescence recovery after photobleaching (gap-FRAP). Calcium waves were captured by ultra-high resolution optical mapping (allowing subcellular imaging over cm-scale) in conjunction with a recently published algorithm for spatiotemporal detection of subtle fine-scale alternans. Experimental results did show the expected increase of CV and breakpoint frequency with coupling. However, tracking the evolution of Ca^{2+} alternans with pacing frequency reveals a non-monotonic dependence of early (<2Hz) alternans area with coupling, as intermediate (not low) coupling results in largest alternating area. This relationship is closely matched by the % of

samples exhibiting large-scale alternans as function of coupling. We conclude that although reduced coupling may lead to paradoxically less Ca^{2+} alternans overall, a better coupling renders anti-arrhythmic benefits by increasing CV and the frequency at which alternans occur. Furthermore, our data indicate that early subtle alternans characteristics may be predictive of later arrhythmia events.

Fig.10 Experimental setup for optical mapping. Neonatal rat cardiomyocytes were cultured on thin long silicone polymer (PDMS) grooves to form confluent monolayers. Pacing was applied via a platinum line electrode on one of the sides of each sample. Optical mapping of intracellular calcium was performed at ultrahigh-resolution using an intensified CMOS camera

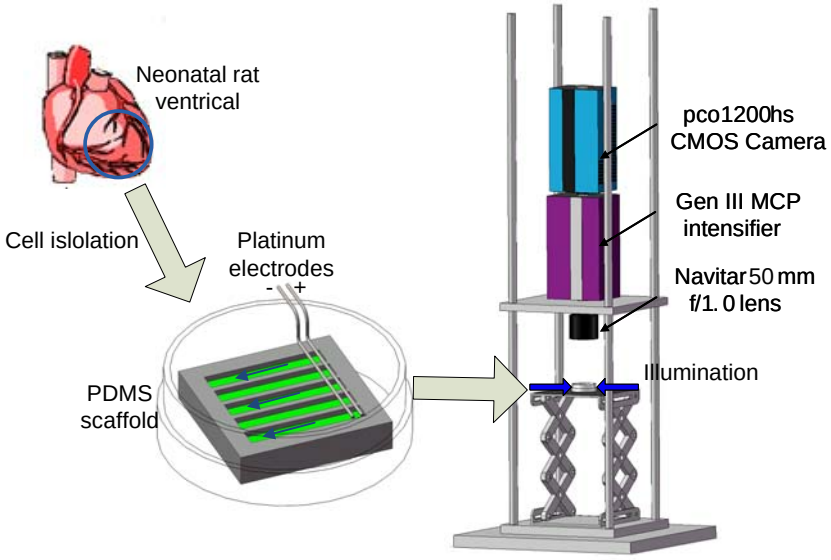

Fig.11 Experimental protocol for evaluating photobleaching. Sample was paced at 1.5Hz for 60 beats without illumination or data acquisition, then illumination light was turned on and 15 beats were recorded. This process was repeated 17 times. The SNR decreased only slightly (11.5%), from 26.45 to 23.40 within the 15 minutes of the experiment.

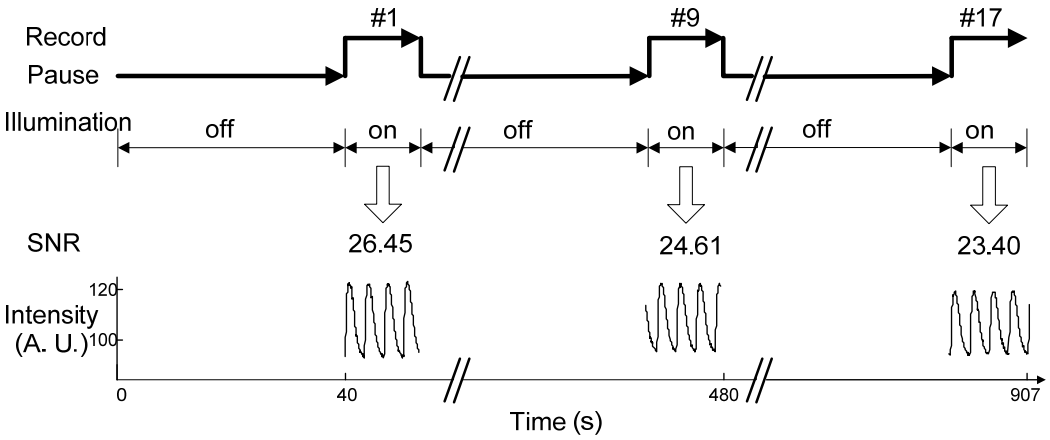

Figure 12. Experimental evidence for strong positive V_m-Ca^{2+} coupling and electromechanical concordance. Panel A: Representative traces of voltage and Ca^{2+} from the same sample at different frequencies during 1:1 response, alternans (2:2) and blocks (2:1). Scale bar is 1s. Panel B: Quantitative analysis of memory (hysteresis) in the induction and disappearance of V_m and Ca^{2+} alternans (n = 16). Samples were paced progressively towards higher frequencies until appearance of alternans (fa) and then back towards slower rates to determine the frequency of disappearance (fd), see bottom inset. Hysteresis was quantified as (fa – fd). Data for all 16 samples are shown as a scatter plot, and as a bar graph (top inset) with mean±S.D.

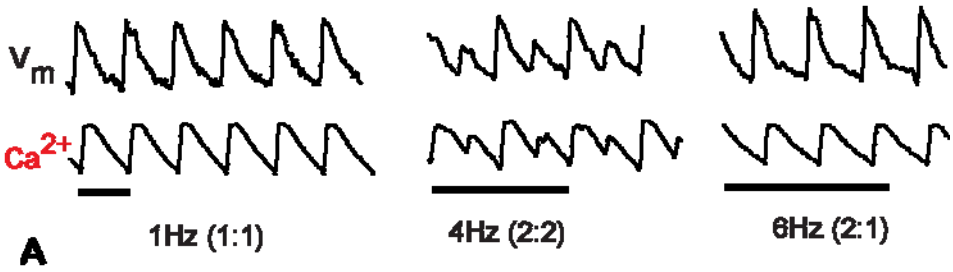
Vm
Ca2+
1Hz (1:1)
4Hz (2:2)
6Hz (2:1)

A

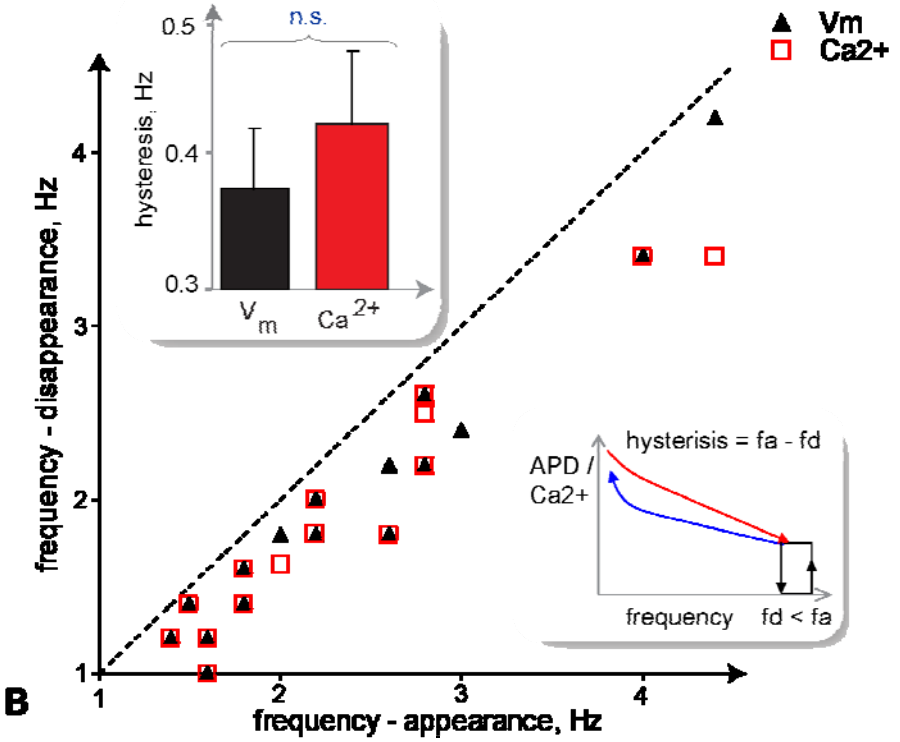
Vm
Ca2+
n.s.
0.5
0.4
0.3
hysteresis, Hz
Vm
Ca2+
hysterisis = fa - fd
APD /
Ca2+
frequency
fd < fa
frequency - disappearance, Hz
frequency - appearance, Hz
1
2
3
4

B

Fig.13 4PB promotes the expression of connexin 43. Panel A: Representative confocal immunofluorescence images of both control and 4PB treated samples. Blue indicates nuclei stained by DAPI. And green is the Cx43 marked by immunofluorescence. Panel B: Granulometry-quantified region numbers of Cx43. Panel C: Western blot results of 4 typical control and 4PB treated samples.

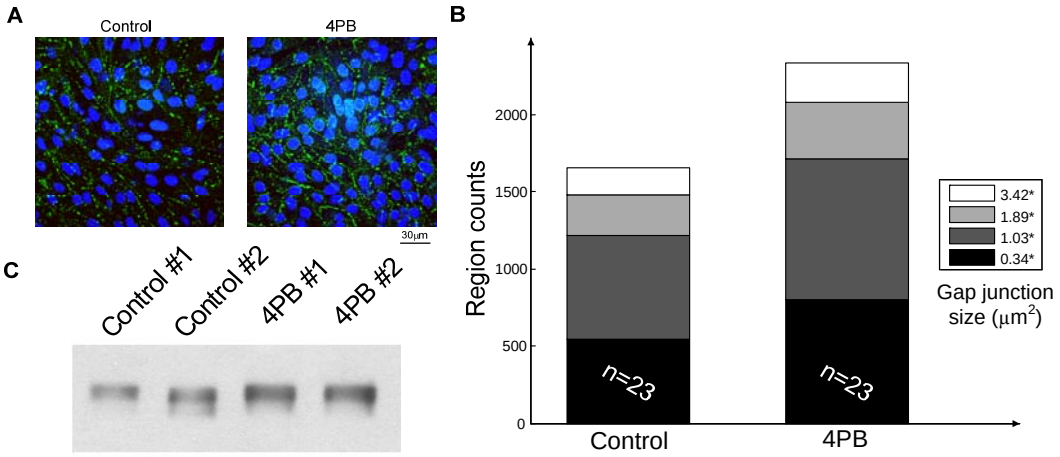

Figure.14 Viability assessment of 4PB. Panel A: representative images stained by Calcein (green, live cells), and Ethidium (red, dead cells). Panel B: Viability results of control, 1mM and 10mM 4PB treated samples.

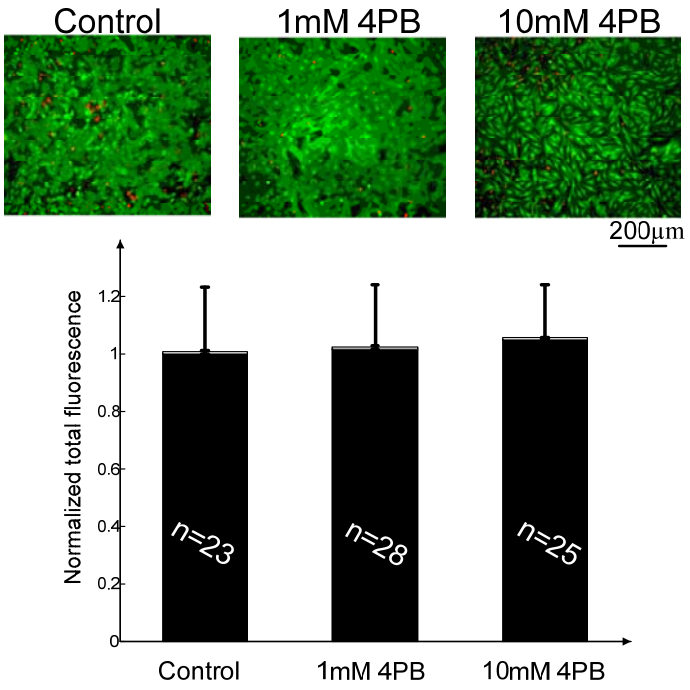

Figure.15 FRAP experiments to assess level of intercellular coupling (diffusion) after perturbation. The effects of gap junction agonist (4PB) and gap junction antagonist (heptanol) on cellular connectivity were quantified by FRAP. (A) Representative fluorescence images at different time points during the FRAP: before bleaching, at t = 0 s and at t = 20 s. Bleached cells are indicated by yellow arrows. Inset shows the applied FRAP protocol. (B) Averaged perturbation-relaxation recovery curves of 4PB (red), control (blue), and 0.25 mM heptanol-treated samples. Error bars are 95% confidence interval. (C) The time constant calculated from the recovery curve fitting for 4PB, control, and heptanol samples. Samples treated with 4PB and 0.5 mM heptanol have significantly different time constants compared to control samples. Error bars are 95% confidence interval; number of examined samples is shown for each group. Diffusion is inversely proportional to the calculated time constants.

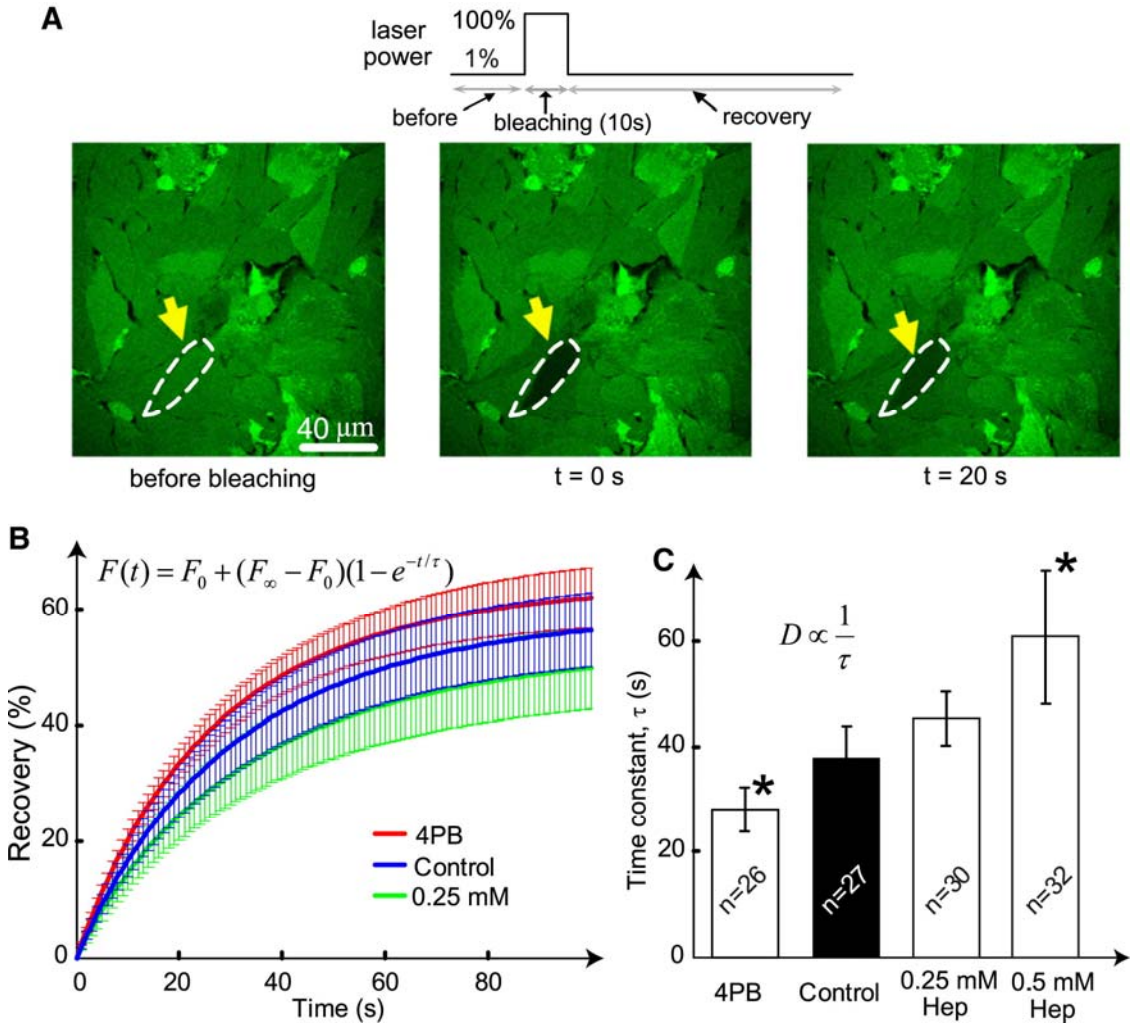
A
laser power
100%
1%
before
bleaching (10s)
recovery
40 µm
before bleaching
t = 0 s
t = 20 s
B
$F(t) = F_0 + (F_\infty - F_0)(1 - e^{-t/\tau})$
Recovery (%)
Time (s)
4PB
Control
0.25 mM
C
$D \propto \frac{1}{\tau}$
Time constant, τ (s)
n=26
n=27
n=30
n=32
4PB
Control
0.25 mM Hep
0.5 mM Hep

Figure.16 Effects of coupling on propagation. (A) CV measured at 30°C, 1 Hz pacing for each group in the rectangular samples; last bar shows recovery (wash out) after heptanol treatment. Error bars indicate standard deviation; (∗) significance at $p < 0.05$; the 95% CI for the slope of a regression line was (23.7, 46.9). (B) Example activation maps for the four groups; color indicates time of activation (0 to 0.1 s), isochrones (in black) are 0.02 s apart. Ca2+ transients are shown from each sample at the ∗ location. (C) Estimated relative effects of heptanol on CV via suppression of gNa and via gap junction block. The two diamonds indicate actual measured CV values (as % of control, from panel A) for the two heptanol concentrations used here; the three curves show expected reduction in CV via gNa block alone: analytical estimate (black), numerical solution (red), and our experimental data with TTX block (blue). See text and Fig. S1 for further details. (D and E) No significant effects of 4PB and low doses of heptanol on Ca2+ transients: CTD80 and rise time (mean ± SE) are not significantly different between the groups ($p = 0.34$ for 4PB effects and $p = 0.16$ for heptanol effects on CTD80); power analysis with bootstrapping would have uncovered significant changes if CTD80 were altered by >18.7%. Panel F: Relative effects of heptanol on CV via suppression of Na+

channels and suppression of gap junctions. Shown are two experimental dose-response curves. Left: Sigmoid curve fit to experimental data from Nelson & Makieski in dog Purkinjie cells on the effects of heptanol on Na+ channel availability. Indicated is k0.5 = 1.3mM, along with the low concentrations used in our study and the respective gNa levels based on this dose-response curve. Right: Sigmoid curve fit to experimental data from Brette & Orchard in adult rat cardiomyocytes on the effects of TTX on Na+ channel availability. Indicated is k0.5 = 0.75 μM, along with 4 TTX concentrations (red diamonds) used in our study to perturb gNa levels and measure CV. These data were used implicitly in Panel C.

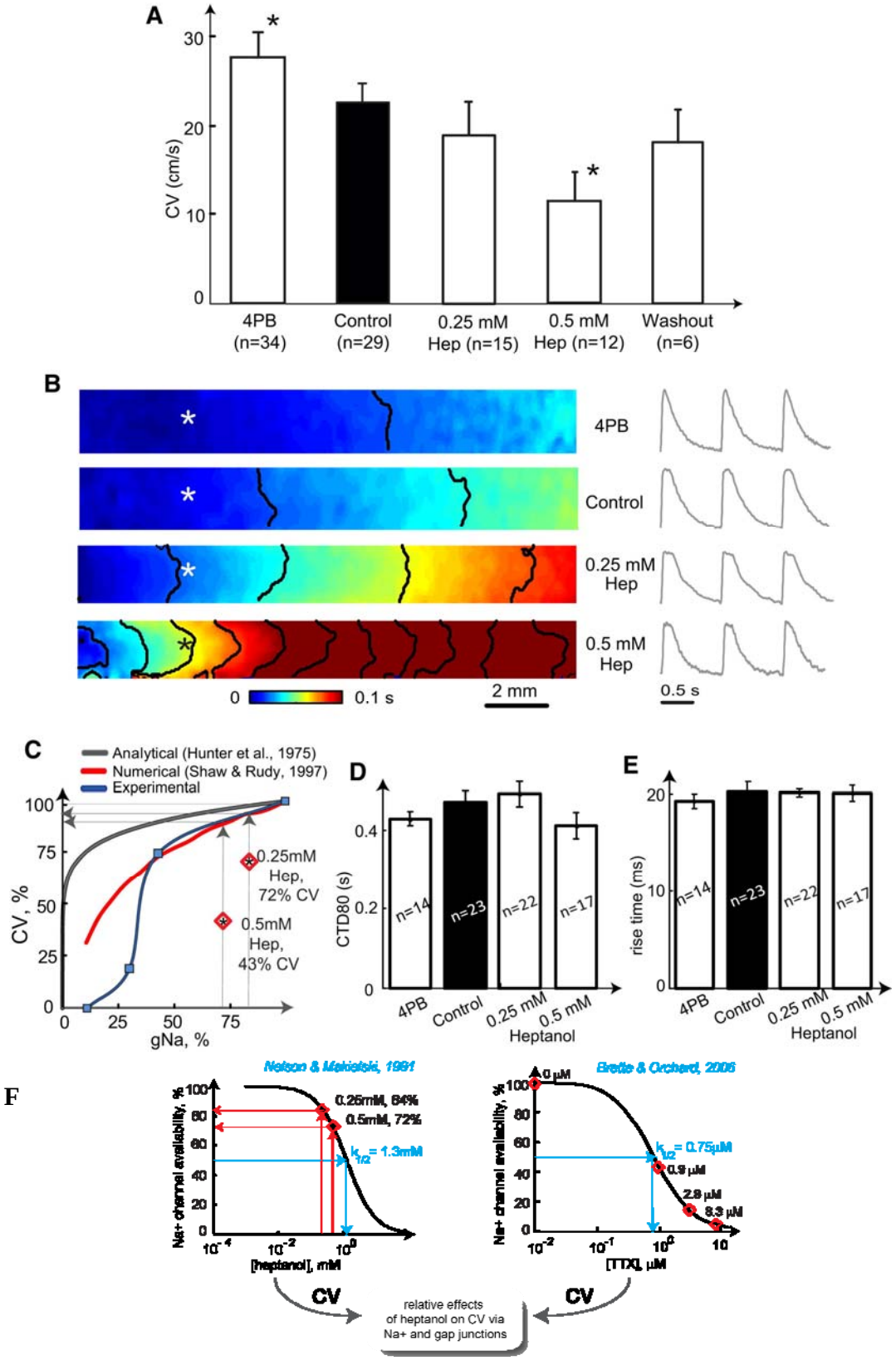
A
CV (cm/s)
4PB (n=34)
Control (n=29)
0.25 mM Hep (n=15)
0.5 mM Hep (n=12)
Washout (n=6)
B
4PB
Control
0.25 mM Hep
0.5 mM Hep
0.1 s
2 mm
0.5 s
C
Analytical (Hunter et al., 1975)
Numerical (Shaw & Rudy, 1997)
Experimental
0.25mM Hep, 72% CV
0.5mM Hep, 43% CV
CV, %
gNa, %
D
CTD80 (s)
n=14
n=23
n=22
n=17
Heptanol
E
rise time (ms)
F
Nelson & Makielski, 1991
Ereifo & Orchard, 2006
0.25mM, 84%
0.5mM, 72%
Na+ channel availability, %
[heptanol], mM
[TTX], µM
relative effects of heptanol on CV via Na+ and gap junctions
CV

Figure.17 Rate-dependent evolution of fine-scale Ca^{2+} alternans. (*A*) Resolving fine-scale alternans while imaging a large FOV: (*top*) space-time plot of persistent (over 55 beats) fine-scale alternation at the cellular level at 4 Hz pacing, detected while imaging FOV = 2.2 × 2.2 cm^2; color indicates Ca^{2+} AR (%), multiplied by representative phase, (−1, +1); (*bottom*) plot of fine-scale spatially discordant alternans along a line from the same sample. (*B–D*) Representative spatial maps of fine-scale Ca^{2+} alternans at steady state under different pacing frequencies and cellular coupling conditions: 0.5 mM heptanol (*B*), control (*C*), and 4PB samples (*D*). Pacing electrode is on the right side. Color indicates AR (%) at different spatial locations. Red and blue identify opposite phase; dark green areas are regions with no detected alternans; white areas identify conduction blocks. Traces on the right are from the location identified by a (*) at pacing frequencies 2.8, 3.4, and 4.0 Hz.

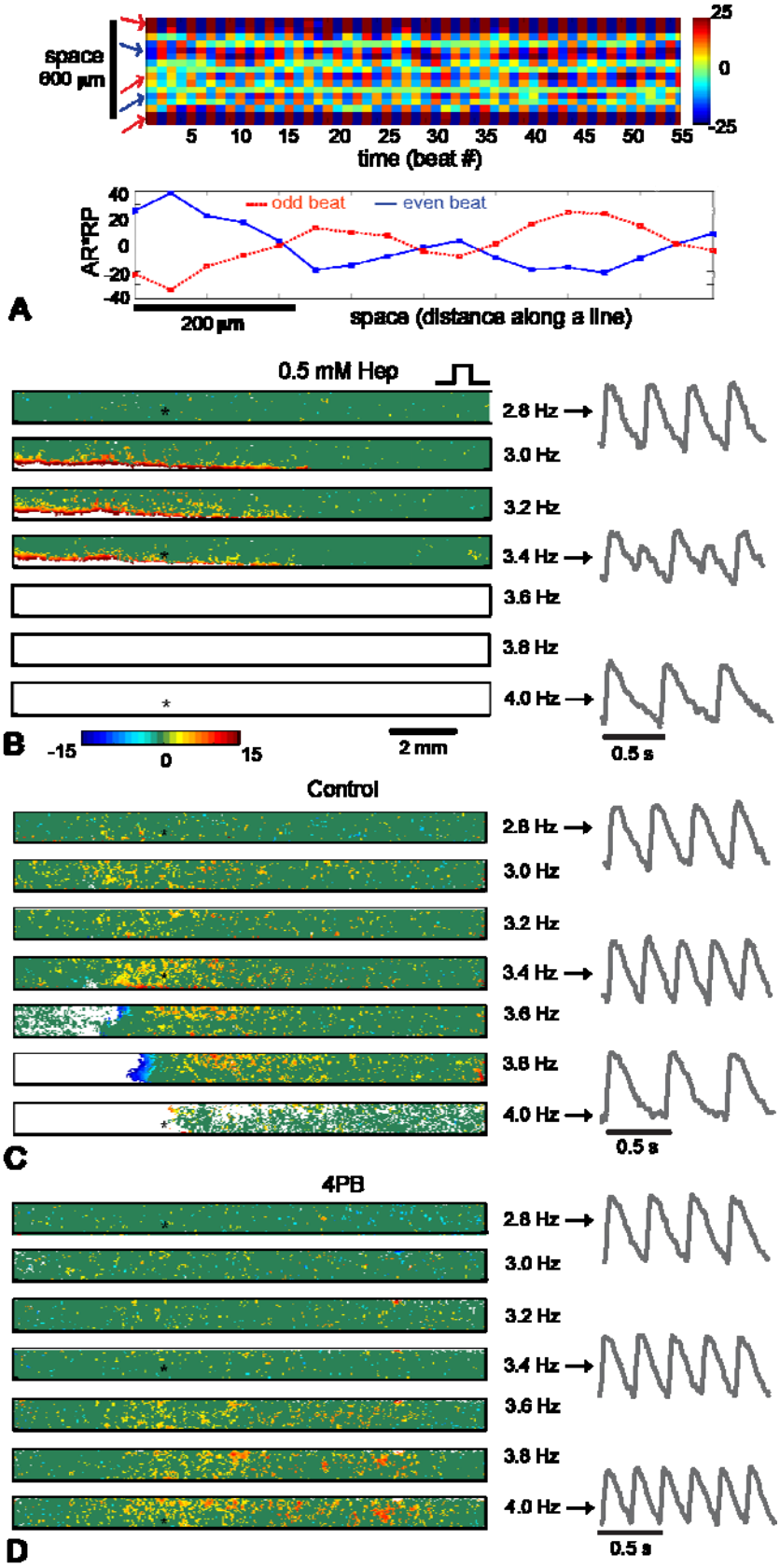
space
600 μm
25
0
-25
5 10 15 20 25 30 35 40 45 50 55
time (beat #)
odd beat
even beat
AR*RP
40
20
0
-20
-40
200 μm
space (distance along a line)
A
0.5 mM Hep
2.8 Hz
3.0 Hz
3.2 Hz
3.4 Hz
3.6 Hz
3.8 Hz
4.0 Hz
B
-15
0
15
2 mm
0.5 s
Control
C
4PB
D

Figure.18 Linking dynamic properties of Ca2+ alternans to FRAP-quantified diffusion. (*A*) CV as a function of the FRAP-measured diffusion factor ($1/\tau$, 1/s) for the four experimental groups. (*B*) Breakpoint frequency (frequency of failure to follow 1:1) as a function of the diffusion factor ($1/\tau$, s). (*C*) Evolution of the areas exhibiting local Ca^{2+} alternans as a function of pacing frequency: green for low coupling (0.5 mM heptanol), black for intermediate coupling (*control*), and blue for high coupling (4PB); arrows indicate the average breakpoint frequency; error bars indicate standard error. (*D*) Space-averaged AR for early fine Ca^{2+} alternans (<2 Hz) as a function of coupling/diffusion. (*E*) Area of fine Ca^{2+} alternation at low frequencies (<2 Hz) as a function of coupling. (*F*) Proportion of samples (%) that exhibited large-scale 2:2 alternans upon breakpoint frequency (the remaining samples went directly into 2:1 block). Sample numbers for *A*~*F* are $n_{0.5\ mM} = 17$, $n_{0.25\ mM} = 14$, $n_{control} = 28$, $n_{4PB} = 18$; data are mean ± 95% confidence interval.

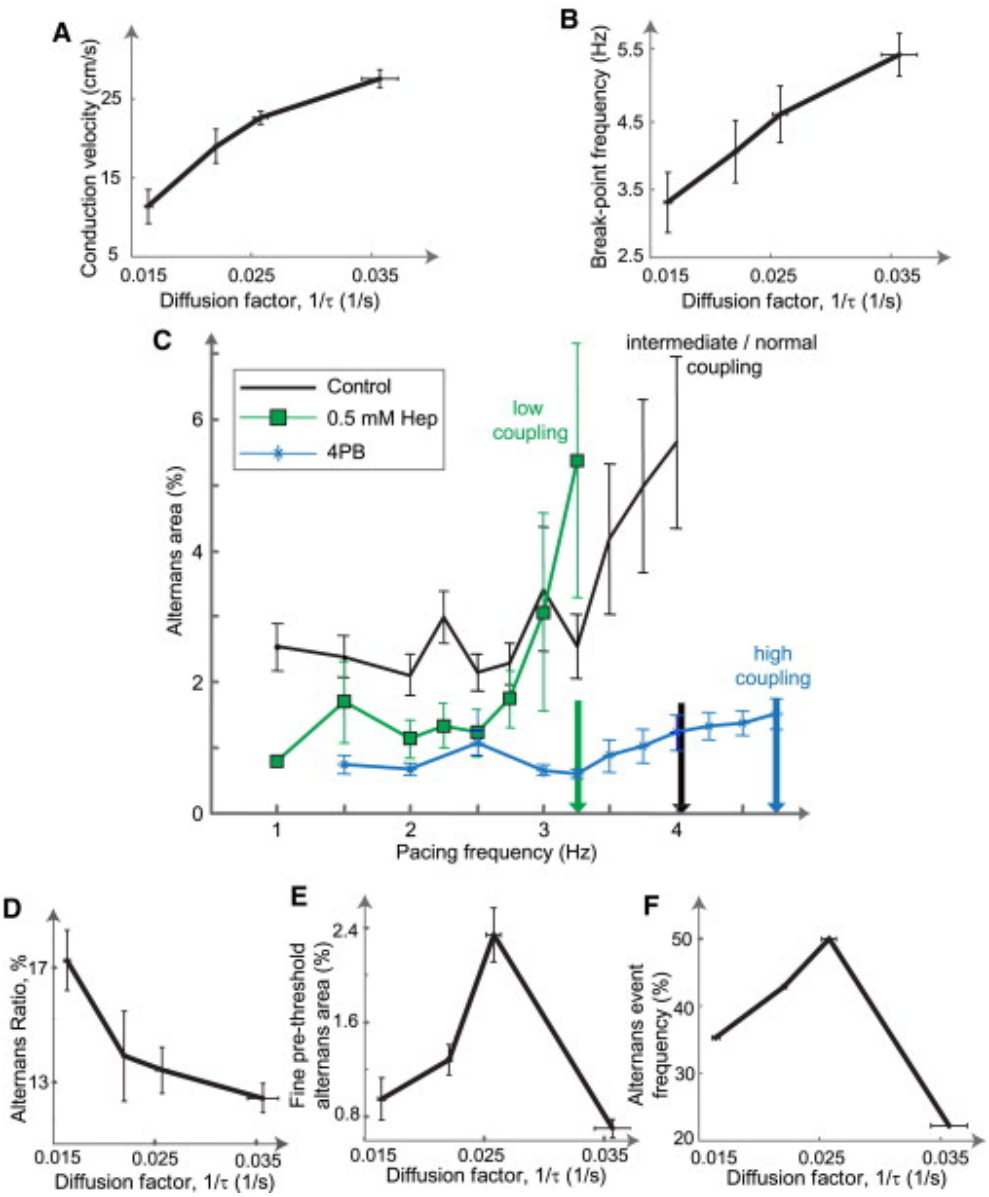
A
Conduction velocity (cm/s)
25
15
5
0.015
0.025
0.035
Diffusion factor, 1/τ (1/s)
B
Break-point frequency (Hz)
5.5
4.5
3.5
2.5
0.015
0.025
0.035
Diffusion factor, 1/τ (1/s)
C
Control
0.5 mM Hep
4PB
intermediate / normal coupling
low coupling
high coupling
Alternans area (%)
6
4
2
0
1
2
3
4
Pacing frequency (Hz)
D
Alternans Ratio, %
17
13
0.015
0.025
0.035
Diffusion factor, 1/τ (1/s)
E
Fine pre-threshold alternans area (%)
2.4
1.6
0.8
0.015
0.025
0.035
Diffusion factor, 1/τ (1/s)
F
Alternans event frequency (%)
50
40
30
20
0.015
0.025
0.035
Diffusion factor, 1/τ (1/s)

Fig.19 Three characteristics that could predict later arrhythmia development. A. cellular coupling is linearly related to break-point frequency. **B.** The area of early fine Ca^{2+} alternans (<2Hz pacing) correlates significantly with the maximum alternans area upon break-point frequency. **C.** Kmeans cluster analysis applied to fine Ca2+ alternans at 2Hz pacing considering their phases successfully predicts the nodal line position developed at 4Hz pacing in the same sample.

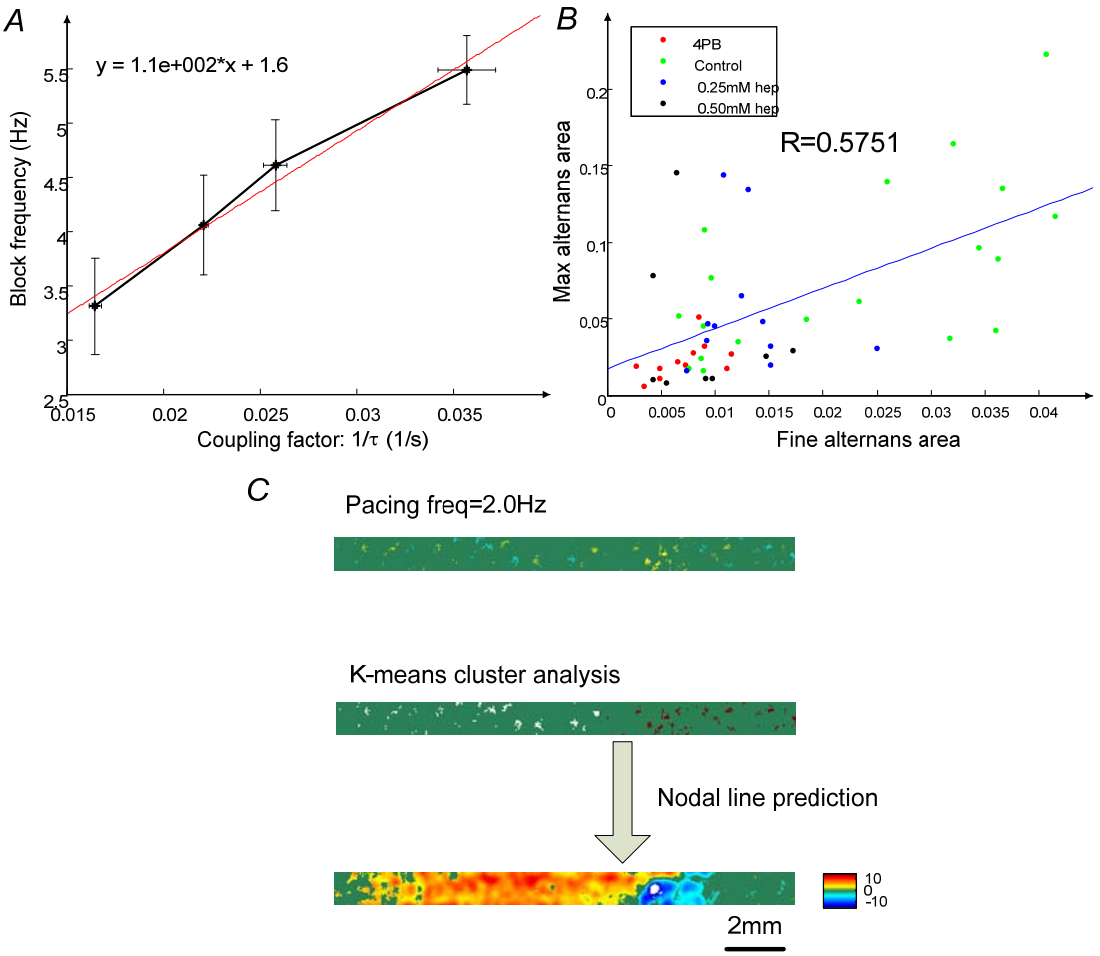

Chapter 4

COMPUTER SIMULATIONS OF Ca^{2+} ALTERNANS AND VARIABLE DIFFUSION IN A CARDIAC MODEL

4.1 Abstract

Thanks to the alternans detection algorithm and ultra-high spatiotemporal resolution macroscopic imaging system, we have experimentally discovered the non-monotonic relationship between alternans and intercellular coupling, and the existence of fine scale alternans. In order to further confirm the discovery, we firstly used classic diffusion equation to verify the monotonic relationship by assuming that alternans spreading is a simple diffusion phenomenon, and then used a more comprehensive computational cardiac model to simulate the monotonic relationship. Both simulations corroborated the experimental findings and offered mechanistic insight of the origin and development of cardiac arrhythmias.

This chapter is based on published work [102]. And thanks to Dr. Yohannes Shiferaw for helping with the cardiac simulations.

4.2 Introduction

Although experimental results from different coupling conditions have disclosed a lot of insights about intracellular Ca^{2+} alternans evolution, and one of the most interesting discoveries is the counterintuitive non-monotonic relationship between the occurrence of alternans and intercellular coupling conditions: there are more alternans in normal coupling conditions than that in low or high coupling conditions. So far, no theory can explain the experiment results, it's obligatory to further validate the experiment results and explore the mechanistic explanation.

Additionally, the coupling experimental results are limited by many factors. For instance, the range for diffusion coefficient is only from 0.015 to 0.035, with $ratio_{max/min} \approx 2$, while the $ratio_{max/min}$ in computer could be infinite theoretically. Also sample numbers are limited by budget and time. The simulation results will be able to validate and greatly expand the experimental results.

Besides traditional diffusion equation, we are looking for a more comprehensive model for cardiac simulations. Fox's dog action potential model is a good candidate[103], which is derived from Luo-Rudy model[104]. Comparing with other models, the advantage of the Fox model is that it's able to reproduce action potential and intracellular Ca^{2+} handling in both normal and failing canine ventricular myocytes using biophysically detailed descriptions of both sarcolemmal currents and key components of E-C coupling [103].

Finally, In collaboration with Prof. Yohannes Shiferaw at the California State University, Northrige, we have decided to use Shiferaw-fox model, which is a simplified mathematical model of the L-type Ca^{2+} current and incorporated it into an established ionic Fox AP model [105] of the membrane voltage dynamics, modified to include the Ca^{2+} cycling model of Shiferaw et al.[106], and this model more realistically represents Ca^{2+} cycling dynamics.

4.3 Methods

4.3.1 Model simulations of diffusion using the classic diffusion equation

We first considered the classic diffusion equation for homogeneous isotropic two-dimensional medium:

$$\frac{\partial C}{\partial t} = D\left(\frac{\partial^2 C}{\partial x^2} + \frac{\partial^2 C}{\partial y^2}\right) \tag{6}$$

For initial conditions, where the local change in concentration is described by the Dirac function, the analytical solution is given by Crank[107] as follows:

$$C(r,t) = \frac{Co}{\left(2\sqrt{\pi Dt}\right)^n}\exp\left(-\frac{r^2}{4Dt}\right) \tag{7}$$

Parameters include distance, r, from the origin, time, t; factor n=2 for two-dimensional isotropic medium; $C_o = 1$ (concentration per area) is the initial concentration at r = 0, t = 0. The diffusion constant, D, was varied between 0.5 and 4.5 (area per time). An arbitrary concentration threshold of 0.0049 was imposed to illustrate the behavior of the model.

4.3.2 Computer simulations of Ca^{2+} alternans and variable diffusion in a cardiac model

We also modeled voltage and calcium dynamics in a two dimensional tissue using the reaction-diffusion equation:

$$\frac{\partial V}{\partial t} = -\frac{I_{ion}}{C_m} + D\left(\frac{\partial^2 V}{\partial x^2} + \frac{\partial^2 V}{\partial y^2}\right), \tag{8}$$

where C_m = 1 F/cm2 is the membrane capacitance, D is the effective diffusion coefficient of membrane voltage in cardiac tissue, and where I_{ion} is the total ionic current density. The reaction-diffusion equation was integrated with an operator splitting method, and adaptive time step method [108]. The space step was 0.015 cm and the time step varied from 0.1 to 0.01 ms. The ionic current was modeled by integrating a model of Ca^{2+} cycling of Shiferaw et al.[109], with the canine action potential model of Fox et al.[110]. Cellular alternans can be generated in this model either by a dynamical instability of Vm or by Ca^{2+} dynamics. In our simulations model parameters were adjusted so that alternans were due to an instability in Ca^{2+} cycling dynamics via a steep release load relationship (see [111] for details). We modeled the case of electromechanically concordant alternans, in which a long APD is associated with a large Ca^{2+} transient, since this "positive coupling" scenario [111] agrees with the experimentally observed relationship between the Ca^{2+} transient and the APD in our neonatal rat culture. The strength of the electromechanical (V_m-Ca^{2+}) coupling in the model was controlled by the time scale of recovery for L-type Ca2+ channel, where a very fast kinetics makes it insensitive to the previous diastolic interval and abolishes voltage-driven APD alternans and its feedbacks on Ca^{2+} alternans.

In order to model the spatial evolution of alternans amplitude in tissue we considered a strip of cardiac tissue 150 cells long and 3 cells wide. Heterogeneous Ca^{2+} cycling properties were

incorporated by adjusting cell model parameters in center region (20 by 3), in the center of the tissue, so that cells in this region were unstable to Ca^{2+} alternans at a pacing rate of 250ms, while cells outside this region were stable i.e. they did not display alternans when uncoupled from the tissue and paced at 4Hz. We then paced the tissue for 70 beats until steady state was reached, similar to the experiments. Spatial profiles of Ca^{2+} and APD alternans amplitude were then measured and plotted. This simulation was repeated with different values of the voltage diffusion coefficient in the range: $Dv=0.24\sim1.8*10^{-3}$ cm^2/ms.

4.3.3 Computer simulations of Ca^{2+} alternans and variable diffusion using amplitude equations

In a more general way, the effect of voltage diffusion on the spatial distribution of Ca^{2+} alternans can be studied by deriving equations that govern the amplitudes of Ca^{2+} and APD alternans, i.e. amplitude equations. This approach is applicable close to the period doubling bifurcation where the amplitudes of alternans are small and evolve slowly over many beats, and thus relevant to the case of early, fine-scale alternans examined here. We assume a one dimensional cable where each cell is paced simultaneously. The amplitude of APD and Ca^{2+} alternans at position x and time t are denoted as $a(x,t)$ and $c(x,t)$ respectively. The spatiotemporal evolution of small-amplitude alternans is then governed by a coupled system of partial differential equations:

$$\partial a/\partial t = \alpha\, a + \beta c - \Gamma_a a^3 + \xi_v\, (\partial^2 a/\partial x^2) \qquad (9)$$

$$\partial c/\partial t = \gamma\, a + \delta c - \Gamma_c c^3 + \xi_c\, (\partial^2 c/\partial x^2) \qquad (10)$$

The variables are described below:

i. The variables ξ_v and ξ_c represent the diffusive spread during a single paced beat of voltage and Ca^{2+}, respectively. In the amplitude equation formulation, these quantities are related to the diffusion coefficients of voltage and Ca^{2+}according to $\xi_v = \text{sqrt}(D_v T)$ and $\xi_v = \text{sqrt}(D_v T)$, where T is the pacing period and D_v and D_c are the diffusion coefficients of voltage and Ca^{2+}, respectively. Note that in cardiac tissue $\xi_v/\xi_c \gg 1$ since voltage diffuses much faster than Ca^{2+}. In this study, we fix $T = 1$.

ii. The variable α denotes the growth rate of APD alternans. If $\alpha > 0$, then APD restitution is steep and the APD will alternate ($\alpha > 0$) independently of Ca^{2+}. Here, we will assume that voltage is stable ($\alpha < 0$) and that Ca^{2+} cycling is the underlying nonlinearity for alternans. This assumption is justified by our observation of fine-scale alternans, as discussed in the main text.

iii. The variable δ denotes the growth rate of the Ca^{2+} cycling instability; $\delta > 0$ in this study to reflect that alternans are due to Ca^{2+} cycling.

iv. The parameters γ and β denote the coupling between APD alternans on Ca^{2+} alternans amplitude, and vice versa. Here we assume positive coupling (positive values for γ and β) based on observed electromechanical concordance in our system.

v. The variables Γ_a and Γ_c are constant parameters to ensure that alternans amplitudes stabilize at a finite value.

Using the system of equations above, we confirm our numerical findings with the full ionic model that an increase in ξ_v leads to a decrease in Ca^{2+} alternans amplitude, and that the area of tissue with Ca^{2+} alternans above a threshold value has a non-monotonic dependence on ξ_v. We considered a cable of $N = 1000$ cells where the central 30 cells were unstable to Ca^{2+}. The parameters used in the model are: $\alpha = -0.1$, $\beta = 0.1$, $\gamma = 0.1$, $\Gamma_c = 0.01$, $\Gamma_v = 0$, $\xi_c = 0.5$. Ca^{2+}

alternans is made unstable by setting $\delta = 0.01$ for the middle 30 cells, and $\delta = -0.1$ for the rest of the tissue. A threshold for the alternans amplitude is set at 1.2 to quantify the area.

4.4 Results

4.4.1 Simulation results from classic diffusion equation verified effects of coupling on the spatial properties of Ca^{2+} alternans

Considering the non-trivial nature of the experimental results in Fig 18, we sought insight by theoretical modeling. Simply abstracting the behavior of Ca^{2+} alternans and coupling to a generic passively diffusing parameter using the analytical solution to the classic diffusion equation in a homogeneous medium[107], revealed that the asymmetric non-monotonic relationship in Fig 18 can be reproduced by combining diffusive spread with a threshold of detection. When alternans are treated as binary events, i.e. the information about the alternans ratio (above a threshold of detection) is ignored; the affected areas exhibit such non-monotonic behavior. But this approach of treating the diffusion of Ca^{2+} alternans is overly simplistic and does not capture the mechanism of events in a complex reaction-diffusion system, such as the heart.

In Fig. 20. Panel A: Using an analytical solution of the generic diffusion equation for two-dimensional medium and a Dirac function of concentration change as initial condition, we obtain the spatial profiles at a fixed time for different degrees of coupling. B: Quantification of spatial patterns (from A) by imposing a threshold (left); average concentration after a fixed time as function of diffusion properties (middle); area of concentration above a threshold as function of diffusion properties (right).

4.4.2 Theoretical explanation of the effects of coupling on the spatial properties of Ca^{2+} alternans

To model the more complex case of Ca^{2+} alternans in cardiac tissue, we applied an existing ionic model of voltage and calcium in cardiac tissue[111]. Model parameters were adjusted so that

alternans were due to an instability of Ca2+ cycling which induced electromechanically concordant alternans at rapid pacing rates. This choice of parameters is based on our experimental observation that a large/small Ca+ transient corresponds to a long/short APD. Also, we note that alternans in our system cannot be due to a voltage instability, since, as shown previously[112], such a mechanism cannot induce subcellular Ca^{2+} alternans i.e. cell-to-cell coupling requires that voltage driven alternans can only vary on a length scale larger than the electrotonic length. In the modeled spatially-extended cardiac tissue, a central region of Ca^{2+} driven alternans was simulated under variable diffusion conditions. The results, Fig 20A, closely match our experimental findings about the amplitude and area of Ca^{2+} alternation as function of coupling.

Using a computational model of cardiac tissue, an island of Ca^{2+} alternans was simulated under different coupling conditions. Quantification of spatial patterns by imposing a threshold (*A*) average AR under 4 Hz pacing as a function of diffusion properties (*B*); area of Ca^{2+} alternation above a threshold as a function of diffusion properties (*C*). Color (*blue to red*) indicates low to high diffusion. Compare panel B to Fig. 18D, and panel C to Fig. 18, E and *F*. (*D*). Schematic illustration of the effective diffusion of Ca^{2+} alternans via $D_{v:}$ in a cell pair or a cable. (*E*) In the cell/region exhibiting instability (*gray*), Ca^{2+} alternans drive V_m alternans, which propagate according to D_v. In the distant cell/region, V_m alternans cause Ca^{2+} alternans, thus effectively mediating diffusion of Ca^{2+} alternans. (*F*) Effects of V_m-Ca^{2+} coupling on the diffusion of Ca^{2+} alternans: same simulations as in *A*, but under low V_m-Ca^{2+}. Ca^{2+} alternans do not spread outside the unstable region (*E*) because of negligible V_m alternans amplitude and low V_m-Ca^{2+} coupling in this case (*G*).

In Fig. 22, Panel A shows the amplitude of calcium alternans, c_p, as function of the effective diffusion coefficient for voltage, ξ_v. Compare to experimental results in Fig 18D, and model results in Fig 21B and Fig 22A. B. Quantification of the area of local alternation (above a threshold of 1.2) as function of the effective diffusion factor, ξ_v. Compare to experimental results in Fig 18E-F, and model results in Fig 21C and Fig 22B.

4.5 Discussion

Previously, we find that isolated fine-scale (cellular) Ca^{2+} alternans occur at relatively low pacing rates and their amplitude and spatial evolution are modulated by cell-cell coupling in a cardiac syncytium. Our FRAP-quantified perturbations of cellular coupling are likely to affect multicellular diffusion reflected in both D_{ca} and D_v. These two diffusion coefficients differ by 3-5 orders of magnitude: D_v is in the range 0.1-1cm^2/s[113], while D_{Ca} has been measured in the cytoplasm of oocytes as 1.3-6.5x10-4 cm^2/s[114], or estimated for myocytes in the range 0.5 – $5x10^{-5}$ cm^2/s[115, 116]. Because of this disparity, virtually all models of cardiac tissue assume D_{ca}=0 at the tissue level (cell-to-cell), including the model used here.

Considering that in the absence of tissue-level diffusion for Ca^{2+}, our cardiac tissue model qualitatively reproduced the spatial behavior of Ca^{2+} alternans in the experiments, the following mechanism can be put forward for the effects of D_v on Ca^{2+} alternans: At the single cell level, coupling between voltage and Ca^{2+} allows for Ca^{2+} alternans to drive APD alternans (via the action of the Ca^{2+} sensing ion transporters, e.g. L-type Ca^{2+} channel and Na/Ca exchanger) and vice versa – APD alternans can drive Ca^{2+} alternans (via changes in the diastolic interval and thus changes in the amount of Ca^{2+} released). Consider a cell pair or a multicellular cable, where a region (or a cell) is unstable, i.e. exhibits Ca^{2+}-driven alternans, while the rest of the tissue is stable. The spatial profiles for Ca^{2+} and APD alternans are sketched for low (solid lines) and high

(dashed lines) values of D_v. It is important to note that in the unstable cell/region, Ca^{2+} alternans drives APD alternans, while in the stable cell/region APD alternans drives Ca^{2+} alternans. The presence of APD alternans is due to the electrotonic coupling between the unstable region and the rest of the tissue. When coupling (and D_v) is increased, APD alternans will be smoothed out over a longer scale so that APD alternans in the unstable region will decrease while APD alternans in the stable region will increase. Because of the V_m-Ca^{2+} coupling, this will also have smoothing effect on the spatial variation of Ca^{2+} alternans, i.e.: 1) the amplitude of Ca^{2+} alternans will decrease in the unstable region, and increase in the neighboring stable region; and 2) the area of the region exhibiting Ca2+ alternans will increase. Upon further increase in D_v, the amplitude of Ca^{2+} alternans can decrease bellow a threshold of detection.

To further validate this mechanism, we show simulation results with reduced electromechanical (V_m-Ca^{2+}) coupling (Fig. 21F). For the same range of Dv values, due to the now negligible APD alternans outside the unstable region (Fig. 21G) and the very weak effect they have on Ca^{2+} alternans, the latter are completely confined to their origin and the spatial data do not match our experimental findings. These results were also corroborated using amplitude equations linking APD and Ca^{2+} alternans [117, 118] close to the bifurcation point (Fig. 22), strengthening the generality of the proposed mechanism. Fig. 22, A and B, matches well with experimental data in Fig. 18, D–F, and model data in Fig. 21, B and C, and Fig. 20 B. In summary, at the tissue level, the effective diffusion of Ca^{2+} alternans is not a function of D_{ca}, but is indirectly determined by the V_m-Ca^{2+} coupling and by D_v via diffusing APD alternans.

An alternative mechanism for occurrence of fine-scale alternans, driven by voltage, can involve substantial spatial heterogeneities in coupling, as seen during nonuniform heptanol uncoupling in

a trial tissue[119]. However, in our cultured monolayers heptanol effects are expected to be more uniform, and the lower concentrations used here are unlikely to produce complete local uncoupling. These expectations are corroborated by the lack of wavefront fractionation (Fig. 23); as would have been found in nonuniform uncoupling [120].

4.6 Conclusions

Recent experimental and modeling studies demonstrate the fine spatial scale, complex nature and independent contribution of Ca^{2+} dynamics as a pro-arrhythmic factor in the heart. The mechanism of progression of cell-level Ca^{2+} instabilities, known as alternans, to tissue-level arrhythmias is not well understood. As gap junction coupling dictates cardiac syncytial properties, we set out to elucidate its role in the spatiotemporal evolution of Ca^{2+} instabilities. After experimentally perturbed cellular coupling in cardiac syncytium *in vitro*, coupling was quantified by fluorescence recovery after photobleaching, and related to function, including subtle fine-scale Ca^{2+} alternans, captured by optical mapping. Conduction velocity (CV) and threshold for alternans monotonically increased with coupling. Lower coupling enhanced Ca^{2+} alternans amplitude, but the spatial spread of early (<2Hz) alternation was the greatest under intermediate (not low) coupling. This non-monotonic relationship was closely matched by the percent of samples exhibiting large-scale alternans at higher pacing rates. Computer modeling corroborated these experimental findings for strong but not weak electromechanical (voltage-Ca^{2+}) coupling, and offered mechanistic insight. In conclusion, using experimental and modeling approach, we reveal a general mechanism for the spatial spread of subtle cellular Ca^{2+} alternans that relies on combination of gap-junctional and voltage-Ca^{2+} coupling.

Figure 20. Simulation results from classic diffusion equation. Panel A: Using an analytical solution of the generic diffusion equation for two-dimensional medium and a Dirac function of concentration change as initial condition, we obtain the spatial profiles at a fixed time for different degrees of coupling. B: Quantification of spatial patterns (from A) by imposing a threshold (left); average concentration after a fixed time as function of diffusion properties (middle); area of concentration above a threshold as function of diffusion properties (right).

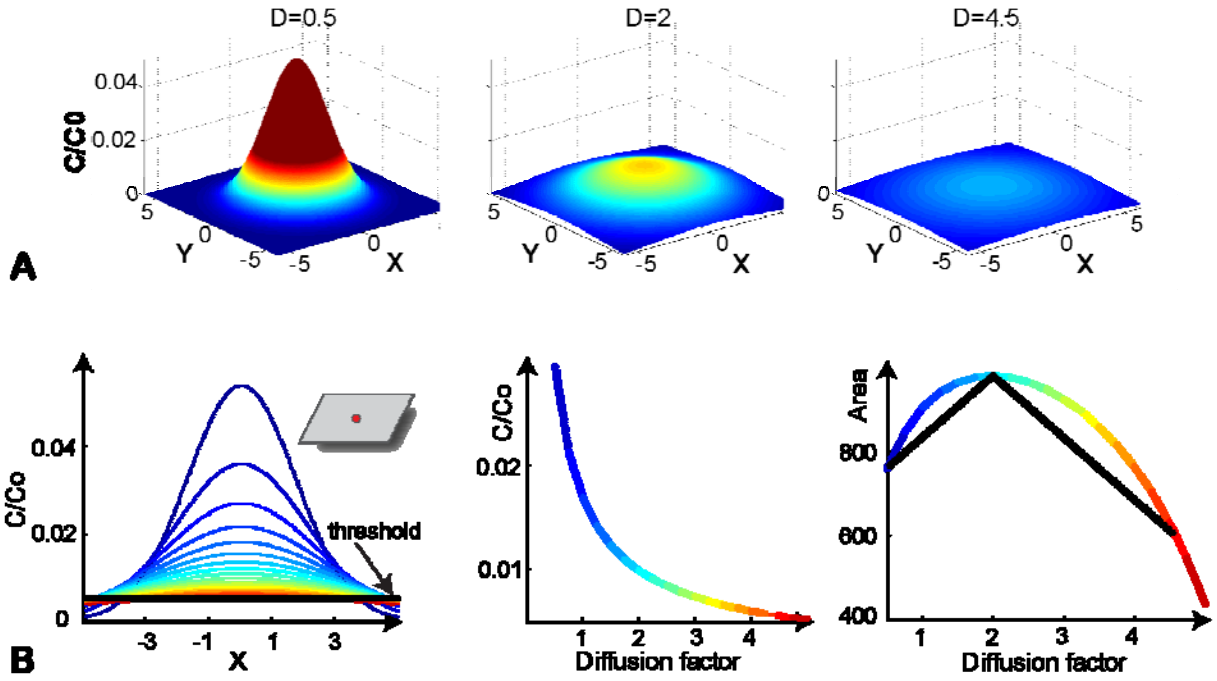

Figure 21 Theoretical explanation of the effects of coupling on the spatial properties of Ca^{2+} alternans. Using a computational model of cardiac tissue, an island of Ca^{2+} alternans (*inset*) was simulated under different coupling conditions. Quantification of spatial patterns by imposing a threshold (*A*) average AR under 4 Hz pacing as a function of diffusion properties (*B*); area of Ca^{2+} alternation above a threshold as a function of diffusion properties (*C*). Color (*blue to red*) indicates low to high diffusion. Compare panel B to Fig. 18D, and panel C to Fig. 18, E and *F*. (*D*). Schematic illustration of the effective diffusion of Ca^{2+} alternans via $D_{v:}$ in a cell pair or a cable. (*E*) In the cell/region exhibiting instability (*gray*), Ca^{2+} alternans drive V_m alternans, which propagate according to D_v. In the distant cell/region, V_m alternans cause Ca^{2+} alternans, thus effectively mediating diffusion of Ca^{2+} alternans. (*F*) Effects of V_m-Ca^{2+} coupling on the diffusion of Ca^{2+} alternans: same simulations as in *A*, but under low V_m-Ca^{2+}. Ca^{2+} alternans do not spread outside the unstable region (*E*) because of negligible V_m alternans amplitude and low V_m-Ca^{2+} coupling in this case (*G*).

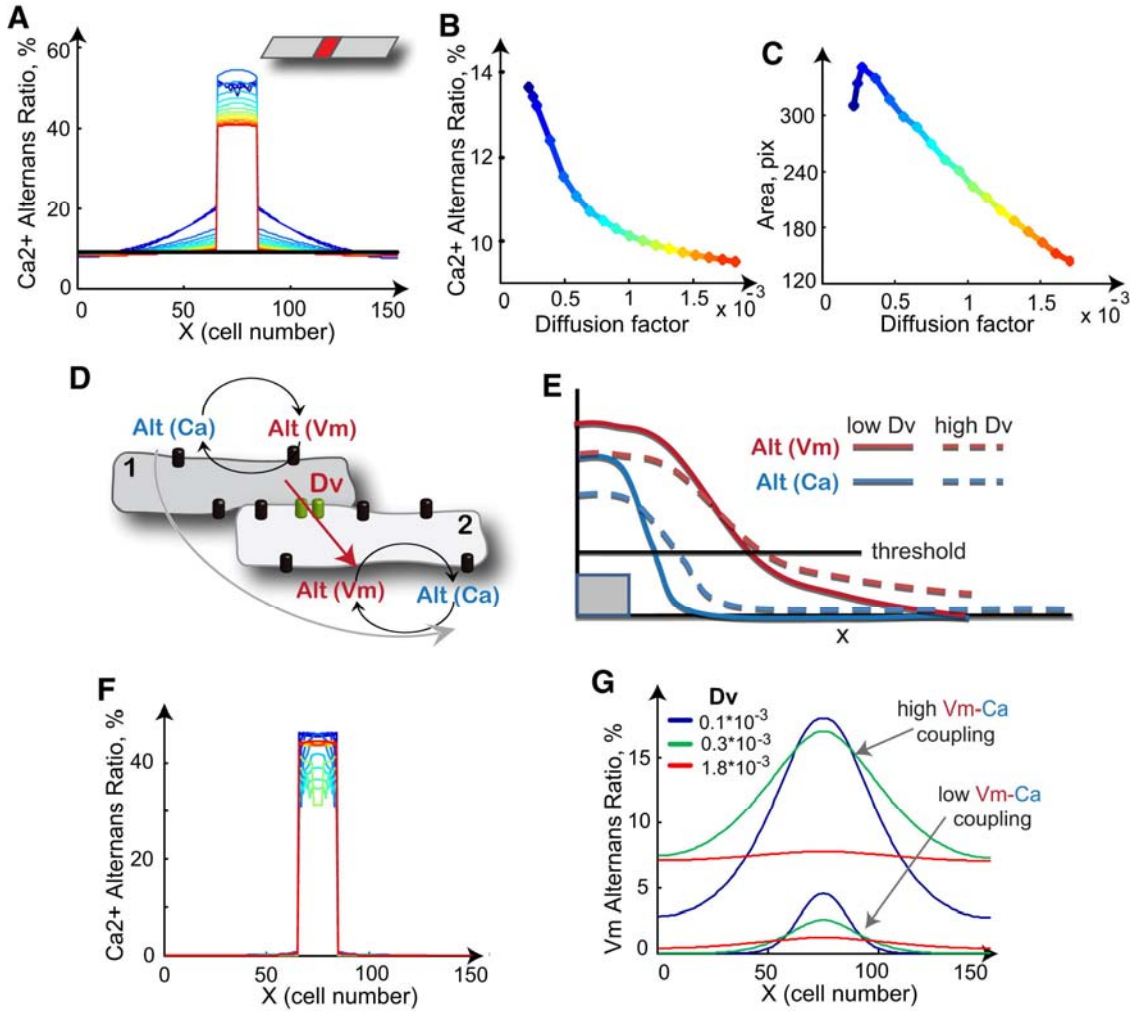
A
Ca2+ Alternans Ratio, %
X (cell number)
B
Ca2+ Alternans Ratio, %
Diffusion factor
x 10^-3
C
Area, pix
Diffusion factor
x 10^-3
D
Alt (Ca)
Alt (Vm)
Dv
1
2
Alt (Vm)
Alt (Ca)
E
low Dv
high Dv
Alt (Vm)
Alt (Ca)
threshold
x
F
Ca2+ Alternans Ratio, %
X (cell number)
G
Dv
0.1*10^-3
0.3*10^-3
1.8*10^-3
high Vm-Ca coupling
low Vm-Ca coupling
Vm Alternans Ratio, %
X (cell number)

Figure 22 Using the amplitude equation to simulate the effects of coupling on the spatial properties of Ca2+ alternans. Panel A: Amplitude of calcium alternans, c_p, as function of the effective diffusion coefficient for voltage, ξ_v. Compare to experimental results in Fig 18D, and model results in Fig 21B and Fig 20B. Panel B: Quantification of the area of local alternation (above a threshold of 1.2) as function of the effective diffusion factor, ξ_v. Compare to experimental results in Fig 18E-F, and model results in Fig 21C and Fig 20B.

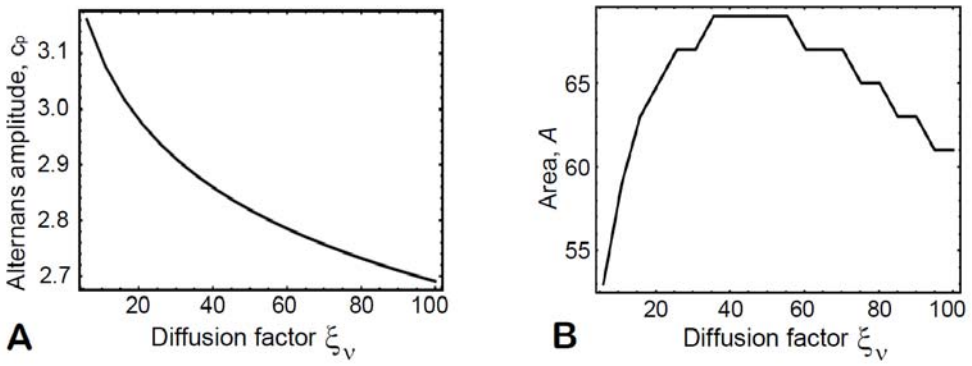

Figure 23. Assessing wavefront fractionation upon uncoupling with low doses of heptanol. **A. A**n example wavefront with a fitted curve (isochrone) and the actual points having the same activation time. **B.** Calculation of residuals and norm for the shown example. **C.** Summary of results for wavefront fractionation (norm/N, where N is the number of points in the wavefront) for control, 0.25 mM and 0.5 mM heptanol treated; number of samples indicated, mean±SEM.

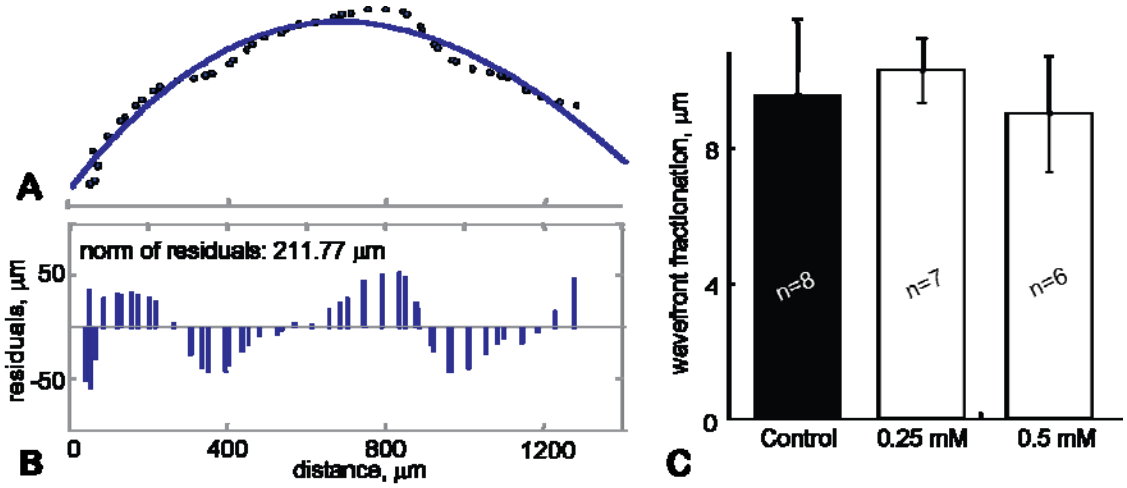

Chapter 5

THE DEVELOPMENT OF CARDIAC OPTOGENETICS BY CELL DELIVERY AND ITS APPLICATION TO FINE ALTERNANS VERIFICATION

5.1 Abstract

Even though computer simulations have predicted the existence of subtle fine-scale intracellular Ca^{2+} alternans, and our experimental results have shown that alternans happens much earlier than detectable VT and VF episodes, they may also be caused or exaggerated by virtual electrode effects. Inspired by recent progress of optogenetics in neuroscience, we developed a tandem cell unit (TCU) strategy and pioneered the application of optogenetics to cardiac muscle where non-excitable cells carry exogenous light-sensitive ion channels, and when electrically coupled to cardiomyocytes, produce optically-excitable heart tissue. For the first time, we combined optical excitation and optical imaging to capture light-triggered muscle contractions and high-resolution propagation maps of light-triggered electrical waves, found to be quantitatively indistinguishable from electrically-triggered waves. Moreover, optical pacing in this case uses less energy, offers superior spatiotemporal control, remote access and can serve not only as an elegant tool in arrhythmia research.

This new optogenetic approach is used here to compare fine-scale Ca2+ alternans induced by electrical and by optical stimulation, where we expect that virtual electrodes present in electrical stimulation will be eliminated by optical stimulation using a depolarizing light-sensitive ion channel, Channelrhodopsin2 (ChR2).

This chapter is based on published work [121].

5.2 Introduction

The non-monotonic relationship between alternans and intercellular coupling and the existence of fine scale alternans are the two most interesting findings in my dissertation research, and the former has been verified by computer simulations. However the origin of fine alternans is not fully understood.

A plausible reason for initiating spatially-discordant alternans could be virtual electrode effect, in which local electrical field produces heterogenous polarization, i.e. areas of positive and negative polarization of various amplitudes in close proximity [122, 123]. A bipolar point or line source electrode will inevitably produce such spatially non-uniform electrical field. Furthermore, due to the intrinsic heterogeneity of cardiac tissue, there will be small "islands" with various degrees of membrane refractoriness superimposed with large-scale changes in transmembrane potential in cardiac tissue. As a result, the alternans emerging in electrically-paced tissue could be due to these heterogenous membrane polarizations. Optogenetics-based pacing works by a different mechanism leading to direct channel-mediated depolarization without creation of virtual electrodes. Therefore, we pursued this new technology to assess the potential contribution of virtual electrodes to the development of fine-scale Ca2+ alternans in cardiac tissue.

The simplest known opto-electrical transducers in nature are a class of light-sensitive transmembrane proteins, best represented by bacteriorhodopsin, converting photons into transmembrane voltage via proton pumping. Since their discovery[124], the prokaryote rhodopsins have been viewed as potential bioelectronics components[125] due to offered ultra-fine spatiotemporal control by light. The latter is of equal interest in excitability control of eukaryotic cells. The cloning of Channelrhodopsin2 (ChR2) by Nagel, Hegemann and his colleagues expanded the field beyond microorganisms [126]. These ion channels provide excitatory current with relatively fast kinetics and can effectively trigger electrical impulses (action potentials) in excitable cells. Since 2005[127, 128], numerous neuroscience applications in vitro and in vivo delineated a new research area, termed "optogenetics" [127, 129-135] – the

precise interrogation, stimulation and control by light of excitable tissue, genetically altered to become light-sensitive.

Use of optogenetics in other excitable tissues, e.g. cardiac, skeletal, smooth muscle, has been virtually non-existent until very recently [136-138]. At the end of 2010, Bruegmann et al.[136] combined viral expression of a ChR2 variant with a CAG promoter into mouse embryonic stem cells (ESCs) with targeted differentiation and purification of ESC-derived cardiomyocytes for in vitro demonstration of optical pacing. They also generated transgenic mice with cardiac ChR2 expression, in which normal rhythm was perturbed by light pulses and focal arrhythmias were induced by long pulses. A transgenic zebra fish was used by Arrenberg to spatially map the exact cardiac pacemaking region by structured illumination [137]. At the same time, our group succeeded in developing the first non-viral strategy to optogenetics that does not rely on embryogenesis and is applicable at the syncytial level – work presented in abstract form in 2010[138], and reported here.

Unlike the brain, cardiac tissue is composed of densely packed, highly coupled cardiomyocytes, integrating electrical and mechanical function. The heart's electromechanical function requires synchrony of excitation waves for efficient global contraction, achieved by cell-cell coupling via gap junction channels formed by Connexin43 (Cx43) in the ventricular portion of the heart. Here, we exploit the heart's high coupling aspect, to develop and validate a non-viral cell delivery system for expression of light-sensitive ion channels. Fig. 24 illustrates the concept of a "tandem cell unit" (TCU), formed by a host cardiomyocyte and a non-excitable donor cell, carrying exogenous ion channels, e.g. ChR2. Biophysically, for this unit to be functional (to fire an action potential upon light excitation), low-resistance coupling is needed for closing the local electric circuits. Our group has previously validated this concept for generation

of a two-cell pacemaking unit using cardiomyocytes and stem cells expressing a pacemaking ion channel[139].

The TCU strategy, if proven successful, not only has potential safety advantages over viral delivery methods used in all prior optogenetics studies, but also may be applicable for study and treatment of cardiac rhythm disorders. In this section, we demonstrate the utility of optogenetics to create optically-excitable cardiac muscle, extendable to in vivo applications, and demonstrated the existence of fine scale alternans under optical pacing, which eliminates the virtual electrode effects.

5.3 Materials and methods

5.3.1 Development of a ChR2-expressing stable cell line

A bacterial stock containing the pcDNA3.1/hChR2(H134R)-EYFP plasmid was obtained from Addgene and amplified in selective Luria-Bertani (LB) medium. Plasmid DNA was extracted using Qiagen HiSpeed Plasmid kit (Qiagen, Valencia, CA), ethanol-precipitated and resuspended in endotoxin-free water for use in cell trasnfections. After verification of identity by restriction digestion and sequencing, it was stored at -20°C at the obtained concentration (typically 2-4 g/ml), later diluted to 1 g/ml for transfection.

HEK293 cells (ATCC, Manassas, VA) were transfected with the plasmid using Lipofectamine™ 2000 (Invitrogen) as directed: 4 g of DNA and 10 g of Lipofectamine in 250 l medium for a 35mm dish with cells. Gene expression was examined by EYFP signal the next day. 48 hours after transfection, cells were switched to selection medium, containing 500 g/ml Geneticin (GIBCO Invitrogen). The selected cells with a high fluorescence signal were maintained in Geneticin (500 g/ml) containing culture medium at 37° in a humidified atmosphere incubator

with 5% CO_2 and 95% air. Expanded HEK cell cultures showing near 100% expression were frozen at -80C for later use. Immediately prior to use, the HEK-ChR2 cells were grown in DMEM (Dulbecco's Modified Eagle's Medium, GIBCO Invitrogen) supplemented with 10% FBS (fetal bovine serum, Sigma-Aldrich, St Louis, MO) and 1% penicillin-streptomycin (Sigma) at 37°, 5% CO_2. Expression and functional properties were confirmed in passages 2 to 20 and used in co-culture experiments with cardiomyocytes.

5.3.2 Confirmation and analysis of light-triggered ChR2-current in the cell delivery system

ChR2 cell membrane expression was confirmed in virtually 100% of the transfected HEK cells (Fig. 21a) using EYFP fluorescence as a marker. For functional measurements of the ChR2-current, the HEK-ChR2 cells were harvested by trypsinization, replated at low density on polylysine-coated coverslips and stored in DMEM medium at 37° in a humidified atmosphere incubator with 5% CO_2. The membrane current was recorded in single cell by whole-cell patch clamp with an Axopatch 1D amplifier (Axon instruments Inc, Foster City, CA). Borosilicate glass pipettes (World Precision Instruments Inc., Sarasota, FL) were pulled on a Flaming-Brown–type pipette puller (Sutter Instrument Co, Novato, CA) and heat-polished before use. Pipette resistances measured in Tyrode's solution were 3-4 MΩ when filled with pipette solution. The pipette solution contained (mmol/L) potassium aspartate 80, KCl 50, $MgCl_2$ 1, MgATP 3, EGTA 10 and HEPES 10 (pH 7.4 with KOH). The external solution contained (mmol/L) KCl 5.4, NaCl 140, $MgCl_2$ 1,$CaCl_2$ 1.8, HEPES 10 and Glucose 10 (pH 7.4 with NaOH). Membrane currents were recorded, digitized (DIGIDATA 1320A, Axon Instruments) and stored for offline analysis. There was a liquid junction potential of ~10 mV between the bath solutions and the electrode solution. The current was recorded as depolarizing 500ms pulses from -80 mV to

+50mV with and without illumination (Fig. 21). The light-triggered ChR2- current was determined by subtracting the "off" light trace from the recorded response of light "on". Illumination pulses were generated using the microscope-attached fluorescence light unit, filtered at 470nm. The light-triggered inward ChR2-current was reproducible upon repeated on/off light pulses.

The kinetics of light-triggered ChR2-current was examined as the cells were clamped at -80mV after obtaining whole-cell configuration, and light pulses of variable duration and spacing were applied sequentially. For the analysis of the current kinetics – activation and deactivation time-constants - nonlinear sigmoidal curve fit was applied to the rising and the falling portion upon light on/off pulse (Fig. 25d-e). The slope parameter (τ_{sl}) was quantified.

The kinetics of light-triggered ChR2-current was examined as the cells were clamped at -80mV after obtaining whole-cell configuration, and light pulses of variable duration and spacing were applied sequentially. For the analysis of the current kinetics – activation and deactivation time-constants - nonlinear sigmoidal curve fit was applied to the rising and the falling portion upon light on/off pulse (Fig. 25d-e). The slope parameter (t_{sl}) was quantified.

5.3.3 Optically-excitable cardiac syncytium: primary cardiomyocyte cell culture and co-culture with HEK-ChR2 cells

Neonatal Sprague-Dawley rats were sacrificed and cardiomyocytes were isolated by an approved Stony Brook University IACUC protocol as previously described[140-144]. Briefly, the ventricular portion of the hearts was excised and washed free of blood. The tissue was cut into small pieces and enzymatically digested overnight with trypsin at 4° (1mg/ml, USB, Cleveland, OH), and then with collagenase at 37° (1mg/ml, Worthington, Lakewood, NJ) the next morning.

Cardiac fibroblasts were removed by a two-stage pre-plating process. In some transfection experiments, these cardiac fibroblasts were used in conjunction with electroporation.

Cardiomyocytes were then plated onto fibronectin-coated glass coverslips at high density: 4×10^5 cells/cm^2 for the control myocyte group and 3.5×10^5 cells/cm^2 for the co-culture groups, mixed with approximately 7,700 or 3,500 HEK cells (for 45:1 and 100:1 initial plating ratios) onto glass bottom dishes in M199 medium (GIBCO Invitrogen) supplemented with 10% fetal bovine serum (GIBCO Invitrogen) for the first 2 days and then reduced to 2%. Cultures were maintained in an incubator at 37° with 5% CO_2 for 4 to 5 days before functional measurements.

5.3.4 Direct expression of ChR2-EYFP in cardiomyocytes, cardiac fibroblasts and mesenchymal stem cells

Freshly isolated neonatal rat cardiomyocytes and cardiac fibroblasts, as well as mesenchymal stem cells, were transfected by electroporation using a Nucleofector device (Amaxa Lonza, Gaithersburg, MD) as follows: 4 g of plasmid DNA was mixed with 100 l of nucleofector solution for transfecting $4x10^6$ cells. Human mesenchymal stem cells (hMSC) were purchased from Clonetics/BioWhittaker, Walkersville, MD, USA, and cultured in mesenchymal stem cell growth medium - Poietics-MSCGM (BioWhittaker). Canine mesenchymal stem cells (cMSC) were isolated from the bone marrow of adult dogs and cultured in Poietics-MSCGM. Flow cytometry revealed 93.9% $CD44^+$ and 6.1% cells were $CD34^+$. Cells with spindle-like morphology were selected after flow cytometry characterization and replated for use. Transfected cells were incubated in normal culture conditions. Similar conditions were used to transfect cardiac fibroblasts or stem cells via electroporation. Expression of fluorescence was detected 24 to 48 hours after transfection using confocal fluorescence imaging.

Images were processed as follows: background fluorescence was first subtracted for images of control (non-transfected) and transfected cells of the same type. Then the remaining integral fluorescence over identical areas was used to form a ratio (transfected/average control) in order to quantify and compare different cell types, as shown in Fig. 26.

5.3.5 Demonstration of TCU functionality in cell pairs of adult canine ventricular myocytes and HEK-ChR2

Adult mongrel dogs were euthanized as per IACUC protocol at Stony Brook University by intravenous injection of sodium pentobarbitone (80mg/kg body weight) and the heart was removed. Canine ventricular cells were isolated using a modified Langendorff procedure[145] perfusing a wedge of the left ventricle through a coronary artery with 0.5 mg/ml collagenase (Worthington) and 0.08 mg/ml protease (Sigma) for 10 min before tissue digestion. Prior to plating, isolated cardiomyocytes were stored in Kraft-Brühe (KB) solution (in mM: KCl, 83; K2HPO4, 30; MgSO4, 5; Na-Pyruvic Acid, 5; b-OH-Butyric Acid, 5; Creatine, 5; Taurine, 20; Glucose, 10; EGTA, 0.5; KOH, 2; and Na2-ATP, 5; pH was adjusted to 7.2 with KOH) at room temperature. The canine ventricular myocytes were plated onto laminin-coated glass coverslips (10 mg/ml, Invitrogen) and incubated in a 37℃ to ensure attachment. HEK-ChR2 cells were added within 24h at low density to stimulate formation of individual cell pairs and the co-culture was maintained in Medium 199 (Gibco) supplemented with 15% FBS, 2 mm L-glutamine, 100 U/ml penicillin, 100 μg/ml streptomycin and 50 μg/ml gentamicin.

Dual patch clamp experiments were performed within 48 hours after plating. Briefly, experiments were carried out on heterologous (HEK-ChR2 - canine myocyte) cell pairs within 48 hours after plating, as described previously [146]. A dual whole-cell voltage-clamp method was used to control and record the membrane potential of both cells and to measure associated

membrane and junctional currents [146-148]. Each cell of a pair was voltage clamped at the same potential by two separate patch clamp amplifiers (Axopatch 200, Axon Instruments). To record junctional conductance, brief voltage steps (±10 mV, 400 ms) were applied to one cell of a pair, whereas the other cell was held at constant voltage and the junctional currents were recorded from the unstepped cell. Membrane and action potentials were recorded in current-clamp mode.

For electrical recordings, glass coverslips with adherent cells were transferred to an experimental chamber mounted on the stage of an inverted microscope (Olympus-IX71) equipped with a fluorescence imaging system. The chamber was perfused at room temperature (~22 °C) with bath solution containing (in mM): NaCl, 140; Mg Cl2, 1; KCl, 5; CaCl2, 2; HEPES, 5 (pH 7.4); glucose, 10. Perfusion with 200mM of carbenoxolone (Sigma) was used to block cell-cell communication. The patch pipettes were filled with solution containing (in mM): K+ aspartate-, 120; NaCl, 10; MgATP, 3; HEPES, 5 (pH 7.2); EGTA, 10 (pCa ~8). Patch pipettes were pulled from glass capillaries (code GC150F-10; Harvard Apparatus) with a horizontal puller (DMZ-Universal, Zeitz-Instrumente). When filled, the resistance of the pipettes measured 1-4MΩ.

5.3.6 Immunostaining of co-cultures

For immunocytochemistry, the co-cultures were fixed and permeabilized with 3.7% formaldehyde and 0.02% Triton-X 100 before being stained with a monoclonal mouse antibody against sarcomeric -actinin (Sigma). Samples were visualized using goat anti-mouse antibody conjugated with fluorophore Alexa 546 (Invitrogen) and imaged on the Olympus FluoView confocal system.

5.3.7 Western blots of Cx43 and T-tubulin

Cells from three groups (HEK293, HEK+ChR2 and stably transfected HeLa+Cx43 cells) were collected, lysed and centrifuged to obtain a pellet. The pellets were re-suspended in cold RIPA buffer (R0278, Sigma), protease Inhibitor cocktail (P2714, Sigma), sodium orthovanadate (S-6508, Sigma) and PMSF (P-7626, Sigma); after centrifugation, the supernatants were transferred to pre chilled microtubes. Protein concentration for each sample was determined by the Bradford assay. Total protein of 30 micrograms from each lysate was mixed with equal volume of laemmli sample buffer (161-0737, Bio-Rad, Hercules, CA) containing β-mercaptoethanol and boiled for 5 minutes at 95˚C. After centrifugation, samples were loaded on a SDS-polacrylamide gel. MagicMark XP Protein Standard (LC5602, Invitrogen) was loaded along with the samples. After separation by electrophoresis at 115 V for 90 minutes in tris-glycine/SDS buffer, proteins were transferred to immobilon-P membrane (Millipore, Billerica, MA) by electrophoresis at 100 V for 60 minutes in tris-glycine/methanol buffer. Nonspecific antibody binding was blocked for 1 hour by 5% blotting grade blocker non-fat dry milk (Bio-Rad) dissolved in 1x TBST. The following antibodies were used: primary anti-Cx43 antibody raised in rabbit (C 6219, Sigma), secondary goat-anti-rabbit antibody (sc-2004, Santa Cruz); a primary antibody for -tubulin at 55kD (sc-8035, Santa Cruz), and a secondary goat-anti-mouse antibody for tubulin from Pierce, Rockford, IL. The secondary antibodies were detected using SuperSignal West Femto Maximum Sensitivity Substrate (34095, Pierce) and images obtained by exposing the membrane to HyBlot CL autoradiography film. Quantification of the Cx43 bands relative to the -tubulin bands was done using a buil-in routine in ImageG.

5.3.8 Ultra-high resolution optical mapping of cardiac excitation waves triggered by light in co-cultures

Two-dimensional optical mapping over a large field of view (about 2.2cm) was done with a custom-developed macroscopic system allowing for ultra-high spatiotemporal resolution [143, 144]. The system (Fig. 4a) includes a CMOS camera (pco, Germany) recording images at 200 frames per second (fps) over 1,280×1,024 pixels), a Gen III fast-response intensifier (Video Scope International, Dulles, VA), collecting optics (Navitar Platinum lens, 50mm, f/1.0) and filters, excitation light source (Oriel with fiber optics lights guides) and an adjustable imaging stage. Subcellular spatial resolution was achieved – about 22 mm per pixel. All measurements were done in normal Tyrode's solution at room temperature. Quest Rhod-4 (AAT Bioquest, Sunnyvale, CA) was used to label the cells for tracking Ca^{2+} waves. This optical dye was chosen for wavelength compatibility with ChR2 and EYFP excitations/emissions. 525 nm excitation light for Ca^{2+} recording was delivered through non-conventional distributed tangential illumination (90° angle with respect to the optical axis) to accommodate optical stimulation but also to achieve superior contrast by complete uncoupling of the Rhod-4 excitation from the light-gathering optics. Excitation light for Rhod-4 was provided by a QTH lamp with a branching liquid light guide, attached to a custom designed experimental chamber with reflective inner walls and open bottom surface, accommodating a 35 mm dish with the sample. Emitted Rhod-4 fluorescence was collected at 585 nm through an emission filter in front of the intensified camera on top of the sample.

All movies of propagation were acquired using CamWare (pco, Germany) data acquisition software. Raw data were binned (2×2) and analyzed in custom-developed Matlab software to extract quantitative information about calcium transient morphology, conduction

velocity etc. Activation maps (based on time of maxiumum rise in Ca^{2+}) and phase movies (using the Hilbert transform) were generated after filtering spatially (Bartlett filter, 5-pixel kernel) and temporally (Savitsky-Golay, order 2, width 11) [142, 144].

5.3.9 Electrical and optical pacing

For records of electrically-triggered activity, cells were paced by Pt electrodes, connected to a computer-driven Myopacer stimulator (IonOptix, Milton, MA). Excitation pulses for light-triggered activity were delivered through the bottom of the dish from an optically focused light from an LED (470nm, 1.35 cd, 20mA, 5mm, 30deg angle) from Optek Technology (Carrollton, TX), connected to the TTL output of a second computer-driven Myopacer stimulator. Irradiance (in mW/cm^2) was measured at the cell monolayer site using a Newport digital optical power meter Model 815 (Newport, Irvine, CA), with a sensor area of 0.4cm*0.4cm. Through the bottom of a 35mm polystyrene dish, we measured about 0.16mW, thus irradiance of about $1mW/cm^2$.

5.3.10 Recording light-triggered contractions

Microscopic imaging for confirmation of gene expression or for documenting contractions by optical excitation was done with the Olympus FluoViewTM FV1000 confocal system at room temperature. Hamamatsu ImagEM EMCCD camera (Hamamatsu, Bridgewater, NJ), attached to the Olympus FluoViewTM FV1000 microscope, was used to record contractility movies at 20 fps with a 60X oil lens (NA=1.42), using SlideBook 5 software (Intelligent Imaging Innovations, Denver, CO). In addition, contractility response was also documented by automatic optical tracking of cell length at 250Hz using an IonOptix videosystem (IonOptix) attached to a Nikon TE2000 inverted microscope [140].

5.3.11 Carbenoxolone treatment to test effects of cell coupling on TCU

Carbenoxolone, CBX, (Sigma), a gap junctional uncoupler[146], was used here at concentration 200mM in the dual-patch experiments with canine CM and HEK-ChR2 or in cardiac syncytium of neonatal rat CM and HEK-ChR2. In the latter case, CBX was applied for 20min (without perfusion) in the co-cultures of HEK-ChR2 cells and cardiomyocytes. Contractility movies were recorded in response to optical pacing before and during administration of carbenoxolone, and upon washout to assess the role of gap junctional coupling in the functionality of the TCU.

5.4 Resutls

5.4.1 Development and characterization of a cell delivery system for non-viral optogenetics

To validate the TCU strategy for cardiac optogenetics, as a proof of principle, we developed a stable HEK cell line expressing a variant of ChR2. Fig. 25a-e illustrates the development of such donor cell line. Successful expression is possible in other non-excitable cell types, including mesenchymal stem cells, Fig. 28, that may yield more clinically relevant cell delivery systems. Preserved expression and functionality were established for the HEK-ChR2 cell line after multiple freeze-thaw cycles and multiple passages (passages 2 to 30 were used for functional experiments), Fig. 22a-b.

Conformation of ChR2 functionality was done by a whole-cell voltage clamp. Using voltage ramp protocol in single HEK-ChR2 cells (Fig. 25c) reveals that the channel is closed and non-contributing during dark periods regardless of transmembrane voltage, and has a mildly inwardly rectifying current-voltage relationship when blue light is applied. Recent comprehensive characterization of ChR2 current kinetics indicates fast activation (<5ms), deactivation (<10ms) and inactivation (<50ms)[149], thus making it suitable as excitatory (action

potential – generating) current for cardiomyocytes during external optical pacing at relevant frequencies (5-12 Hz for rodents, 1-3 Hz for humans). Indeed, our kinetics characterization (Fig. 25d-e) estimates the activation and de-activation time constants for ChR2-mediated current in the ms range. Therefore suitable rates for cardiac pacing are attainable even without genetic modifications, as previously done for neural applications (up to 200Hz) [132].

In contrast to the robust expression of ChR2 in HEK cells, much lower yield was seen when directly transfecting cardiomyocytes with ChR2 using nucleofector electroporation. This prevented direct synthesis of a large-scale ventricular syncytium from ChR2-expressing myocytes. Nevertheless, individual ChR2-expressing neonatal rat ventricular myocytes were excitable and contracting when optically stimulated and quiescent otherwise.

5.4.2 Validation of the TCU strategy for cardiac excitation

The TCU approach for cardiac optogenetics, i.e. inscribing light-sensitivity into cardiomyocytes and cardiac tissue without direct genetic modifications, was validated in cell pairs of CM and HEK-ChR2 cells, as well as in synthesized large-scale cardiac syncytium (Fig. 26a). ChR2 expression was verified by EYFP in the donor cells, with confirmed Cx43 (Fig. 26b), found to aggregate in small clusters within cardiac syncytium of neonatal rat CM, Fig. 26a. Functional response of TCU to optical stimulation was first confirmed in cell pairs of adult canine CM and HEK-ChR2 cells using dual-clamp to estimate coupling and to record light-triggered action potentials in the cardiomyocytes, Fig. 26c-d. Because of the spontaneous cell pair formation, it was not possible to control the level of cell coupling in the cell pairs of canine CM and HEK-ChR2. However, a very robust response was seen in a wide range of coupling values spanning an order of magnitude (from 1.5 nS to 15 nS). Interestingly, a similar low critical coupling value (1.5 – 2 nS) was found previously in the generation of a two-cell

pacemaking unit by a donor cell carrying HCN2 (a gene encoding for the pacemaking current If) and a cardiomyocyte[146]. Nevertheless, extreme uncoupling abolished the light-sensitivity of the TCU. Pharmacological uncoupling with cabenoxolone provided further proof for gap junctions' critical role in the TCU functionality for neonatal rat and for adult canine myocytes, Fig 26e.

In a functional TCU pair, the cardiomyocyte generated normal action potentials upon stimulation by blue (470nm) light (Fig 22d), indistinguishable from electrically-triggered ones. The donor cell's membrane potential followed passively by a low-pass filtered version of an action potential, Fig. 26d. In spatially-extended (several centimetres) two-dimensional cardiac syncytium of randomly mixed neonatal rat CMs and HEK-ChR2, robust synchronous contractions were registered upon stimulation by blue light

5.4.3 Wave properties of cardiac syncytium in response to optical vs. electrical stimulation

Thus synthesized optically-excitable cardiac tissue was subjected to further functional testing. Synchronized wave propagation is essential for heart's normal functionality and efficient mechanical contraction; lethal arrhythmias occur when the generation or propagation of these excitation waves is altered (failure to initiate, abnormal propagation velocity and/or path). Accordingly, we have developed an ultra-high resolution optical mapping system[143, 144] to dissect cardiac wave propagation during external pacing or arrhythmic activity over a centimeter-scale (>2cm) with subcellular resolution (22um/pix) at 200 fps using fast voltage and calcium-sensitive dyes[143]. This optical mapping system was made compatible with simultaneous optical excitation, Fig. 27a. While mapping was done here with Rhod-4, a calcium-sensitive fluorescent dye, suitable voltage-sensitive probes with similar spectral properties can also be used, e.g. di-4 or di-8-ANEPPS [143]. In normal pacing conditions, cardiac calcium transients

are an excellent surrogate for action potentials, and calcium dyes outperform voltage-sensitive dyes in signal-to-noise ratio.

Optical mapping of propagating waves triggered by localized electrical and optical stimulation in the same sample, revealed similar conduction velocities and calcium transient morphologies (away from the stimulus site), thus confirming equivalent triggering abilities for both, Fig. 27b-e. Pure cardiomyocyte cultures and co-cultures of cardiomyocytes and HEK cells without ChR2 served as controls. At mixing ratio of 100:1 (CM:HEK), conduction velocity in pure myocytes cultures was higher than the mixtures, but presence or absence of ChR2 did not alter propagation Fig. 27e. Note that we have been successful in preserving light-sensitivity for higher mixing ratios (up to 100:1) CM:HEK, which are likely to preserve CV as in pure myocytes layers. Furthermore, electrical and optical pacing in light-sensitive samples (CM:HEK+ChR2) resulted in the wave propagation properties. The controls (CM only and CM+HEK without ChR2) were quiescent and never produced excitation in response to light triggers.

Considering the electromechanical nature of cardiomyocytes, we also show direct light-triggered muscle contraction, confirming intact excitation-contraction coupling in single myocytes or hybrid cardiac tissue Fig. 27f. This demonstration of mechanical response triggered by light-sensitive ion channels suggests development of light-driven actuators with efficient energy transfer and illustrates the feasibility for direct optogenetic control in other muscles.

5.4.4 Energy needs in cardiac optogenetics

Previous studies in neuroscience have reported optical energies used to excite single neurons or brain tissue [127, 129, 150] in a wide range of high values (approximately 800 to 7500 mW/cm^2). The well-coupled spatially-extended cardiac tissue was expected to present

lower input impedance for optical stimulation, thus possibly requiring higher irradiance values. Yet, surprisingly, in Bruegmann et al.'s study [136], significantly lower light levels (50 to 700 mW/cm^2) were sufficient to optically stimulate for a wide range of pulse durations *in vitro* or *in vivo*.

In our TCU approach, during optical pacing in the two-dimensional cardiac syncytium, we measured irradiance at 470nm of approximately 1 mW/cm^2 at the cell site. Interestingly, this is about 1-2 orders of magnitude lower than previously reported values for cardiac excitation[136] when similar longer pulses were used as here (10 to 50ms). The significantly lower optical energy needed in our study may stem from different cellular/tissue properties and superior efficiency of ChR2 expression. Importantly, the TCU strategy is likely to yield favourable conditions for optical excitation and propagation of a pulse into a large well-connected mass of cardiomyocytes. The reduced (compared to CM-CM) coupling between the donor cells, in which charge builds up before reaching threshold, and the host cardiomyocyte(s), that generate the action potential for propagation effectively counters the dissipation of charge (the electrical sink that the myocardium normally presents) while threshold for excitation is being approached. These circumstances qualitatively resemble the conditions where the sino-atrial node reliably drives the large well-coupled ventricular myocardium.

It is important to note, that in contrast to a previous study[136], no (pro-arrhythmic) re-excitations were observed during longer stimulation pulses (up to 1s) at our low illumination intensities, close to the rheobase of the strength-duration curve[151]. This low light intensity is important factor in minimizing heat-related effects, phototoxicity and in considering future implantable devices.

An interesting question concerns comparison of energy needed for electrical vs. optical pacing. In our system, energy needed for supra-threshold stimulation of two-dimensional cardiac syncytium can be estimated as follows: For typical electrical pacing (5V, 0.2A, 0.01s pulses), we obtain 10mJ. For optical stimulation with an LED (5V, 0.02A, 0.01 – 0.05s pulses), we obtain 1 to 5mJ. Considering the possibility for optimization of light focusing, as well as the active development of more efficient light-emitting diodes (more lumens per watt), it is likely that optical stimulation may be more energy efficient than its electrical counterpart. As pacemaking (unlike cardioversion) is a topologically simple problem, i.e. spatially-localized (light-sensitive) cell ensemble can be used; the TCU strategy may prove particularly valuable in pursuing potential clinical applications, given the above energy considerations.

5.4.5 Comparing fine alternans profile under both electrical and optical pacing

Besides intrinsic heterogeneity, another possible reason for fine-scale alternans is the 'virtual electrode' effects typically present in electrical pacing, which cause closely spaced areas of opposite polarity. As shown in Fig.29, during true electric field stimulation (widely spaced electrodes) there is engagement/excitation originating at sites in the "far field" - only excitation region at lower electrical field E=2.9 V/cm, and two excitation regions emerged when E increased to 3.2 V/cm. When electrical pacing is done with closely spaced electrodes (bipolar point or line electrodes), opposite polarity "virtual electrodes" will emerge locally. These could be effective triggers for spatially discordant fine-scale alternans.

In order to test the contribution of these side effects of electrical pacing, optical pacing was adopted by using optogenetics with ChR2. As Fig. 30 shows, firstly we have tested both optical and electrical pacing on myocyte and HEK-ChR2 co-culture samples. And found the physiological and biophysical properties of optically-triggered excitation events were

indistinguishable from those from electrically-triggered excitation events (calcium transient duration, conduction velocity, contractility). Then we compared alternans in tissue scale, there is still no difference between alternans area, region number or alternans ratio within a tissue area of 2.64*2.64 mm. As co-culture tissue inevitably would introduce structural heterogeneity, we repeated the same measurement on electrically paced myocyte only samples and optically paced myocyte+local 8000 HEK-ChR2 cells. Relevant to the topic of this thesis, our experimental data show that, fine-sale alternans did emerge in optically-paced samples and their properties were not significantly different those induced by electrical pacing.

5.5 Conclusion

In summary, our study highlights the utility of optogenetics for cardiac applications by using a strategy inspired by the specific properties of cardiac tissue, i.e. high coupling. The optogenetic approach offers unprecedented spatiotemporal resolution for precise interrogation and control of excitation, seemingly without interfering with essential cardiac tissue properties, as shown here. Therefore, it presents a new versatile actuation tool in cardiac research for dissection of arrhythmias. Furthermore, cardiac optogenetics based on the TCU strategy, presented here, may evolve in a more translational direction and lead to a new generation of optical pacemakers and cardioverter/defibrillators. The feasibility of this is supported by several critical features of the method presented here: 1) desirable pacing rates achievable with the current kinetics of ChR2; 2) finer control of excitation and repolarization in shaping cardiac action potentials, and in terminating arrhythmias is possible by a combination of lights-sensitive ion channels providing outward current[130, 131] and ChR2; 3) the cell delivery platform demonstrated here may offer a safer alternative to viral delivery for in vivo applications; 4) optical fibers are inherently more biocompatible than metal electrode leads for in vivo pacing; 5)

preliminary energy estimates point to potential fold improvements in energy consumption with optical vs. electrical pacing – important for extending battery life in implantable devices.

Finally, we confirmed in a preliminary study that both electrical pacing and optical pacing induced similar Ca2+ alternans profiles, which suggests that the side effects of virtual electrodes may be negligible when considering the spatiotemporal evolution of these instabilities.

Figure 24. The functional "tandem cell unit" (TCU) concept of donor-host cells. Non-excitable cells (e.g. HEK cells here) are transfected to express a light-sensitive ion channel (ChR2). When coupled via gap junctions to excitable cardiomyocytes (CM) they form an optically controllable functional TCU, i.e. the CM will generate an action potential upon light-triggered opening of the depolarizing ChR2 in the HEK cell.

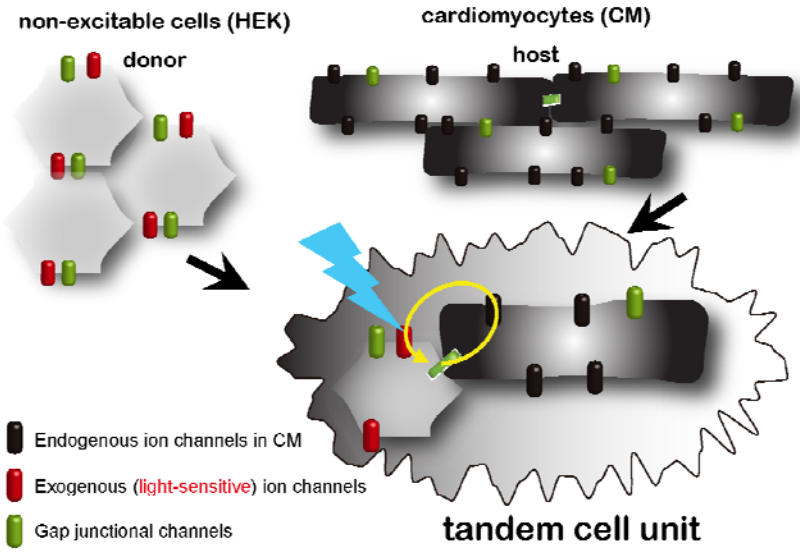

Figure 25. Development and functional characterization of a cell delivery system for ChR2. **a:** Stable HEK-ChR2 cell line – shown is EYFP-reported ChR2 expression in the 10^{th} passage after transfection and purification; scale bar is 50 m. **b**: Voltage-clamp test protocol and example traces for quantification of the steady-state ChR2 current in single HEK-ChR2 cells with 500ms voltage pulses in the range (-80 to +50mV) with and without excitation light for ChR2 on (470nm, 0.24 mW/mm^2). **c**: Example curves for the light-sensitive component after subtraction of current in dark, and the resultant average current-voltage (I-V) relationship for n=12 cells, cell capacitance 43.3±7.5pF, data are presented as mean±SD. **d**: Magnitude of the light-triggered current does not depend on the duration of rest (t rest) or activation (t act), thus indicating relatively fast deactivation in the examined range. Holding potential is -80mV. **e**: Kinetics of activation (on) and deactivation (off), quantified by a $_{sl}$ parameter in the sigmoid curve fits to the light-controlled current transitions (see inset); bar graphs represent mean±SEM.

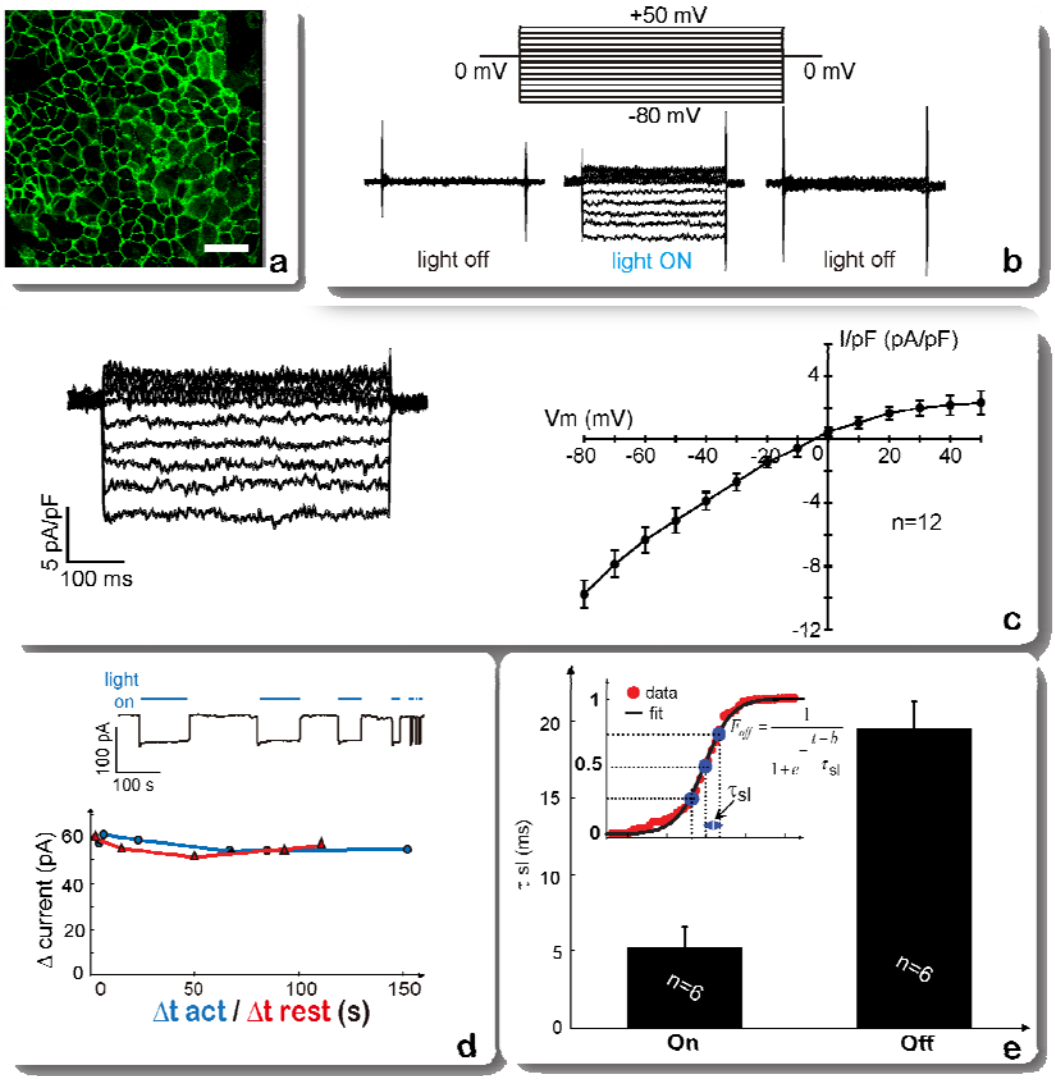
a
+50 mV
0 mV
0 mV
-80 mV
light off
light ON
light off
b
5 pA/pF
100 ms
I/pF (pA/pF)
Vm (mV)
n=12
c
light
on
100 pA
100 s
Δ current (pA)
Δt act / Δt rest (s)
d
data
fit
τsl
τ sl (ms)
n=6
n=6
On
Off
e

Figure 26. Implementation and validation of the TCU concept for neonatal rat CM and adult canine CM coupled to HEK+ChR2 cells. **a**: Phase and fluorescence images of neonatal rat CM and HEK-ChR2 co-culture. Immunostaining in red for -actinin (CMs), green is EYFP-ChR2-expressing HEK cells, typically forming small clusters as shown. Scale bar is 20 m. **b**: Western blot for Cx43 and -tubulin (at 55kD) in the cell delivery system (HEK-ChR2), column 2; column 1 shows a positive control of stably transfected HeLa-Cx43 cells; column 3 shows parental HEK cells without ChR2; column 4 shows the ladder – MagicMark^{TM} bands in kDa; Normalized (Cx43/tubulin) expression is provided for four gels (mean±95%CI). **c**: Histogram of measured coupling conductances in TCUs of canine CMs and HEK-ChR2 cells, n=31, median value of 4nS and IQR (2 – 11nS); red arrow indicates coupling levels allowing optical excitability of the TCUs. **d**: Dual whole-cell voltage clamp of a TCU - adult canine ventricular CM (1) and HEK-ChR2 cell (2). Voltage steps (V1=10mV, 0.4s), applied to the canine CM (cell 1), induced junctional currents (I2) in this cell pair (estimated g.j. conductance of 11nS). **e**: Action potentials in a cell pair (canine CM and HEK-ChR2 cell, phase image on the left) in response to optical pacing (0.13 mW/mm^2, 10ms pulses). Due to coupling, the HEK cell exhibits a low-pass filtered version of the CM-generated action potentials. **f**: Action potentials in a cell pair (canine CM and HEK-ChR2 cell) in response to continuous optical pacing before, during and after washout of uncoupler carbenoxolone (CBX).

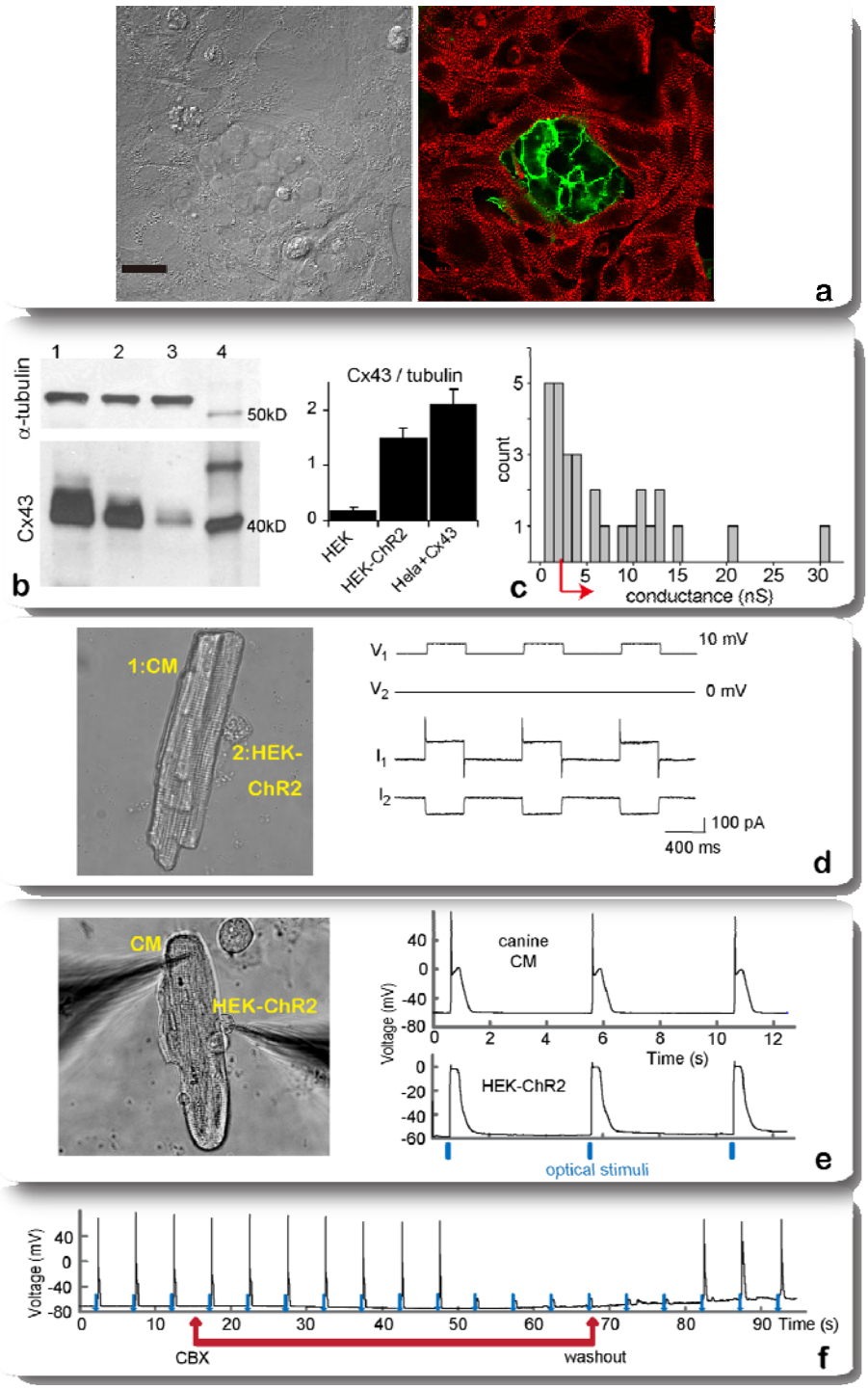
a
1
2
3
4
α-tubulin
50kD
Cx43
40kD
b
Cx43 / tubulin
HEK
HEK-ChR2
Hela+Cx43
count
conductance (nS)
c
1:CM
2:HEK-ChR2
V1
10 mV
V2
0 mV
I1
I2
100 pA
400 ms
d
CM
HEK-ChR2
canine CM
Voltage (mV)
Time (s)
HEK-ChR2
optical stimuli
e
Voltage (mV)
Time (s)
CBX
washout
f

Figure 27. Optical control of cardiac tissue function over space-time: light-triggered excitation waves and light-triggered contractions. **a**: Experimental setup for ultra-high resolution high-speed optical imaging and optical control of cardiac excitation: 1) experimental chamber with tangential light illumination for calcium imaging, focused LED illumination on a moveable stage for ChR2 excitation (see inset on the right); 2) high-NA optics for high-resolution macroscopic imaging; 3) Gen III MCP intensifier; 4) pco 1200hs CMOS camera; 5) light source, excitation filter and optical light guides for tangential excitation; 6) computer system and software for data acquisition and control of electrical and optical stimulation; 7) interface for stimulation control; 8) controllable stimulator for electrical pacing (analog output); 9) controllable stimulator for optical pacing (TTL output). 10) LED for ChR2 excitation, driven by the TTL stimulator output. **b**: Activation maps in a cardiac monolayer by electrical and optical pacing at 0.5Hz. Color represents time of activation; isochrones are shown in black at 0.15s. Calcium transient traces in response to electrical or optical stimulation are shown from 2 locations (A and B), normalized fluorescence. Blue marks indicate time of stimulation (electrical pulses were 10ms, optical – 20ms each). **c**: Normalized Ca^{2+} transients from CM monolayer (red), CM:HEK (black) and CM:HEK+ChR2 co-culture 100:1 (blue) at 1Hz pacing. **d**: Quantification of calcium transient duration (CTD) – CTD25, CTD50 and CTD80 for pure CM monolayer, 45:1 and 100:1 CM:HEK, as well as 100:1 CM:(HEK+ChR2) co-culture under electrical and optical pacing at 1Hz. **e**: Comparison of conduction velocity (CV) among the same 5 groups as in (**d**); for **d** and **e** optical pacing was at irradiance of 0.01- 0.04mW/mm^2, 50ms pulses; data are shown as mean±95%CI; listed number of samples applies to both; **f**: Strength-duration curve (along with the equation for the fitted curve) obtained for optical pacing in co-

cultures (100:1 CM:HEK ratio) at 30°C, n=8, mean±SEM. **g**: Example contractility recording from optically-driven CM+HEK+ChR2 – displacement normalized to cell length. Scale bar is 1s.

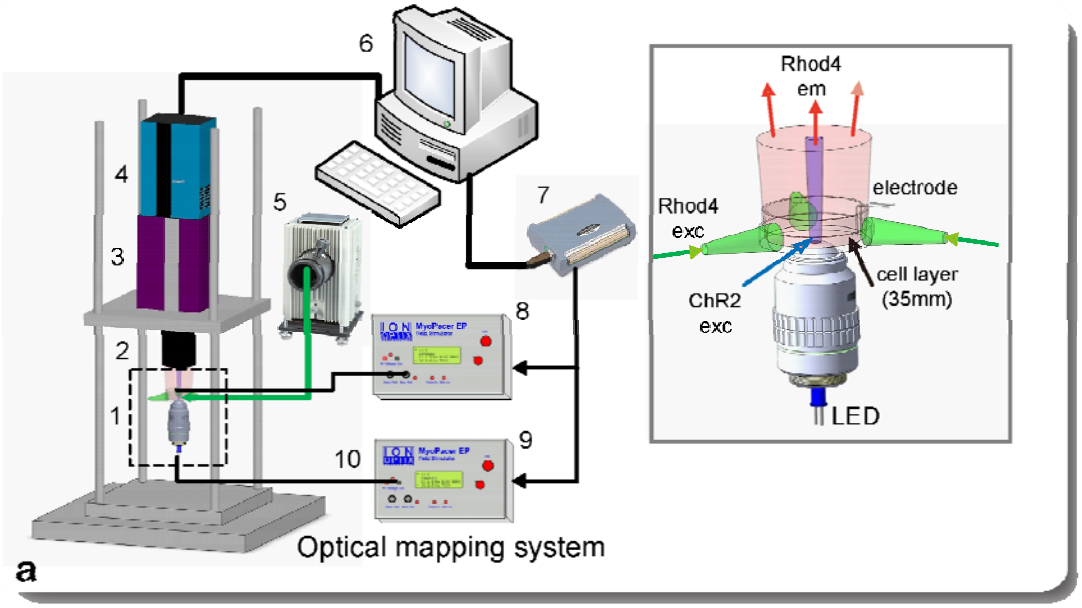
6
4
5
7
3
8
2
1
10
9
Optical mapping system
a
Rhod4
em
electrode
Rhod4
exc
cell layer
(35mm)
ChR2
exc
LED

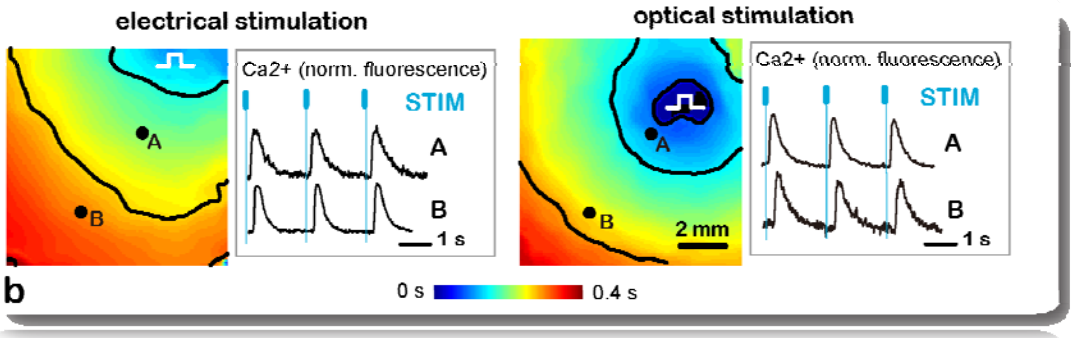
electrical stimulation
optical stimulation
Ca2+ (norm. fluorescence)
STIM
A
B
1 s
2 mm
0 s
0.4 s
b

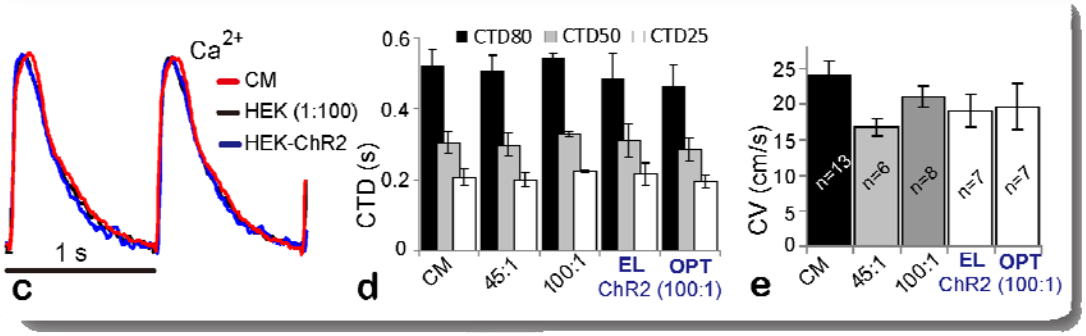
Ca2+
CM
HEK (1:100)
HEK-ChR2
1 s
c
CTD80
CTD50
CTD25
CTD (s)
CM
45:1
100:1
EL
OPT
ChR2 (100:1)
d
CV (cm/s)
n=13
n=6
n=8
n=7
n=7
e

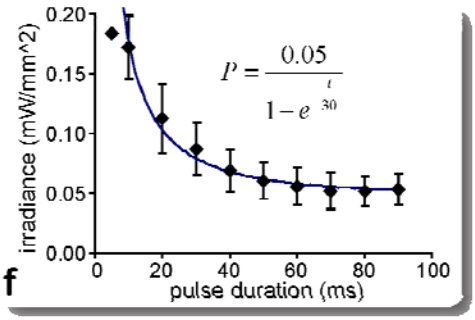
irradiance (mW/mm^2)
pulse duration (ms)
f

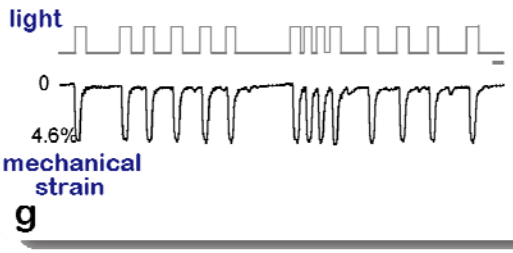
light
0
4.6%
mechanical
strain
g

Figure 28. Direct expression of light-sensitive channels in cardiac cells and mesechnymal stem cells via electroporation. a: Cardiac myocytes express ChR2-EYFP at low efficiency after electroporation (left), control (right); scale bar is 50 m. Panel **b**: Cardiac fibroblasts robustly express ChR2 after electroporation. **c:** Expression of ChR2 in mesenchymal stem cells – canine (cMSC) and human (hMSC). cMSC showed substantially better expression than hMSC. Scale bar is 20 m. Data in the bar graphs are mean±SEM. Normalized fluorescence is the image's total fluorescence normalized by the mean fluorescence from control (non-transfected) cells of the same type. **d:** Phase and fluorescence (EYFP) images of two electroporation-transfected cardiomyocytes, for which movies of optically-triggered contractions are provided. Scale bar is 20 m.

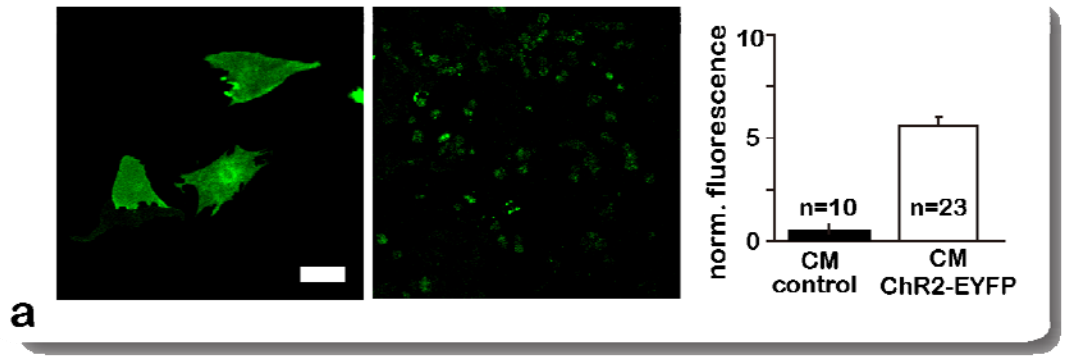
a
norm. fluorescence
10
5
0
n=10
n=23
CM
control
CM
ChR2-EYFP

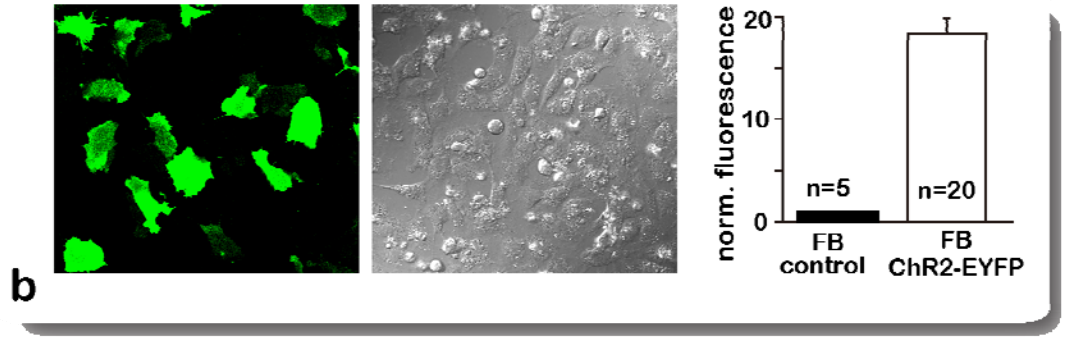
b
norm. fluorescence
20
10
0
n=5
n=20
FB
control
FB
ChR2-EYFP

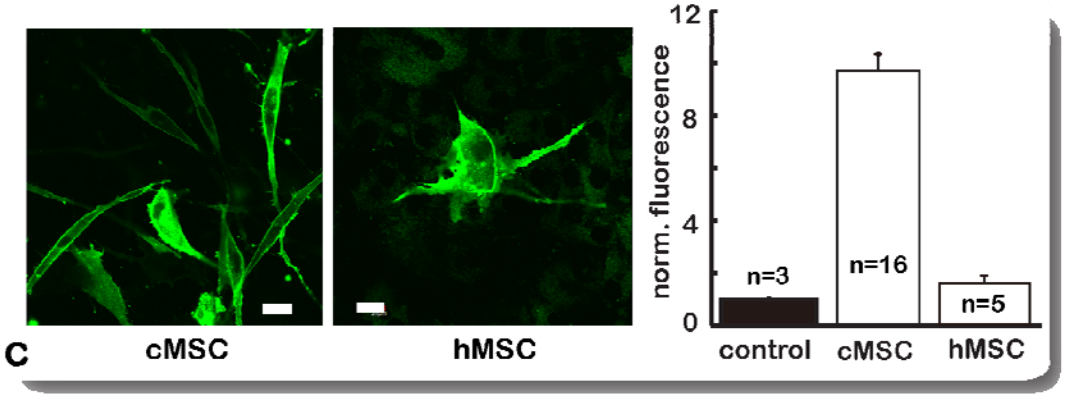
c
cMSC
hMSC
norm. fluorescence
12
8
4
0
n=3
n=16
n=5
control
cMSC
hMSC

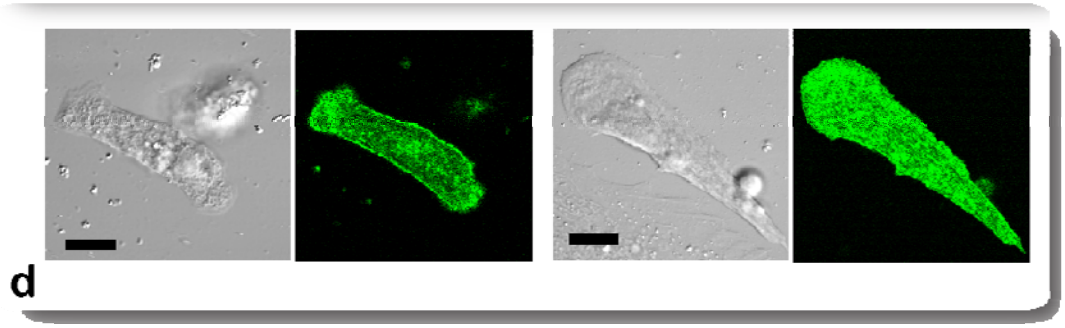
d

Fig.29 Virtual electrode effects on electric field simulated cardiac monolayer. Demonstration of virtual electrode effect: Cardiac monolayer is paced under uniform electrical field at 2.9V/cm and 3.6C/cm. Activation map was captured at 0.02s and 0.04s.

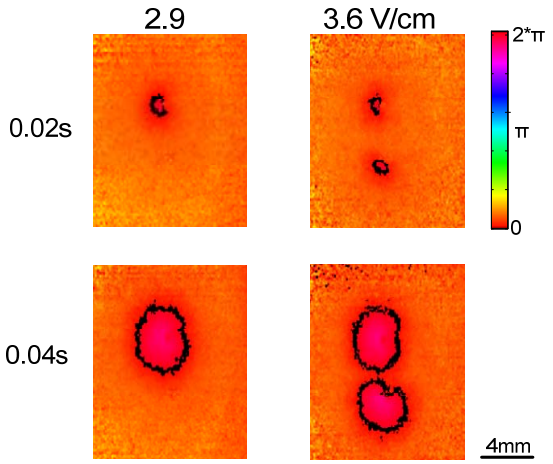

\

Fig.30 Comparison of alternans properties between optical and electrical pacing at 0.5 Hz. Panel A: Representative images of optically and electrically paced co-culture monolayer (2.64*2.64 mm^2), in which the ratio of cardiac myocytes and HEK-ChR2 is 100:1. Green represents no alternans, blue and red indicate alternans ratio and phase information. Panel B: Alternans area, region number and alternans ratio comparison between optically and electrically paced co-culture monolayer (2.64*2.64 mm^2), in which the ratio of cardiac myocytes and HEK-ChR2 is 100:1. Panel C: Alternans area, region number and alternans ratio comparison between optically paced myocte monolayer with locally cultured 8000 HEK-ChR2 cells and electrically myocyte only.

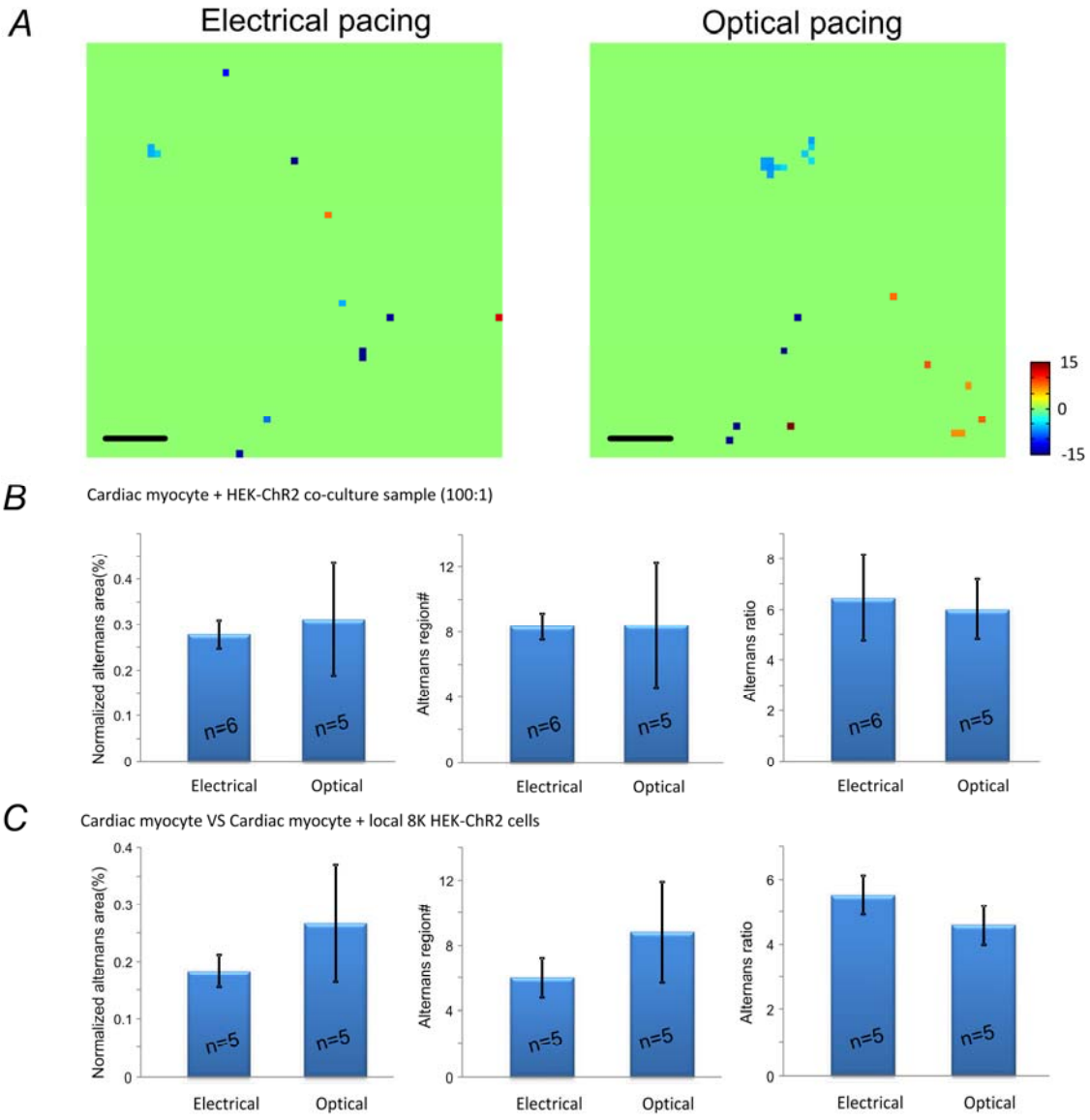
A
Electrical pacing
Optical pacing
15
0
-15
B
Cardiac myocyte + HEK-ChR2 co-culture sample (100:1)
Normalized alternans area(%)
Alternans region#
Alternans ratio
n=6
n=5
Electrical
Optical
C
Cardiac myocyte VS Cardiac myocyte + local 8K HEK-ChR2 cells
Normalized alternans area(%)
Alternans region#
Alternans ratio
n=5
Electrical
Optical

Chapter 6

FUTURE WORK

6.1 Abstract

This dissertation research has devised new tools for the study of Ca^{2+} alternans in cardiac tissue at unprecedented resolution. This work has demonstrated that these alternans at the cellular level are not all-or-nothing response, but evolve gradually over time and space, and are influenced by several important factors, e.g. cellular coupling and Ca^{2+}-Vm kinetics. Specifically, we developed an automatic detection algorithm with superior specificity and sensitivity to identify the amplitude and phase information of subtle cell-level Ca^{2+} alternans within a large FOV when used in conjunction with our ultra-high resolution optical mapping. Using computational and experimental approaches, we perturbed cellular coupling in two opposite directions to reveal its effect on alternans evolution. The complex non-monotonic relationship between alternans and intercellular coupling were verified by computer simulations and cardiac optogenetics. However, there are other relevant factors and conditions that need to be elucidated to better understand the emergence of Ca^{2+} instabilities in the heart as a prelude to cardiac arrhythmias. This brief chapter outlines one possible new direction for future work in this area, for which some preliminary data were obtained. Additional exciting directions include the further development of our optogenetics approach for fine-scale actuation (finer than electrical stimulation) – comparable to our ultra-high resolution optical mapping. Furthermore, work on reversible disruption of T-tubule structural integrity, that we published recently [152] but is not included in this dissertation, can benefit by means of probing for spatial profile of Ca^{2+} instabilities linked to these underlying structural changes.

6.2 Experimentally examine the role of local Ca^{2+}-V_m kinetics on the spatiotemporal evolution of intracellular Ca^{2+} alternans.

Cardiac tissue is inherently heterogeneous [153], and conventionally this heterogeneity was considered as the main source of alternans, especially for SDAs [154]. However, computer simulations [155, 156] indicate that SDAs can also be induced in homogeneous tissue by dynamic factors. Furthermore, VT induced by rapid pacing can spontaneously break up into VF in homogeneous initial conditions [157-159]. All these indicate that the evolution of cardiac alternans could be affected by dynamic factors like local Ca^{2+}-V_m relationship, which can be bidirectional, i.e. voltage or intracellular Ca^{2+} can act as a driving force. When the system is voltage-driven, Ca^{2+} alternans occur as a secondary phenomenon since the transmembrane potential (V_m) can easily affect the voltage-dependent L-type Ca^{2+} channels to induce further Ca^{2+} induced Ca^{2+} release and the electrical signal propagates much faster than the chemical signals (Ca^{2+}). V_m-driven alternans usually occur in positive V_m-Ca^{2+} coupling, while Ca^{2+}-driven alternans can be the result of either positive or negative Ca^{2+}-V_m coupling. We hypothesize that the local V_m-Ca^{2+} kinetics can change the spatiotemporal evolution profile of intracellular Ca^{2+} alternans in a quantifiable way. With the help of V_m-Ca^{2+} dual imaging optical system, we will attempt to reveal the nature of the V_m-Ca^{2+} coupling [160, 161] and how it relates to the spatiotemporal evolution of intracellular Ca^{2+} alternans.

A key technical problem in simultaneous dual imaging is the selection of proper fluorescence dyes. Based on our preliminary experimental results and experience, we choose RH-237 (voltage-sensitive dye) and Rhod-2 (Ca^{2+} sensitive dye) in our dual imaging system. Fig. 31 panel A illustrates the hardware system, panel B - the spectrum of the two dyes and panel C shows no crosstalk. Our imaging solution is unique in

combining high spatial resolution for Ca^{2+} imaging (>1 million pixels camera) and high temporal solution for V_m imaging (photodiode array, PDA at 1.6kHz) with special mode of illumination, resembling dark-field regime. The dyes share the same excitation light 525±20 nm, while the emitted fluorescence within 585±20 nm is collected by the intensified camera as Ca^{2+} signal and the fluorescence beyond 700 nm is collected as voltage signal recoded by the PDA. In previous dual imaging experiments from other labs, the spectral dye overlap was shown to be minimal [162, 163] . Our own preliminary tests with RH-237 and Rhod-2 (Fig. 31C) in our current setup also confirmed no crosstalk between the two fluorescence dyes.

6.2.1 Experimental setup for Ca^{2+}-V_m dual imaging

In order to examine the effects of local Ca^{2+}-V_m kinetics, the intracellular Ca^{2+} and transmembrane potential need to be recorded simultaneously. We demonstrate preliminary data from a dual imaging system for Ca^{2+} and transmembrane voltage (V_m),Fig.27. For records of intracellular Ca^{2+}, which require very fine spatial resolution but can tolerate moderate temporal resolution, we use an intensified camera system (pco CMOS 1280×1024), at 200 fps and at 20 μm/pix within a FOV>2×2 cm. The voltage signal, which diffuses faster, i.e. cannot form very small-scale patterns, but has higher-frequency features than the Ca^{2+} transients, will use a photodiode array (PDA) (WuTech Instruments, Gaithersburg, MD) with 464 channels and 0.75 mm diameter in a hex arrangement, and sampling frequency of 1.6 kHz. The two imaging detectors cover the same FOV simultaneously. We use RH-237 (voltage-sensitive dye) and Rhod-2/4 (Ca^{2+} sensitive dye). Light from a 250W QTH lamp is collimated, passed through 525±20 nm interference filter as excitation light, and focused on the monolayer at 90 degree angle via

a split light guide, creating dark field-like conditions. Fluorescence from the top stained sample is collected by a lens, and then passes through 585±20 nm interference as the Ca^{2+} signal. The rest of the fluorescence is collected by the PDA as voltage signal by passing a 700 nm long pass filter (KODAK WRATTEN Gelatin Filter).

As the optical mapping images from both camera and PDA are from the same monolayer (here we assume the thickness of monolayer is comparable with one myocyte), we need to register the two data sets temporally and spatially in order to examine the local Ca^{2+}-V_m kinetics. For the temporal registration, we are using an I/O board (USB4301, Measurement Computing Corporation, MA) to send out pulses to synchronize the camera and the PDA. The pulse sent to the camera will enable the camera to start data acquisition, while the pulse sent to the PDA will be received by a dedicated channel to trigger recording. For spatial registration, there are three dim LED red lights and two white lights, as Fig.32 shows, in the corner of the PDA aperture, which can be seen by the camera as spatial registration points.

Samples are co-labeled by two dyes: RH-237 and Rhod-2. The samples are first stained 20 minutes by Rhod-2 (8 μM) and then 10 minutes RH-237 (75μM), the last step is 10 minutes washing out with fresh Tyrode's.

6.2.2 Expected results and interpretation

We will construct maps of Ca^{2+} and V_m alternans over space using the developed algorithm in Aim 1. The Ca^{2+} and voltage are bi-directionally coupled in the cardiac tissue[164], which can be distinguished by the Ca^{2+} and V_m profile across nodal lines [160], as Fig. 33 shows. When voltage-driven alternans are present, the Ca^{2+} alternans should be alternating secondarily. The V_m-driven alternans typically occur in positive

coupling, but Ca^{2+}-driven alternans can be seen in positive or negative coupling. Positive Ca^{2+}-V_m coupling describes the situation when larger Ca^{2+} alternans can produce a longer APD. This is a consequence of a large Ca^{2+} transient increasing the net inward current during the action potential plateau by enhancing inward Na^{+}–Ca^{2+} exchange current to a greater extent than it reduces the L-type Ca^{2+} current. In Ca^{2+}-driven positive coupling, the spacing between nodes is on the tissue scale, around 1 cm [161]. On the other hand, negative Ca^{2+}-V_m coupling refers to the mode in which a larger Ca^{2+} transient causes a shorter APD. This occurs when the reduction in L-type Ca current dominates over the increased Na^{+}–Ca^{2+} exchange current. In Ca^{2+}-driven positive coupling, the spacing between nodes is a few cell lengths (100 to 400 μm)[161]. Therefore, if a dynamic instability causes the Ca^{2+} transient to alternate, then the APD will passively follow and also begin to alternate and vice versa.

In sum, SDA regions are critical to infer the types of local Ca^{2+}-V_m kinetics. As Fig.33 shows, the alternans can first be classified as Ca^{2+} driven or V_m driven by checking the Ca^{2+} and V_m profile across the nodal line. Then depending on the phase of Ca^{2+} and V_m transients, and the distance between nodes, we can determine positive or negative coupling. In the spatiotemporal domain, we can check the relationship between local Ca^{2+}-V_m kinetics and evolution of intracellular Ca^{2+} alternans.

Fig.31 Optical apparatus, spectrums of Rhod-2 and RH237[165] and verification of non-crosstalk. Panel A: the imaging setup for Ca^{2+}-V_m dual imaging: top intensified camera is for Ca^{2+} imaging, and bottom photo diode array (PDA) is for capturing V_m signal. Panel B: the emission spectrum for RH237 and Rhod2. Panel C: Verifying the cross talk between RH237 and Rhod2.

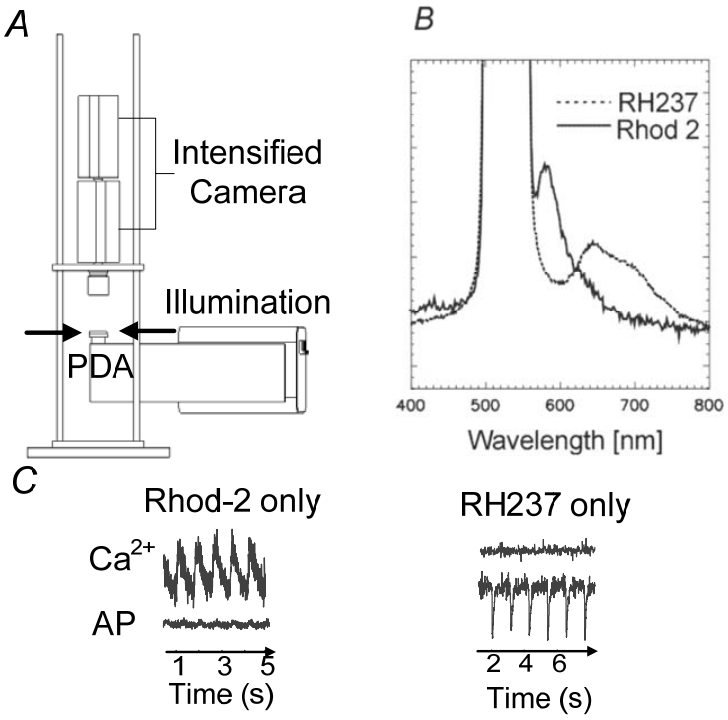

Fig.32 Imaging setup for dual V_m/Ca^{2+} mapping. Myocytes will be co-labeled by RH-237 (voltage-sensitive dye) and Rhod-2/4 (Ca^{2+} sensitive dye). Light from a 250W QTH lamp is collimated, passed through 525±20 nm interference filter as excitation light, and focused on the monolayer at 90 degree angle via a split light guide, creating dark field-like conditions. Fluorescence from the top stained sample is collected by a lens, and then passes through 585±20 nm interference as the Ca^{2+} signal. The rest of the fluorescence is collected by the PDA as voltage signal by passing a 700 nm long pass filter (KODAK WRATTEN Gelatin Filter).

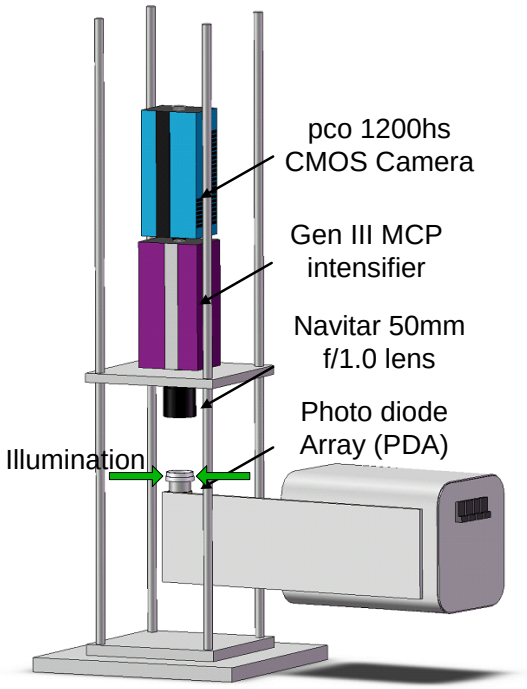

Fig.33 Types of local Ca^{2+} and V_m kinetics (Figures are modified from[160] [161]). The nodal line profile of Ca^{2+} and V_m can determine Ca^{2+} driven or V_m driven alternans. Then depending on the phase of Ca^{2+} and V_m transients, and the distance between nodes, one can determine positive or negative coupling of alternans.

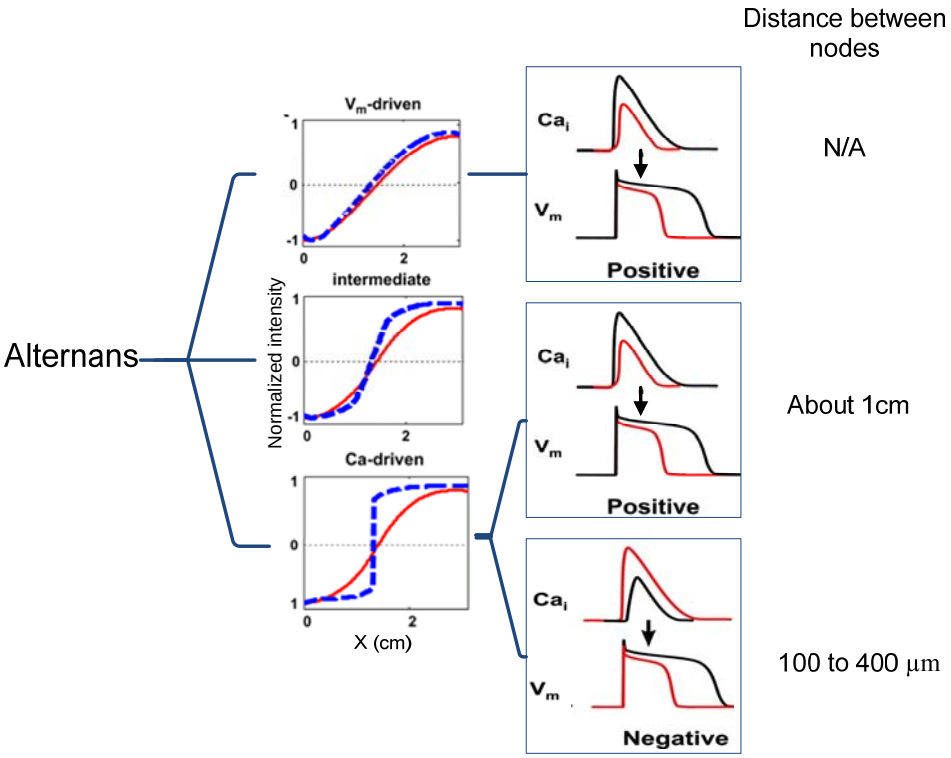

References

1. WRITING GROUP MEMBERS, et al., *Heart Disease and Stroke Statistics--2009 Update: A Report From the American Heart Association Statistics Committee and Stroke Statistics Subcommittee.* Circulation, 2009. **119**(3): p. e21-181.
2. Weiss, J.N., et al., *From Pulsus to Pulseless: The Saga of Cardiac Alternans.* Circ Res, 2006. **98**(10): p. 1244-1253.
3. Qu, Z., et al., *Mechanisms of Discordant Alternans and Induction of Reentry in Simulated Cardiac Tissue.* Circulation, 2000. **102**(14): p. 1664-1670.
4. Pastore, J.M. and D.S. Rosenbaum, *Role of Structural Barriers in the Mechanism of Alternans-Induced Reentry.* Circ Res, 2000. **87**(12): p. 1157-1163.
5. Chung, C.Y., H. Bien, and E. Entcheva, *The role of cardiac tissue alignment in modulating electrical function.* J Cardiovasc Electrophysiol, 2007. **18**(12): p. 1323-9.
6. Nolasco, J.B. and R.W. Dahlen, *A graphic method for the study of alternation in cardiac action potentials.* J Appl Physiol, 1968. **25**(2): p. 191-196.
7. Chudin, E., et al., *Intracellular Ca(2+) dynamics and the stability of ventricular tachycardia.* Biophys J, 1999. **77**(6): p. 2930-41.
8. Wier, W.G., et al., *Local control of excitation-contraction coupling in rat heart cells.* J Physiol, 1994. **474**(3): p. 463-71.
9. Sah, R., et al., *Regulation of cardiac excitation-contraction coupling by action potential repolarization: role of the transient outward potassium current (Ito).* J Physiol, 2003. **546**(1): p. 5-18.
10. Sato, D., et al., *Spatially Discordant Alternans in Cardiac Tissue: Role of Calcium Cycling.* Circ Res, 2006. **99**(5): p. 520-527.
11. Shiferaw, Y. and A. Karma, *Turing instability mediated by voltage and calcium diffusion in paced cardiac cells.* Proceedings of the National Academy of Sciences, 2006. **103**(15): p. 5670-5675.
12. Aistrup, G.L., et al., *Pacing-induced Heterogeneities in Intracellular Ca2+ Signaling, Cardiac Alternans, and Ventricular Arrhythmias in Intact Rat Heart.* Circ Res, 2006. **99**(7): p. E65-73.
13. Bien, H. and E. Entcheva, *Co-existence of reentrant waves with spatially discordant alternans*, in *Annual Heart Rhythm Society Meeting*2006: Boston, MA.
14. Kim, T.Y., et al., *Cardiac beat-to-beat alternations driven by unusual spiral waves.* Proceedings of the National Academy of Sciences, 2007. **104**(28): p. 11639-11642.
15. Iyer, V. and A.A. Armoundas. *Unraveling the Mechanisms of Catecholaminergic Polymorphic Ventricular Tachycardia*. in *Engineering in Medicine and Biology Society, 2006. EMBS '06. 28th Annual International Conference of the IEEE*. 2006.
16. Laitinen, P.J., et al., *Mutations of the Cardiac Ryanodine Receptor (RyR2) Gene in Familial Polymorphic Ventricular Tachycardia.* Circulation, 2001. **103**(4): p. 485-490.
17. Priori, S.G., et al., *Clinical and Molecular Characterization of Patients With Catecholaminergic Polymorphic Ventricular Tachycardia.* Circulation, 2002. **106**(1): p. 69-74.
18. Napolitano, C., S.G. Priori, and R. Bloise, *Catecholaminergic Polymorphic Ventricular Tachycardia.* 1993.

19. Bloomfield, D.M., et al., *Microvolt T-Wave Alternans and the Risk of Death or Sustained Ventricular Arrhythmias in Patients With Left Ventricular Dysfunction.* Journal of the American College of Cardiology, 2006. **47**(2): p. 456-463.
20. Martinez, J.P. and S. Olmos, *Methodological principles of T wave alternans analysis: a unified framework.* IEEE Trans Biomed Eng, 2005. **52**(4): p. 599-613.
21. Verrier, R.L., et al., *Ambulatory electrocardiogram-based tracking of T wave alternans in postmyocardial infarction patients to assess risk of cardiac arrest or arrhythmic death.* J Cardiovasc Electrophysiol, 2003. **14**(7): p. 705-11.
22. Adam, D.R., S. Akselrod, and R.J. Cohen, *Estimation of Ventricular Vulnerability to Fibrillation Through T-Wave Time Series Analysis.* Computers in Cardiology, 1981. **8**: p. pp. 307-310.
23. Adam, D.R., et al., *Ventricular Fibrillation and Fluctuations in the Magnitude of the Repolarization Vector.* Computers in Cardiology, 1982. **9**: p. 241-244.
24. Adam, D.R., et al., *Fluctuations in T-wave morphology and susceptibility to ventricular fibrillation.* J Electrocardiol, 1984. **17**(3): p. 209-18.
25. Entcheva, E. and H. Bien, *Macroscopic optical mapping of excitation in cardiac cell networks with ultra-high spatiotemporal resolution.* Progress in Biophysics and Molecular Biology, 2006. **92**(2): p. 232-257.
26. Kim, T.Y., et al., *Cardiac beat-to-beat alternations driven by unusual spiral waves.* Proc Natl Acad Sci U S A, 2007. **104**(28): p. 11639-42.
27. Weiss, J.N., et al., *From Pulsus to Pulseless: The Saga of Cardiac Alternans.* Circulation, 2006. **98**(10): p. 1244-1253.
28. Pham, Q., K.J. Quan, and D.S. Rosenbaum, *T-wave alternans: marker, mechanism, and methodology for predicting sudden cardiac death.* Journal of Electrocardiology, 2003. **36**(Supplement 1): p. 75-81.
29. Pastore, J.M., et al., *Mechanism Linking T-Wave Alternans to the Genesis of Cardiac Fibrillation.* Circulation, 1999. **99**(10): p. 1385-1394.
30. Jia, Z., et al. *Anti-arrhythmic Effects of 4-phenylbutyrate (4PB) in Cardiac Myocytes*. in *American Heart Association: Scientific Sessions 2009*. 2009. Orlando, Florida, USA.
31. Rodriguez-Sinovas, A., et al., *Enhanced effect of gap junction uncouplers on macroscopic electrical properties of reperfused myocardium.* J Physiol, 2004. **559**(1): p. 245-257.
32. Watanabe, M.A., et al., *Mechanisms for discordant alternans.* J Cardiovasc Electrophysiol, 2001. **12**(2): p. 196-206.
33. Karma, A., *Electrical alternans and spiral wave breakup in cardiac tissue.* Chaos, 1994. **4**(3): p. 461-472.
34. Qu, Z., J.N. Weiss, and A. Garfinkel, *Cardiac electrical restitution properties and stability of reentrant spiral waves: a simulation study.* Am J Physiol, 1999. **276**(1 Pt 2): p. H269-83.
35. Qu, Z., et al., *Scroll wave dynamics in a three-dimensional cardiac tissue model: roles of restitution, thickness, and fiber rotation.* Biophys J, 2000. **78**(6): p. 2761-75.
36. Sato, D., et al., *Inferring the Cellular Origin of Voltage and Calcium Alternans from the Spatial Scales of Phase Reversal during Discordant Alternans.* Biophys. J., 2007. **92**(4): p. L33-35.
37. Sepulveda, N.G., B.J. Roth, and J.P. Wikswo Jr, *Current injection into a two-dimensional anisotropic bidomain.* Biophysical Journal, 1989. **55**(5): p. 987-999.

38. Trayanova, N., K. Skouibine, and P. Moore, *Virtual electrode effects in defibrillation.* Prog Biophys Mol Biol., 1998. **69**(2-3): p. 387-403.
39. Jia, Z., H. Bien, and E. Entcheva, *Detecting Space-Time Alternating Biological Signals Close to the Bifurcation Point.* Biomedical Engineering, IEEE Transactions on, 2010. **57**(2): p. 316-324.
40. Weiss, J.N., et al., *The Dynamics of Cardiac Fibrillation.* Circulation, 2005. **112**(8): p. 1232-1240.
41. Kontula, K., et al., *Catecholaminergic polymorphic ventricular tachycardia: Recent mechanistic insights.* Cardiovascular Research, 2005. **67**(3): p. 379-387.
42. Zhiheng, J., H. Bien, and E. Entcheva, *Detecting Space-Time Alternating Biological Signals Close to the Bifurcation Point.* Biomedical Engineering, IEEE Transactions on, 2010. **57**(2): p. 316-324.
43. Strogatz, S.H., *Nonlinear Dynamics And Chaos: With Applications To Physics, Biology, Chemistry And Engineering*1998: Westview Press.
44. Pham, Q., K.J. Quan, and D.S. Rosenbaum, *T-wave alternans: marker, mechanism, and methodology for predicting sudden cardiac death.* Journal of Electrocardiology, 2003. **36**(Supplement 1): p. 75-81.
45. Karma, A. and R.F. Gilmour, *Nonlinear dynamics of heart rhythm disorders.* Physics Today, 2007. **60**(3): p. 51-57.
46. Weiss, J.N., et al., *The Dynamics of Cardiac Fibrillation.* Circulation, 2005. **112**(8): p. 1232-1240.
47. Adam, D.R., S. Akselrod, and R.J. Cohen, *Estimation of Ventricular Vulnerability to Fibrillation Through T-Wave Time Series Analysis.* Computers in Cardiology, 1981. **8**: p. 307-310.
48. Martinez, J.P. and S. Olmos, *Methodological principles of T wave alternans analysis: a unified framework.* IEEE Trans Biomed Eng, 2005. **52**(4): p. 599-613.
49. Verrier, R.L., et al., *Ambulatory Electrocardiogram-Based Tracking of T Wave Alternans in Postmyocardial Infarction Patients to Assess Risk of Cardiac Arrest or Arrhythmic Death.* Journal of Cardiovascular Electrophysiology, 2003. **14**(7): p. 705-711.
50. Kim, T.Y., et al., *Cardiac beat-to-beat alternations driven by unusual spiral waves.* Proc Natl Acad Sci U S A, 2007. **104**(28): p. 11639-42.
51. Weiss, J.N., et al., *From Pulsus to Pulseless: The Saga of Cardiac Alternans.* Circulation, 2006. **98**(10): p. 1244-1253.
52. Pastore, J.M., et al., *Mechanism Linking T-Wave Alternans to the Genesis of Cardiac Fibrillation.* Circulation, 1999. **99**(10): p. 1385-1394.
53. Jia, Z., H. Bien, and E. Entcheva, *A sensitive algorithm for automatic detection of space-time alternating signals in cardiac tissue.* Conf Proc IEEE Eng Med Biol Soc, 2008. **1**: p. 153-6.
54. de Diego, C., et al., *Spatially discordant alternans in cardiomyocyte monolayers.* Am J Physiol Heart Circ Physiol, 2008. **294**(3): p. H1417-1425.
55. Berger, C.M., et al., *Period-doubling bifurcation to alternans in paced cardiac tissue: crossover from smooth to border-collision characteristics.* Phys Rev Lett, 2007. **99**(5): p. 058101.
56. DANIEL M. BLOOMFIELD, S.H.H., RICHARD J. COHEN,, *Interpretation and Classification of Microvolt T Wave Alternans Tests.* Journal of Cardiovascular Electrophysiology, 2002. **13**(5): p. 502-512.

57. Nieminen, T., et al., *T-wave alternans predicts mortality in a population undergoing a clinically indicated exercise test.* Eur Heart J, 2007. **28**(19): p. 2332-2337.
58. Sredniawa, B., et al., *Current developments in microvolt T-wave alternans.* Indian Pacing Electrophysiol J, 2006. **6**(4): p. 214-25.
59. Albrecht, P., et al., *Exercise recordings for the detection of T wave alternans. Promises and pitfalls.* J Electrocardiol, 1996. **29 Suppl**: p. 46-51.
60. Hwang, S.M., T.Y. Kim, and K.J. Lee, *Complex-periodic spiral waves in confluent cardiac cell cultures induced by localized inhomogeneities.* Proc Natl Acad Sci U S A, 2005. **102**(29): p. 10363-8.
61. Qu, Z., et al., *Mechanisms of Discordant Alternans and Induction of Reentry in Simulated Cardiac Tissue.* Circulation, 2000. **102**(14): p. 1664-1670.
62. Sato, D., et al., *Spatially Discordant Alternans in Cardiac Tissue: Role of Calcium Cycling.* Circulation, 2006. **99**(5): p. 520-527.
63. Aistrup, G.L., et al., *Pacing-induced Heterogeneities in Intracellular Ca2+ Signaling, Cardiac Alternans, and Ventricular Arrhythmias in Intact Rat Heart.* Circulation, 2006. **99**(7): p. E65-73.
64. Watanabe, M.A., et al., *Mechanisms for discordant alternans.* J Cardiovasc Electrophysiol, 2001. **12**(2): p. 196-206.
65. Jia, Z., et al., *Cardiac Cellular Coupling and the Spread of Early Instabilities in Intracellular Ca2+.* Biophysical Journal, 2012. **102**(6): p. 1294-1302.
66. Chudin, E., et al., *Intracellular Ca2+ dynamics and the stability of ventricular tachycardia.* Biophys J, 1999. **77**: p. 2930-2941.
67. Kapur, S., et al., *Early development of intracellular calcium cycling defects in intact hearts of spontaneously hypertensive rats.* Am J Physiol Heart Circ Physiol, 2010. **299**(6): p. H1843-53.
68. Nemec, J., et al., *Calcium oscillations and T-wave lability precede ventricular arrhythmias in acquired long QT type 2.* Heart Rhythm, 2010. **7**(11): p. 1686-94.
69. Lehnart, S.E., et al., *Stabilization of cardiac ryanodine receptor prevents intracellular calcium leak and arrhythmias.* Proc Natl Acad Sci U S A, 2006. **103**(20): p. 7906-10.
70. Kang, G., et al., *Purkinje cells from RyR2 mutant mice are highly arrhythmogenic but responsive to targeted therapy.* Circ Res, 2010. **107**(4): p. 512-9.
71. Nolasco, J.B. and R.W. Dahlen, *A graphic method for the study of alternation in cardiac action potentials.* J Appl Physiol, 1968. **25** p. 191-196.
72. Eisner, D.A., et al., *Integrative analysis of calcium cycling in cardiac muscle.* Circ Res., 2000. **87**(12): p. 1087-1094.
73. Weiss, J.N., et al., *Alternans and arrhythmias: from cell to heart.* Circ Res, 2011. **108**(1): p. 98-112.
74. Echebarria, B. and A. Karma, *Amplitude equation approach to spatiotemporal dynamics of cardiac alternans.* Phys.Rev.E Stat.Nonlin.Soft.Matter Phys., 2007. **76**(5 Pt 1): p. 051911.
75. Kurebayashi, N., et al., *Behavior of Ca(2+) waves in multicellular preparations from guinea pig ventricle.* Am J Physiol Cell Physiol, 2004. **287**(6): p. C1646-C1656.
76. Shiferaw, Y. and A. Karma, *Turing instability mediated by voltage and calcium diffusion in paced cardiac cells.* Proc.Natl.Acad.Sci.U.S.A, 2006. **103**(15): p. 5670-5675.

77. Aistrup, G.L., et al., *Pacing-induced Heterogeneities in Intracellular Ca2+ Signaling, Cardiac Alternans, and Ventricular Arrhythmias in Intact Rat Heart.* Circ.Res., 2006.
78. Sato, D., et al., *Spatially discordant alternans in cardiac tissue: role of calcium cycling.* Circ.Res., 2006. **99**(5): p. 520-527.
79. Sato, D., et al., *Inferring the cellular origin of voltage and calcium alternans from the spatial scales of phase reversal during discordant alternans.* Biophys J, 2007. **92**(4): p. L33-5.
80. Kjolbye, A.L., et al., *Maintenance of intercellular coupling by the antiarrhythmic peptide rotigaptide suppresses arrhythmogenic discordant alternans.* Am J Physiol Heart Circ Physiol, 2008. **294**(1): p. H41-9.
81. Jia, Z.H., et al., *Anti-arrhythmic Effects of 4-phenylbutyrate (4PB) in Cardiac Myocytes.* Circulation, 2009. **120**(18): p. S653-S654.
82. Wade, M.H., J.E. Trosko, and M. Schindler, *A fluorescence photobleaching assay of gap junction-mediated communication between human cells.* Science, 1986. **232**(4749): p. 525-8.
83. Axelrod, D., et al., *Mobility measurement by analysis of fluorescence photobleaching recovery kinetics.* Biophys J, 1976. **16**(9): p. 1055-69.
84. Chung, C.Y., H. Bien, and E. Entcheva, *The role of cardiac tissue alignment in modulating electrical function.* J Cardiovasc Electrophysiol, 2007. **18**(12): p. 1323-9.
85. Yamasaki, H. and C.C. Naus, *Role of connexin genes in growth control.* Carcinogenesis, 1996. **17**(6): p. 1199-213.
86. Rodriguez-Sinovas, A., et al., *Enhanced effect of gap junction uncouplers on macroscopic electrical properties of reperfused myocardium.* J Physiol, 2004. **559**(1): p. 245-257.
87. Abbaci, M., et al., *Gap junctional intercellular communication capacity by gap-FRAP technique: A comparative study.* Biotechnology Journal, 2007. **2**(1): p. 50-61.
88. Jia, Z., H. Bien, and E. Entcheva. *A sensitive algorithm for automatic detection of space-time alternating signals in cardiac tissue*. in *Engineering in Medicine and Biology Society, 2008. EMBS 2008. 30th Annual International Conference of the IEEE*. 2008.
89. Rohr, S., D. Shoelly, and A. Kleber, *Patterned growth of neonatal rat heart cells in culture. Morphological and electrophysiological characteristics.* Circ Res, 1991. **68**: p. 114-130.
90. Entcheva, E., et al., *Contact fluorescence imaging of reentry in monolayers of cultured neonatal rat ventricular myocytes.* J Cardiovasc Electrophysiol, 2000. **11**(6): p. 665-76.
91. Entcheva, E. and H. Bien, *Tension development and nuclear eccentricity in topographically controlled cardiac syncytium.* Biomedical Microdevices, 2003. **5**(2): p. 163-168.
92. Bien, H., L. Yin, and E. Entcheva, *Calcium instabilities in Mammalian cardiomyocyte networks.* Biophys.J., 2006. **90**(7): p. 2628-2640.
93. Chung, C.Y., et al., *Hypertrophic phenotype in cardiac cell assemblies solely by structural cues and ensuing self-organization.* Faseb J, 2011. **25**(3): p. 851-62.
94. Bursac, N., F. Aguel, and L. Tung, *Multiarm spirals in a two-dimensional cardiac substrate.* Proc Natl.Acad.Sci.U.S.A, 2004. **101**(43): p. 15530-15534.
95. McSpadden, L.C., R.D. Kirkton, and N. Bursac, *Electrotonic loading of anisotropic cardiac monolayers by unexcitable cells depends on connexin type and expression level.* Am J Physiol Cell Physiol, 2009. **297**(2): p. C339-51.

96. Takens-Kwak, B.R., et al., *Mechanism of heptanol-induced uncoupling of cardiac gap junctions: a perforated patch-clamp study.* Am J Physiol Cell Physiol, 1992. **262**(6): p. C1531-1538.
97. Ammerpohl, O., et al., *Complementary effects of HDAC inhibitor 4-PB on gap junction communication and cellular export mechanisms support restoration of chemosensitivity of PDAC cells.* Br J Cancer, 2006. **96**(1): p. 73-81.
98. Asklund, T., et al., *Histone deacetylase inhibitor 4-phenylbutyrate modulates glial fibrillary acidic protein and connexin 43 expression, and enhances gap-junction communication, in human glioblastoma cells.* Eur J Cancer, 2004. **40**(7): p. 1073-81.
99. Jia, Z., H. Bien, and E. Entcheva, *Detecting space-time alternating biological signals close to the bifurcation point.* IEEE Trans Biomed Eng, 2010. **57**(2): p. 316-24.
100. Entcheva, E. and H. Bien, *Macroscopic optical mapping of excitation in cardiac cell networks with ultra-high spatiotemporal resolution.* Prog.Biophys.Mol.Biol., 2006. **92**(2): p. 232-257.
101. Kanungo, T., et al., *An Efficient k-Means Clustering Algorithm: Analysis and Implementation.* IEEE Trans. Pattern Anal. Mach. Intell., 2002. **24**(7): p. 881-892.
102. Jia, Z., et al., *Cardiac Cellular Coupling and the Spread of Early Instabilities in Intracellular Ca2+.* Biophysical Journal, 2012. **102**(6): p. 1294-1302.
103. Winslow, R.L., et al., *Mechanisms of Altered Excitation-Contraction Coupling in Canine Tachycardia-Induced Heart Failure, II : Model Studies.* Circ Res, 1999. **84**(5): p. 571-586.
104. Luo, C. and Y. Rudy, *A dynamic model of the cardiac ventricular action potential. I. Simulations of ionic currents and concentration changes.* Circ Res, 1994. **74**(6): p. 1071-1096.
105. Colecraft, H.M., et al., *Novel functional properties of Ca2+ channel β subunits revealed by their expression in adult rat heart cells.* The Journal of Physiology, 2002. **541**(2): p. 435-452.
106. Shiferaw, Y., et al., *Model of Intracellular Calcium Cycling in Ventricular Myocytes.* Biophysical Journal, 2003. **85**(6): p. 3666-3686.
107. Crank, J., *The Mathematics of Diffusion*1975, Oxford: Oxford University Press. 414.
108. Qu, Z. and A. Garfinkel, *An advanced algorithm for solving partial differential equation in cardiac conduction.* IEEE Trans Biomed Eng, 1999. **46**(9): p. 1166-8.
109. Shiferaw, Y., et al., *Model of intracellular calcium cycling in ventricular myocytes.* Biophys.J, 2003. **85**(6): p. 3666-3686.
110. Fox, J.J., J.L. McHarg, and R.F. Gilmour, Jr., *Ionic mechanism of electrical alternans.* Am J Physiol Heart Circ Physiol, 2002. **282**(2): p. H516-H530.
111. Shiferaw, Y., D. Sato, and A. Karma, *Coupled dynamics of voltage and calcium in paced cardiac cells.* Physical Review E, 2005. **71**: p. 10-15.
112. Sato, D., et al., *Inferring the cellular origin of voltage and calcium alternans from the spatial scales of phase reversal during discordant alternans.* Biophys J, 2007. **92**(4): p. L33-5.
113. Winfree, A.T., *A spatial scale factor for electrophysiological models of myocardium.* Prog.Biophys Mol.Biol, 1998. **69**(2-3): p. 185-203.
114. Allbritton, N.L., T. Meyer, and L. Stryer, *Range of messenger action of calcium ion and inositol 1,4,5-trisphosphate.* Science, 1992. **258**(5089): p. 1812-5.

115. Fabiato, A., *Two kinds of calcium-induced release of calcium from the sarcoplasmic reticulum of skinned cardiac cells.* Adv Exp Med Biol, 1992. **311**: p. 245-62.
116. Tang, Y. and H.G. Othmer, *A model of calcium dynamics in cardiac myocytes based on the kinetics of ryanodine-sensitive calcium channels.* Biophys J, 1994. **67**(6): p. 2223-35.
117. Shiferaw, Y. and A. Karma, *Turing instability mediated by voltage and calcium diffusion in paced cardiac cells.* Proceedings of the National Academy of Sciences, 2006. **103**(15): p. 5670-5675.
118. Echebarria, B. and A. Karma, *Instability and Spatiotemporal Dynamics of Alternans in Paced Cardiac Tissue.* Physical Review Letters, 2002. **88**(20): p. 208101.
119. Ohara, T., et al., *Increased vulnerability to inducible atrial fibrillation caused by partial cellular uncoupling with heptanol.* American Journal of Physiology - Heart and Circulatory Physiology, 2002. **283**(3): p. H1116-H1122.
120. Qu, Z., et al., *Effects of Na+ channel and cell coupling abnormalities on vulnerability to reentry: a simulation study.* American Journal of Physiology - Heart and Circulatory Physiology, 2004. **286**(4): p. H1310-H1321.
121. Jia, Z., et al., *Stimulating Cardiac Muscle by Light / Clinical Perspective.* Circulation: Arrhythmia and Electrophysiology, 2011. **4**(5): p. 753-760.
122. Sepulveda, N.G., B.J. Roth, and J.P. Wikswo Jr, *Current injection into a two-dimensional anisotropic bidomain.* Biophysical Journal, 1989. **55**(5): p. 987-999.
123. Trayanova, N., K. Skouibine, and P. Moore, *Virtual electrode effects in defibrillation.* Prog Biophys Mol Biol., 1998. **69**(2-3): p. 387-403.
124. Oesterhelt, D. and W. Stoeckenius, *Rhodopsin-like protein from the purple membrane of Halobacterium halobium.* Nat New Biol, 1971. **233**(39): p. 149-52.
125. Vsevolodov, N.N., *Biomolecular Electronics. An Introduction via Photosensitive Proteins*1998, Boston: Birkhauser.
126. Nagel, G., et al., *Channelrhodopsin-2, a directly light-gated cation-selective membrane channel.* Proc Natl Acad Sci U S A, 2003. **100**(24): p. 13940-5.
127. Boyden, E.S., et al., *Millisecond-timescale, genetically targeted optical control of neural activity.* Nat Neurosci, 2005. **8**(9): p. 1263-8.
128. Li, X., et al., *Fast noninvasive activation and inhibition of neural and network activity by vertebrate rhodopsin and green algae channelrhodopsin.* Proc Natl Acad Sci U S A, 2005. **102**(49): p. 17816-21.
129. Wang, H., et al., *High-speed mapping of synaptic connectivity using photostimulation in Channelrhodopsin-2 transgenic mice.* Proc Natl Acad Sci U S A, 2007. **104**(19): p. 8143-8.
130. Han, X. and E.S. Boyden, *Multiple-color optical activation, silencing, and desynchronization of neural activity, with single-spike temporal resolution.* PLoS One, 2007. **2**(3): p. e299.
131. Chow, B.Y., et al., *High-performance genetically targetable optical neural silencing by light-driven proton pumps.* Nature, 2010. **463**(7277): p. 98-102.
132. Gunaydin, L.A., et al., *Ultrafast optogenetic control.* Nat Neurosci, 2010. **13**(3): p. 387-92.
133. Airan, R.D., et al., *Temporally precise in vivo control of intracellular signalling.* Nature, 2009. **458**(7241): p. 1025-9.
134. Huber, D., et al., *Sparse optical microstimulation in barrel cortex drives learned behaviour in freely moving mice.* Nature, 2008. **451**(7174): p. 61-4.

135. Nagel, G., et al., *Light activation of channelrhodopsin-2 in excitable cells of Caenorhabditis elegans triggers rapid behavioral responses.* Curr Biol, 2005. **15**(24): p. 2279-84.
136. Bruegmann, T., et al., *Optogenetic control of heart muscle in vitro and in vivo.* Nat Methods, 2010. **7**(11): p. 897-900.
137. Arrenberg, A.B., et al., *Optogenetic control of cardiac function.* Science, 2010. **330**(6006): p. 971-4.
138. Jia, Z., et al., *Optically activated light-sensitive channels can pace cardac tissue and generate propagating cardiac impulses.* Circulation Research, 2010. **107**(12): p. LateBreaking Basic Science Abstracts, AHA.
139. Valiunas, V., et al., *Coupling an HCN2-expressing cell to a myocyte creates a two-cell pacing unit.* J Physiol, 2009. **587**(Pt 21): p. 5211-26.
140. Entcheva, E. and H. Bien, *Tension development and nuclear eccentricity in topographically controlled cardiac syncytium.* J Biomed Microdev, 2003. **5**(2): p. 163-168.
141. Yin, L., H. Bien, and E. Entcheva, *Scaffold topography alters intracellular calcium dynamics in cultured cardiomyocyte networks.* Am J Physiol Heart Circ Physiol, 2004. **287**(3): p. H1276-H1285.
142. Chung, C.Y., H. Bien, and E. Entcheva, *The role of cardiac tissue alignment in modulating electrical function.* J Cardiovasc Electrophysiol, 2007. **18**(12): p. 1323-9.
143. Entcheva, E. and H. Bien, *Macroscopic optical mapping of excitation in cardiac cell networks with ultra-high spatiotemporal resolution.* Prog.Biophys.Mol.Biol., 2006. **92**(2): p. 232-257.
144. Bien, H., L. Yin, and E. Entcheva, *Calcium instabilities in Mammalian cardiomyocyte networks.* Biophys.J., 2006. **90**(7): p. 2628-2640.
145. Yu, H., et al., *Effects of the renin-angiotensin system on the current I(to) in epicardial and endocardial ventricular myocytes from the canine heart.* Circ Res, 2000. **86**(10): p. 1062-8.
146. Valiunas, V., et al., *Coupling an HCN2 expressing cell to a myocyte creates a two cell pacing unit.* J Physiol, 2009.
147. Valiunas, V., et al., *Gap junction channels formed by coexpressed connexin40 and connexin43.* Am J Physiol Heart Circ Physiol, 2001. **281**(4): p. H1675-89.
148. Valiunas, V., E.C. Beyer, and P.R. Brink, *Cardiac gap junction channels show quantitative differences in selectivity.* Circ.Res., 2002. **91**(2): p. 104-111.
149. Chater, T.E., et al., *Voltage- and temperature-dependent gating of heterologously expressed channelrhodopsin-2.* J Neurosci Methods, 2010.
150. Cardin, J.A., et al., *Targeted optogenetic stimulation and recording of neurons in vivo using cell-type-specific expression of Channelrhodopsin-2.* Nat Protoc, 2010. **5**(2): p. 247-54.
151. Malmivuo, J. and R. Plonsey, *Bioelectromagnetism*1995, New York: Oxford University Press.
152. Wu, C.-Y.C., et al., *PI3Ks Maintain the Structural Integrity of T-Tubules in Cardiac Myocytes.* PLoS ONE, 2011. **6**(9): p. e24404.
153. Pastore, J.M., et al., *Mechanism Linking T-Wave Alternans to the Genesis of Cardiac Fibrillation.* Circulation, 1999. **99**(10): p. 1385-1394.

154. Pastore, J.M. and D.S. Rosenbaum, *Role of Structural Barriers in the Mechanism of Alternans-Induced Reentry.* Circ Res, 2000. **87**(12): p. 1157-1163.
155. Watanabe, M.A., et al., *Mechanisms for discordant alternans.* J Cardiovasc Electrophysiol, 2001. **12**(2): p. 196-206.
156. Qu, Z., et al., *Mechanisms of Discordant Alternans and Induction of Reentry in Simulated Cardiac Tissue.* Circulation, 2000. **102**(14): p. 1664-1670.
157. Karma, A., *Electrical alternans and spiral wave breakup in cardiac tissue.* Chaos, 1994. **4**(3): p. 461-472.
158. Qu, Z., J.N. Weiss, and A. Garfinkel, *Cardiac electrical restitution properties and stability of reentrant spiral waves: a simulation study.* Am J Physiol, 1999. **276**(1 Pt 2): p. H269-83.
159. Qu, Z., et al., *Scroll wave dynamics in a three-dimensional cardiac tissue model: roles of restitution, thickness, and fiber rotation.* Biophys J, 2000. **78**(6): p. 2761-75.
160. Sato, D., et al., *Inferring the Cellular Origin of Voltage and Calcium Alternans from the Spatial Scales of Phase Reversal during Discordant Alternans.* Biophys. J., 2007. **92**(4): p. L33-35.
161. Sato, D., et al., *Spatially Discordant Alternans in Cardiac Tissue: Role of Calcium Cycling.* Circ Res, 2006. **99**(5): p. 520-527.
162. Kong, W., et al., *Emission ratiometry for simultaneous calcium and action potential measurements with coloaded dyes in rabbit hearts: reduction of motion and drift.* J Cardiovasc Electrophysiol, 2003. **14**(1): p. 76-82.
163. Johnson, P.L., et al., *Errors caused by combination of Di-4 ANEPPS and Fluo3/4 for simultaneous measurements of transmembrane potentials and intracellular calcium.* Ann Biomed Eng, 1999. **27**(4): p. 563-71.
164. Weiss, J.N., et al., *From Pulsus to Pulseless: The Saga of Cardiac Alternans.* Circ Res, 2006. **98**(10): p. 1244-1253.
165. Choi, B.R. and G. Salama, *Simultaneous maps of optical action potentials and calcium transients in guinea-pig hearts: mechanisms underlying concordant alternans.* J Physiol, 2000. **529 Pt 1**: p. 171-88.